Three-Dimensional Histopathology of the Human Liver

Chelsea L Fortin

A dissertation

submitted in partial fulfillment of the

requirements for the degree of

Doctor of Philosophy

University of Washington

2021

Reading Committee:

Kelly R. Stevens, Chair

Thomas N. Wight

Ying Zheng

Program Authorized to Offer Degree:

Molecular Medicine and Mechanisms of Disease

University of Washington

Abstract

Three-Dimensional Histopathology of the Human Liver

Chelsea L. Fortin

Chair of the Supervisory Committee:
Dr. Kelly R. Stevens, Assistant Professor
Departments of Bioengineering and Lab Medicine & Pathology

The liver performs hundreds of functions and is considered second only to the brain in structural and functional complexity. One critical spatial aspect of liver architecture is the division of the primary functional unit (the lobule) into "zones" where cells perform different functions (functional zonation). Lobular zones also contain different types of vascular and biliary structures (structural zonation). The homeostasis of this intricate architecture is critical for liver function and health, and its disruption is pathologic. Visual examination of tissue under the microscope (histopathology) is the gold standard for diagnosing many liver diseases, including the severe scar-tissue buildup known as cirrhosis, examined here.

The liver's architecture at cell-level resolution has been elucidated largely via two-dimensional (2D) traditional histology, the interrogation of thin slices of tissue under a microscope. 2D histology has provided centuries' worth of information but is not without limitations. For one,

sectioning tissue into thin slices can physically alter the examined structures. Beyond that, the 2D nature of histology can misrepresent actual biological structures: 1) three-dimensionally (3D) convoluted structures often appear as multiple distinct objects in a 2D cross-section, 2) cross-sections may not accurately capture the distribution of objects within a tissue volume, and 3) 2D slices may simply not contain rare or sparse objects. To overcome these limitations, groups have recently begun imaging thick liver samples via 3D immunostaining and tissue clearing, which render the tissue optically clear and permit deeper imaging than traditional methods. The rodent liver was the subject of most of this work; the few 3D human liver studies have imaged less than one lobule to a depth equivalent to approximately 20 traditional tissue sections.

Here, we have surpassed existing 3D human liver imaging studies by imaging a depth equivalent to approximately 100 traditional tissue sections, roughly 200 times the previously captured tissue volume. We have developed a 3D imaging and analysis pipeline to define structures across multiple human liver lobules empirically. First, we optimized immunostaining for diverse hepatic cell types and structures, customized tissue clearing to work robustly in the liver, and established a large-field, micrometer-resolution 3D confocal imaging workflow. Next, we developed a pipeline for image processing and 3D analysis & morphometry of branching and non-branching structures. Utilizing this, we uncover the dysregulation of the structurally zonated vascular and biliary networks of the human liver within cirrhosis. We find a significant expansion of periportal structures with significant regression of pericentral structures. These findings suggest a decentralization phenotype within cirrhosis of multiple etiologies, with possible functional consequences for blood drainage and nutrient and drug metabolism. Together, these efforts provide methods for staining, clearing, reconstructing, and analyzing structures within cell-dense tissues

like the liver; unveil never-before-seen-in-3D human liver structures across multiple size scales; and reveal volumetric dysregulations of structural and functional zonation in cirrhosis.

TABLE OF CONTENTS

List of Figures 9

List of Tables 10

Chapter 1. Introduction 15

1.1 Liver Disease and Human Health 15

1.1.1 Liver disease- and cirrhosis-related health disparities in the United States (US) 16

1.2 The Microanatomy of the Normal Liver 18

1.2.1 The Lobule 18

1.2.2 Structural and Functional Zonation 20

1.3 Liver Cirrhosis and Cirrhotic Microanatomy 23

1.3.1 Liver Cirrhosis 23

1.3.2 The Lobule and Zonation in Cirrhosis 25

1.4 The Current State of the Art of Human Liver 3D Imaging 29

1.4.1 Tissue clearing and the liver 35

1.5 Summary 38

Chapter 2. Multiplexed 3D Immunostaining, Clearing, and Imaging of the Human Liver 40

2.1 Introduction 40

2.2 Materials and Methods 41

2.2.1 Human liver samples 41

2.2.2 Whole-mount staining of human liver biopsies with antibodies & small molecules 42

2.2.3 Optical clearing of cell-dense tissue 43

2.2.4 3D confocal imaging and image processing 44

2.3 Results 45
2.3.1 An optimized pipeline for reconstructing human liver tissue. 45
2.3.2 Deep fluorescent labeling and 3D imaging of cell-resolution hepatic structures. 46
2.3.3 Deep, large-field fluorescent labeling and imaging of zonated mesoscale hepatic structures. 51
2.3.4 Multilobular 3D imaging permits visualization of the first human z-dimensional portal-central axis. 58
2.4 Discussion 62
Chapter 3. Morphometric Multilobular 3D Imaging of the Human Liver Reveals Periportal Expansion and Pericentral Regression within the Cirrhotic Liver 64
3.1 Introduction 64
3.2 Materials and Methods 66
3.2.1 Non-fibrotic and cirrhotic human liver samples 66
3.2.2 Deep immunolabeling of structural (Architecture Panel) and functional (Zonation Panel) zonation and tissue clearing 67
3.2.3 3D imaging and image processing 69
3.2.4 Quantitative morphometric analysis 70
3.2.5 Statistical analysis 71
3.3 Results 71
3.3.1 Traditional 2D histopathology to phenotype analyzed samples. 71
3.3.2 Development of 3D models of branching structures. 74
3.3.3 3D surface models of structures and networks. 77

3.3.4 The cirrhotic liver contains a denser and more complex 3D network of CD31+ microvessels than non-fibrotic. 79
3.3.5 The cirrhotic 3D biliary network fills more tissue volume than the non-fibrotic biliary network. 83
3.3.6 The cirrhotic liver contains fewer individual central venules compared to non-fibrotic. 86
3.3.7 Dysregulation of hepatocyte zonation of the cirrhotic liver. 88
3.4 Discussion 90
Chapter 4. Conclusions and Future Directions 94
Bibliography 101

LIST OF FIGURES

Figure 1.1. Normal liver architecture. 20
Figure 1.2. Normal liver functional zonation. 22
Figure 1.3. Liver regeneration and fibrosis. 25
Figure 1.4. Dysregulation of cirrhotic structural and functional zonation. 28
Figure 1.5. 2D histology misrepresents 3D structures. 30
Figure 1.6. Graphical literature review: Multiscale 3D human imaging. 34
Figure 2.1. Schematic of the 3D liver mapping pipeline. 46
Figure 2.2. Deep labeling and 3D imaging unveils volumetric microscale human liver structures and networks. 50
Figure 2.3. Deep labeling and 3D imaging of multilobular structures. 57
Figure 2.4. Combining thick staining with large-field imaging enables 3D visualization of human liver architecture across multiple lobules. 61
Figure 3.1. Traditional histological staining for phenotyping our analyzed samples. 73
Figure 3.2. Branching structures are reconstructed as 3D models using Vesselucida. 76
Figure 3.3. Volumetric structures are reconstructed as 3D models using Imaris. 78
Figure 3.4. 3D imaging unveils an increase in CD31+ microvessel network density and complexity in cirrhosis. 82
Figure 3.5. 3D imaging unveils an expansion of CK19+ ductule network volume in cirrhosis. 85
Figure 3.6. 3D imaging shows fewer central venules present in cirrhotic liver. 88
Figure 3.7. 3D imaging of human liver zonation reveals a decentralization phenotype in cirrhotic liver. 90

LIST OF TABLES

Table 2.1. Key Resources Table - Antibodies and Small Molecules..... 43
Table 3.1. Details for analyzed samples. 66
Table 3.2. Key Resources Table – Multiplexed Antibody Panels..... 68

ACKNOWLEDGEMENTS

Firstly, I thank my advisor, Doctor Kelly R. Stevens. We began working together before I graduated from undergrad (when I was only 21!). You took a chance on a young cell and molecular biologist. You hired me into my first bioengineering lab, introducing me to a world of applied biology that I had not previously experienced. We mutually desired me to undertake my Ph.D. studies in your lab. You allowed me to experience many things that most Ph.D.'s do not, including lab startup, building perfusion machines from parts, and mentorship and training of most incoming lab members. At this point in my life, we have worked together for seven years; I am now 28 years old, so this is a quarter of my life. It goes without saying that this is foundational! It was an honor to grow under your wing and watch you grow and change over your career.

I thank my doctoral supervisory committee, Doctors Thomas N. Wight, Jean S. Campbell, Raymond S. W. Yeung, Ying Zheng, Edward J. Kelly, and John D. Scott. You have been a source of support, challenge, mentorship, and advice. Dr. Wight, you gave me my first laboratory rotation, where I learned invaluable histology skills. Dr. Campbell, you introduced me to the Ce3D clearing technique used in this dissertation. Dr. Yeung, you provided clinical samples for the work presented here. Special thanks to Drs. Wight, Zheng, and Stevens for serving on my reading committee. Thank you all.

I thank all past and present members of the Stevens lab. I could never put the true extent of my gratitude into words. You have been friends, colleagues, advisors, emotional supports, and just plain fun. You have made coming into work each day something I look forward to. This last year of COVID-19-induced working from home has made that ever more evident. Special thanks to Doctors Daniel Corbett, Mary Regier, Fredrik Johansson, and Tara McCray, as well as Jonathan Mene, Emily Olszewski, Parker Grosjean, Eileen Brady, Colleen O'Connor, Sarah Saxton, Wesley

Fabyan, Susana Simmonds Bohorquez, and Olivia Prado. Thank you to Dr. McCray for both becoming a true friend and collaborating with me in the last year to continue a project away from which I had to shift focus. I am in immense gratitude to Susy and Wes, who joined me to stain, image, and analyze the normal and cirrhotic samples presented here in Chapter 3. Without you, it would have been much less fun and taken much more time. Thank you for helping me learn to lead a small team. Thank you all for being you!

I thank my doctoral program, with special thanks to Doctor William Mahoney and Megan Barker, who have guided me through the ins and outs of the last five years. To my program cohort, Michael Kiflezghi, Emily Kohlbrenner, Allison Knupp, Doctor Melissa Kordahi, Doctor Denise Chac, and Doctor Yevgeniy Yuzefpolskiy, thank you for walking side-by-side with me through this process. To Darrian Bugg, who has become a trusted, beloved friend and colleague, thank you for years of personal and professional support and advice. To Louisa Helms and to Doctors Eric Nealy, Katie Baker, Charlotte James, Mimi Krutein, Ian Dowsett, and Mitchell Lee, thank you for injecting fulfilling friendships into my time in the program. Thank you to Katherine Manbeck of UW Psychology for reviewing the portion of this dissertation regarding health disparities; your expertise was so valuable and insightful.

I owe never-ending thanks to my family for their support and love throughout my entire life. To my mother, Trina Fortin, who has always been there for me. You taught me that education elevates circumstance. You gave me every available opportunity and allowed me to become myself. To my twin sister, Doctor Patricia Fortin, who inspires me every day in her work as a clinician and keeps me laughing with unparalleled hilarity. To my soon-to-be in-laws, Doctors Lauren Montgomery & Michael Johnson, and Doctor Samuel Wasser & Elizabeth Welch, thank you for accepting me, loving me, and genuinely becoming my family.

A special thank you to my partner, Noah Wasser, who has supported, motivated, and lifted me every day of this process. It was not easy, but your support provided strength and grace in good times and in bad. I love you, and I cannot wait to marry you (one week after my defense!).

Thank you to the National Institutes of Health for supporting this doctoral work (T32 GM095421, TL1 TR002318). I also thank my undergraduate funding sources, without which I would not have had financial access to higher education or unpaid research experiences. I thank Boston University's Undergraduate Research Opportunities Program, BU Financial Assistance, the Finance Authority of Maine, and the US Department of Education.

Thank you to the anonymous donors who consented to donate tissue to scientific research. Your contributions made this dissertation possible.

Created with BioRender.com.

DEDICATION

For my father, who was unable to participate in my childhood or adulthood because of addiction and end-stage liver failure. You taught me early that patients are people first. May the work of my colleagues and myself ease the burdens you carried.

Chapter 1. INTRODUCTION

This chapter will introduce the motivation for 3D microscopy of large human liver samples and volumetric study of architectural changes in cirrhosis. First, we provide an overview of liver disease and its impacts on human health, focusing on the inequitable distribution of liver disease burden. Then, we examine the liver's complex architecture and how it changes in cirrhosis. Traditional 2D histology elucidated these structures, so finally, we will review what modern 3D histology has unveiled about the human liver's structure and what is left to be determined.

The liver has an intricately complex architecture, with unevenly distributed (zonated) features and tube-like networks. The volume of the human lobule is about an order of magnitude larger than that of model organisms like mice. Therefore, we hypothesize that a large-field 3D imaging and analysis approach enables mapping the non-fibrotic and cirrhotic human liver. This work is impactful in that it unveils volumetric changes in the cirrhotic liver that may have functional implications and provides micrometer-resolution 3D blueprints for the hepatic tissue engineering community.

1.1 Liver Disease and Human Health

Liver disease is the 11th most common global cause of death, representing two million deaths each year, half of which are cirrhotic. [1] Liver disease also causes significant morbidity; approximately ten times as many people live with complications as those who die yearly (based on US data). [2] The severity of this burden might be unexpected, considering the liver's regenerative capacity.

The liver is the only visceral organ that humans can regenerate. Insults such as substance abuse, obesity, genetic abnormalities, and infectious diseases may injure the organ. Upon removing the

insult, the organ will undergo a reparative regeneration process where remaining healthy tissue grows to reestablish lost liver function. However, with sustained liver injury, this transient regenerative response will become a pathologic steady state known as fibrosis, characterized by excessive deposition of a scar-like extracellular matrix and reduced organ function. [3] If this fibrotic response continues, the scar tissue will expand, forming fibrous bands throughout the organ that isolate portions of tissue from each other. This progressed fibrosis is the severe condition called cirrhosis that causes half of worldwide liver disease-related deaths each year. The gold standard for cirrhosis diagnosis is the microscopic examination of a biopsy, where the severe structural changes are evident.

1.1.1 *Liver disease- and cirrhosis-related health disparities in the United States (US)*

This section aims to discuss some of the US's health care disparities, specifically regarding liver diseases. This discussion is not an extensive review of the many inequities liver disease patients may face. However, it is crucial to include this review in this scholarly work, as researchers and our works affect societal systems and societal systems impact our work. Identifying and naming the inequities within these systems and our own work is a responsibility that each researcher must accept.

Health disparities can be broadly defined as "clinically and statistically significant differences in health outcomes… between socially distinct vulnerable and less vulnerable populations." [4] Population vulnerability depends on a wide range of social, economic, and environmental determinants of health, which, among many others, include sex, race, age, socioeconomic status, and (dis)ability. [5] It is essential to use an intersectional framework to recognize that multiple social factors overlap when shaping an individual's health. [6] Health disparities have been reported foci of many health care and governmental organizations for decades. While there has

been incremental progress, there are still significant disparities disproportionately affecting individuals of marginalized populations.

Many liver diseases that can lead to cirrhosis, from viral hepatitis to alcoholism to cancers, display health disparities. [7, 8, 9] Racial and ethnic disparities are a primary source of inequitable liver disease outcomes. The only curative treatment for end-stage liver disease is a transplant, but racial and ethnic minorities have disproportionately low access to transplant listing. [12, 13] Particularly relevant to the year 2021, when the world has been battling the COVID-19 pandemic for over a year, are the racial and socioeconomic disparities in telehealth utilization for liver disease care. [14] There is increasing evidence that systemic racism, not the individual's race or ethnicity, is the cause of the disproportionate morbidity and mortality burden placed on racial and ethnic minorities. [10, 11]

Socioeconomic status is another significant disparity observed within liver diseases, partially due to disproportionate risk factors like injectable drug use and obesity. [15, 16] The percentage of Americans with liver disease is two-fold higher for those with less than a high school diploma than a Bachelor's degree, three-fold higher for the unemployed than the employed, and three-fold higher for those who make less than $35,000 compared to $100,000 or more, annually. [2] Socioeconomic status also contributes to an individual's inability to be listed to receive a life-saving liver transplant. [13]

Meaningful progress in addressing these inequities will require a partnership between patients, health care providers, researchers who build and discover the next generation of therapies, insurance companies, policymakers, philanthropic organizations, and public health workers. [17] Addressing the systemic racism and classism contributing to the racial, ethnic, and socioeconomic disparities prevalent within liver disease will require all of society. Most proposed frameworks to

address health disparities include the first step of increasing awareness of the inequities that patient populations face. This dissertation would be incomplete without discussing the social factors contributing to liver cirrhosis, the subject of this work.

1.2 The Microanatomy of the Normal Liver

1.2.1 *The Lobule*

The liver contains an exemplarily complex microanatomy involving an intricate arrangement of distinct microstructures (**Figure 1.1**). The primary structural unit, the **lobule**, is thought to be composed of one **central vein**, which carries spent blood out of the liver. This vein is located in the center of the lobule, and multiple **portal triads** are arranged around the edges in an approximately hexagonal shape (**Figure 1.1 A**). Portal triads consist of **portal veins** that bring nutrient-rich blood from the intestine to the liver, **bile ducts** that carry the hepatic byproduct bile from the liver to the gallbladder, and **hepatic arteries** that transport oxygenated blood into the liver (**Figure 1.1 A**).

Bile ducts are tube-like structures comprised of biliary epithelial cells, or cholangiocytes, and are approximately the same diameter as the hepatic arteries (**Figure 1.1**). The biliary tree is a hierarchically branching structure, and the tiniest branches found at the single lobule level are the terminal bile ductules. [18] The blood vessels similarly branch hierarchically and resemble trees. The smallest vascular units at the single lobule level are the terminal hepatic arterioles, terminal portal venules, and terminal hepatic venules (central venules) (**Figure 1.1**). Portal tracts normally contain a small amount of supportive connective tissue made primarily of collagen type I. If the central venule is the center of the lobule hexagon, then the portal triads are the vertices, and the remaining space is the parenchyma (**Figure 1.1**). The liver parenchyma mainly consists of the primary functional cell type of the liver, the **hepatocyte** (**Figure 1.1**).

Hepatocytes are arranged within the liver as ‘cords’ one to two cell layers thick (**Figure 1.1 B**). Hepatocytes are polygonal cells about 25 to 40 um in diameter with central nuclei. [19] The cells can commonly contain two nuclei, a phenomenon called binucleation. [20] The liver is approximately 80% hepatocytes by volume, interwoven with microscale tube-like networks. [21] One crucial microscale network allows blood flow, and another allows the flow of the metabolic byproduct bile (**Figure 1.1 B**). Hepatocytes are a polarized epithelial cell, and the apical and basal domains perform different functions for these two fluid flow mechanisms. The apical surfaces of two neighboring hepatocytes will contact one another and form a tiny channel called the **bile canaliculus** (**Figure 1.1 B**). The canaliculi are where hepatocytes secrete bile, which then flows toward the bile ducts that eventually exit the liver to shuttle bile to the gallbladder. On the other side, the basal surfaces of the hepatocytes face the sinusoids through the space of Disse (**Figure 1.1 B**). [22] The sinusoids are the liver’s specialized capillaries, and blood flows from the portal triad to the central vein by percolating through the sinusoids, countercurrent to bile flow. Liver sinusoidal endothelial cells (**LSECs**) line the sinusoids and form the body’s most permeable endothelium, allowing blood products to contact hepatocytes for processing through the space of Disse (**Figure 1.1 B**).

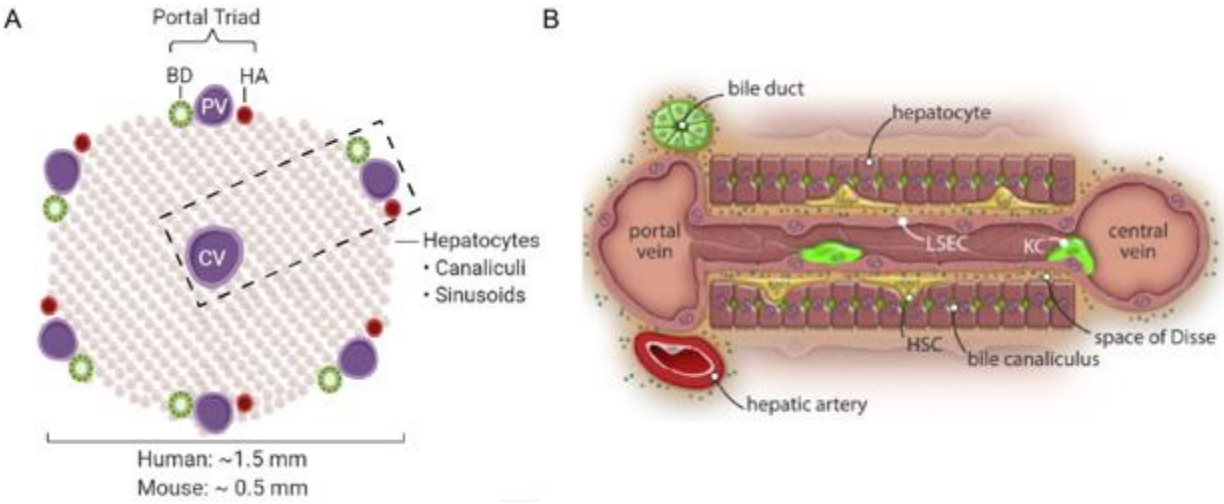

Figure 1.1. Normal liver architecture. (A) The liver lobule is comprised of a central vein (CV, purple) surrounded by multiple portal triads each containing a bile duct (BD, green), portal vein (PV, purple), and hepatic artery (HA, red). Blood flows from the portal triads toward the central vein, percolating through the sinusoids (white space). Hepatocytes (light brown cords) make up much of the parenchyma, and their apical domains will form bile canaliculi. Dashed box: portal-central axis **(B)** A zoomed-in view of a portal-central axis. Schematic shows more detail of polarized hepatocyte arrangement, including bile canaliculi (green dots) and LSECs (brown). HSC: hepatic stellate cell, KC, Kupffer cell. Adapted from [23].

1.2.2 *Structural and Functional Zonation*

The liver performs hundreds of discrete functions, from protein synthesis to drug metabolism. Remarkably, the tissue has evolved to diversify which cells perform what functions through a phenomenon called **zonation**. [24]

Structural and functional differences divide the lobule into three zones: zone 1, the periportal (near the portal vein) zone; zone 2, the midlobular or transitional zone; and zone 3, the pericentral zone (**Figure 1.2 A**). Zonation, therefore, depends on proximity to the portal or central vein. This portal-central framework - the zones themselves and the landmark vasculobiliary structures that allow their localization - is the **structural zonation** of the lobule. [25] This structure develops in part due to molecular gradients that form across the portal-central axis. For example, oxygen- and

nutrient-rich blood enters the liver through the portal triad, percolates through the sinusoids, and exits the liver via the central vein, which causes higher oxygen and solute concentrations on the portal side than the central. Since they are the primary metabolic cell type in the liver, zonation majorly affects hepatocyte function (**Figure 1.2 A**).

Functional zonation primarily involves hepatocyte drug and glucose metabolism and ammonia detoxification. [26] Some hepatocyte functions are not zonated, including the synthesis of abundant serum proteins like transferrin. [27] Glucose metabolism is a zonated function, with gluconeogenesis primarily periportal and glycolysis pericentral. [24] Another zonated liver function is ammonia detoxification, which converts ammonia to water-soluble urea for excretion. Periportal hepatocyte enzymes carbamoyl-phosphate synthetase (Cps1) and arginase (Arg1) convert ammonia to urea. Then, the pericentral enzyme glutamine synthetase (GLUL), a classic pericentral hepatocyte marker used in this dissertation, converts the leftover or excess ammonia. [28] Metabolism of drugs and other xenobiotics is another zonated function. Most xenobiotic metabolism occurs pericentrally; the cytochrome P450 enzymes that convert them into excretable metabolites are expressed primarily by pericentral hepatocytes. [29] Studies exploring liver zonation mechanisms suggest that the Wnt pathway may be the primary zonation-determining signaling pathway. [30] Wnt signaling induces the hepatic pericentral fate while repressing the portal, and the MAPK/ERK pathway has the opposite effect. [31] The division of labor afforded by zonation has likely evolved to allow the tissue to 1) efficiently perform hundreds of functions at once and 2) adapt quickly to nutritional requirements in various metabolic states. [32]

Though they are the primary metabolic cell, hepatocytes are not the only zonated cell type in the liver. Hepatocyte phenotype can affect nearby LSECs, so we must not ignore the zonation of the sinusoidal endothelium. [33, 34] In animal models, LSECs display zonated differences in

fenestrae (gaps or pores) size and surface molecules. [35, 36, 37] In humans, LSECs form two distinct subpopulations, Type 1 (zone 1 or periportal) and Type 2 (zones 2 and 3, or midlobular and pericentral) (**Figure 1.2 B**). [38] Type 1 LSECs line the first entry points where blood from the portal triads begins percolating across the lobule (**Figure 1.2 B**). CD36 expression marks them and is likely involved in the Type 1 cells' low-density lipoprotein-scavenging behavior (**Figure 1.2 B**). [39] Type 2 LSECs, on the other hand, are present in both the midlobular and pericentral zones (**Figure 1.2 B**). Markers expressed by Type 2 cells imply functions related to blood-derived leukocyte adhesion and antigen clearance (**Figure 1.2 B**). [38]

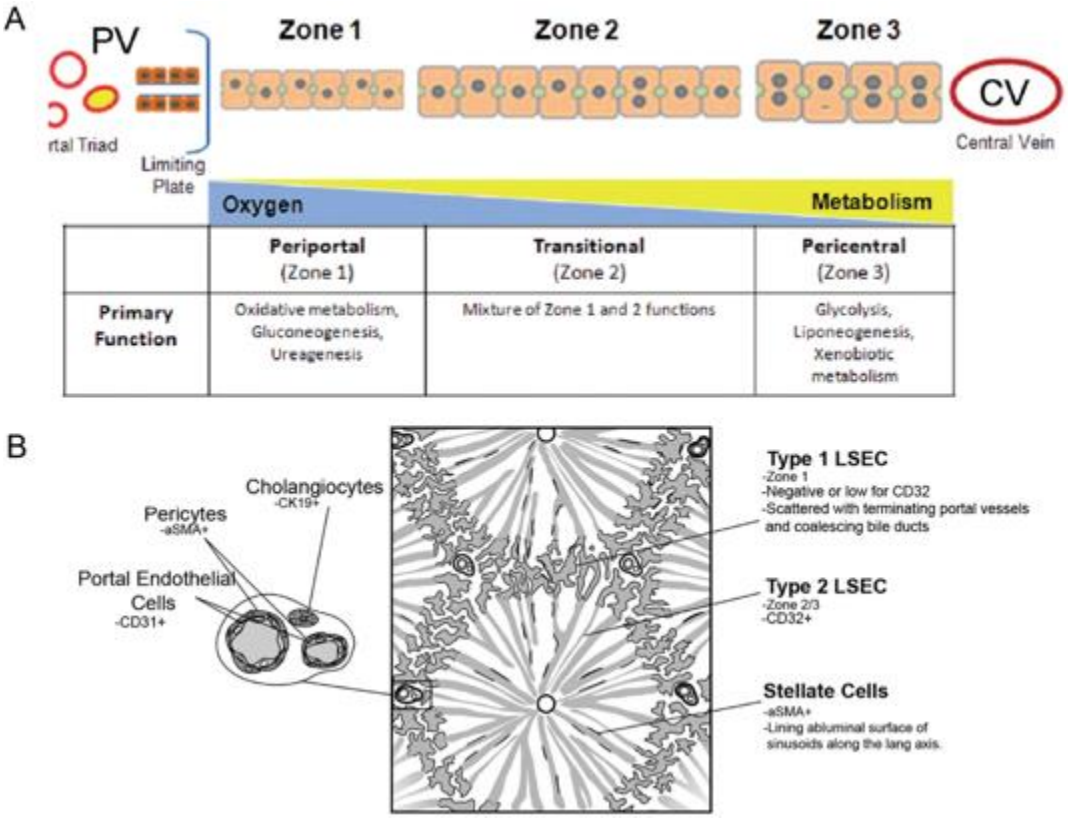

Figure 1.2. Normal liver functional zonation. (A) Functional zonation of hepatocytes (light brown/orange rectangular cells). Bile canaliculi: green dots between two adjacent hepatocytes. Note differences in cell size and nucleus number. Gradients of oxygen and metabolism are illustrated over a table describing zonated hepatocyte functions. PV: portal vein. Adapted from

[25]. **(B)** Schematic of the lobular organization and zonation of the sinusoids, highlighting immunohistochemical markers used in this study. Adapted from [38].

1.3 Liver Cirrhosis and Cirrhotic Microanatomy

1.3.1 *Liver Cirrhosis*

Liver cirrhosis, by definition, involves severe, pathologic structural changes. The gold standard for the diagnosis of cirrhosis is histology, revealing the presence of hepatocyte nodules surrounded by thick, fibrous bands of scar tissue. Chronic liver injury causes cirrhosis, and it can lead to end-stage liver failure. The only curative treatment for liver cirrhosis and end-stage liver failure is transplant, but demand exceeds supply, and an organ shortage leaves thousands of patients on the US transplant list each year. [40]

Many types of adverse stimuli can injure the liver, including drug and alcohol abuse, viral hepatitis, genetic disorders, and obesity. Among adult mammalian organs, the liver has the unique ability to regenerate in response to acute injury in a process involving cell proliferation and extracellular matrix (ECM) remodeling (**Figure 1.3 A**). Healthy regenerative ECM dynamics involve remodeling, synthesizing, depositing, and eventually removing ECM components, like collagen. This process is vital for liver regeneration in that it 1) allows the release of matrix-bound growth factors and signaling molecules involved in cell growth and 2) is critical for maintenance of cell placement within the tissue's intricate microarchitecture. [41] 'Tissue regeneration' is the reestablishment of tissue organization and function after injury **without** scar formation (**Figure 1.3 A**). [42] This definition illuminates how critical the transiency of ECM remodeling is, as scar tissue will indeed form if there is an imbalance in ECM degradation and deposition. The healthy liver can generally regenerate without incident, but this ability is not infinite, and chronic, repetitive injury will exhaust the liver's regenerative capacity.

Once the liver undergoes repetitive, chronic injury, it may enter a pathologic steady state called fibrosis (**Figure 1.3 B**). [3] Liver fibrosis is the presence of excessive ECM accumulation (scar tissue) and increased tissue stiffness. This scar tissue disrupts the critical microarchitecture of the liver. If liver injury ceases, the fibrosis may reverse, and healing may occur. [43] However, if the fibrotic state continues, the tissue can tip into the irreversible condition of cirrhosis, where the hepatic parenchyma is broken up into nodules by extensive fibrous bands of scar tissue. The scar tissue bands progressively crosslink, leaving it even harder for enzymes to degrade over time. [43]

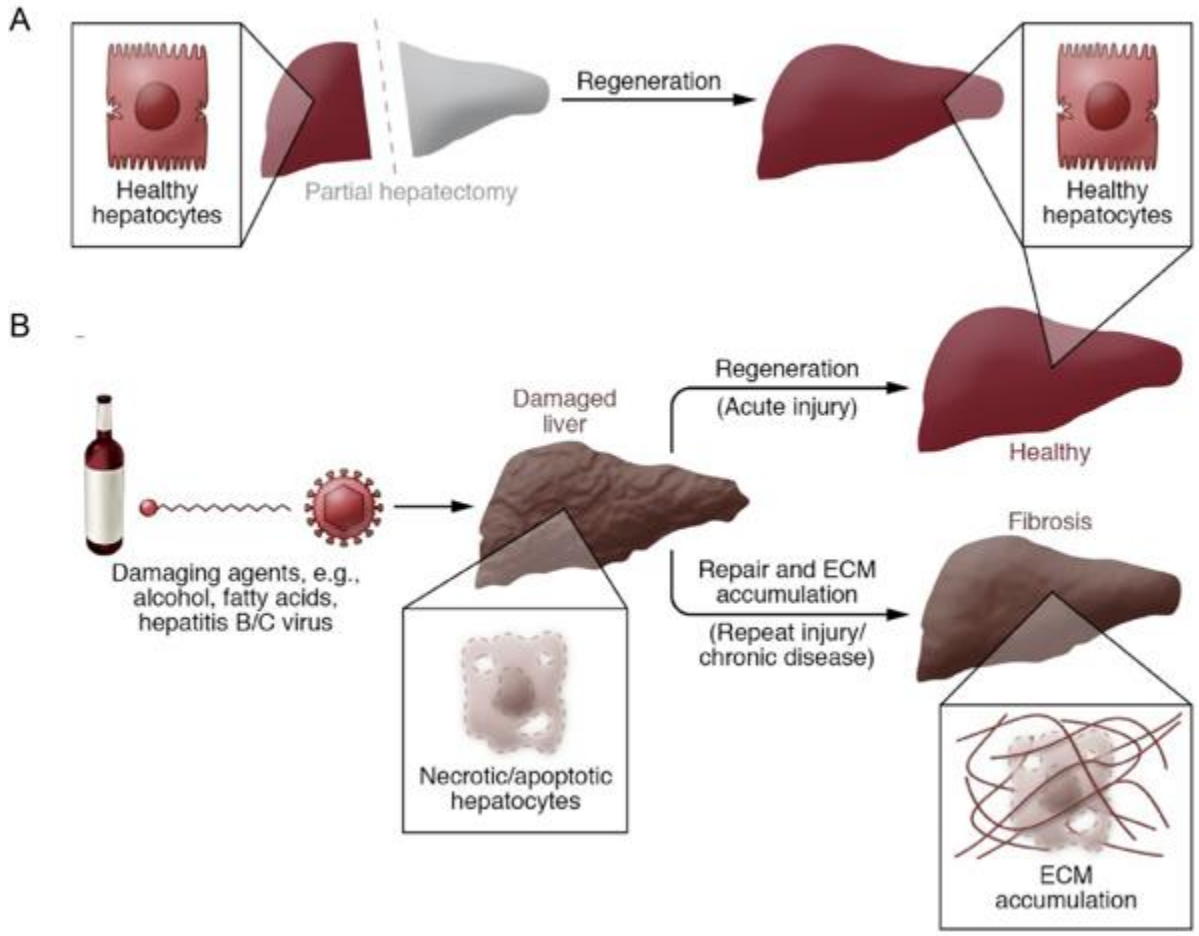

Figure 1.3. Liver regeneration and fibrosis. (A) As in the example of partial hepatectomy (left), healthy liver tissue can completely regenerate (right). **(B)** Liver regeneration in response to cell-damaging agents (left) can ultimately lead to regeneration (top right). However, chronic injury may lead to ECM accumulation and fibrosis (bottom right). This can ultimately progress to cirrhosis. Adapted from [3].

1.3.2 *The Lobule and Zonation in Cirrhosis*

Liver cirrhosis involves severe structural changes that rearrange the hepatic microanatomy and cause vascular changes. Here, we will examine those changes in the context of structural and functional zonation within the liver lobule (**Figure 1.4**). For diagnosing cirrhosis, biopsy-based

histology is the gold standard over less invasive imaging like magnetic resonance imaging (MRI), ultrasonography, and computed tomography (CT), simply because those other modalities are not sensitive enough to detect cirrhosis. They may detect changes that *imply* cirrhosis, like a rougher texture on the liver's surface or the presence of collateral veins. However, a biopsy is still needed to exclude causes other than cirrhosis. [44]

The liver's intricately organized microvasculature can become massively rearranged in liver cirrhosis (**Figure 1.4 A**). The portal and arterial blood supplies may directly shunt to the central vein rather than percolating through the hepatic sinusoids. This redirection can have severe consequences for the synthesis, and metabolism of blood products that usually occurs through exchange between the hepatocytes and the blood. [45] The sinusoids may change as well, further affecting blood flow. LSECs can lose their fenestrations in a process called capillarization, and the space of Disse that typically allows exchange with hepatocytes may come to contain scar tissue. [46] These changes can all cause increased blood flow resistance within the liver, leading to portal vein hypertension and are related to many organism-wide circulatory problems found in cirrhosis.

The bile ducts, similarly, can undergo significant changes during cirrhosis. Some cirrhosis cases will show destroyed ducts, like those from the autoimmune disease primary biliary cirrhosis, and bile may leak into the bloodstream if it is not successfully shuttled out of the liver. [47] Another, seemingly opposite, biliary phenotype is ductular reaction (DR) (**Figure 1.4 C**). DR resembles a proliferation of bile ductules and may be caused by the proliferation of cholangiocytes or hepatic progenitor cells or by transdifferentiation of hepatocytes. [48] The cell type of origin for the DR may depend on the underlying pathology that caused the cirrhosis. [48] Portal triad immune infiltrate is commonly found in samples with DR. [49]. Interestingly, the number of ductules in DR samples frequently correlates with an increased number of portal microvessels,

suggesting a close relationship between the different branching structures. [50] This link may not be surprising, considering that the biliary tree relies on the hepatic artery branches for much of its blood supply.

The hepatocytes are also affected by structural cirrhotic changes. The fibrous bands described as the hallmark of cirrhosis typically contain microvessels in addition to scar tissue. Many vascular changes already described occur by expanding the vascularized fibrotic septa that bridge the portal regions and central regions. These **fibrovascular septa** then isolate nodules of hepatocytes from the rest of the parenchyma (**Figure 1.4 A**). These hepatocyte islands frequently do not contain a central vein (**Figure 1.4 A**). [45] This change, therefore, can result in a complete dysregulation of the normal lobule architecture. Cirrhosis involves significant losses in hepatocyte function and, therefore, liver function and is a significant risk factor for the development of hepatocellular carcinoma and end-stage liver failure.

In agreement with the loss of structural zonation by dysregulation of the lobule architecture, functional zonation may also be altered in liver cirrhosis. For example, glutamine synthetase expression, which marks the first one or two pericentral hepatocyte layers, may be progressively lost altogether in fibrosis and cirrhosis (**Figure 1.4 B**). [51] Paradoxically, it is also possible for the cirrhotic liver to show robust and diffuse glutamine synthetase expression, an opposite phenotype but still with destroyed zonation. [52] In experimental cirrhosis in the rat, pericentral enzymes decrease more than periportal enzymes. [53] The loss of, and changes in, molecular gradients via fibrovascular rerouting of blood and bile flow may partially explain the loss of zonation observed in cirrhosis.

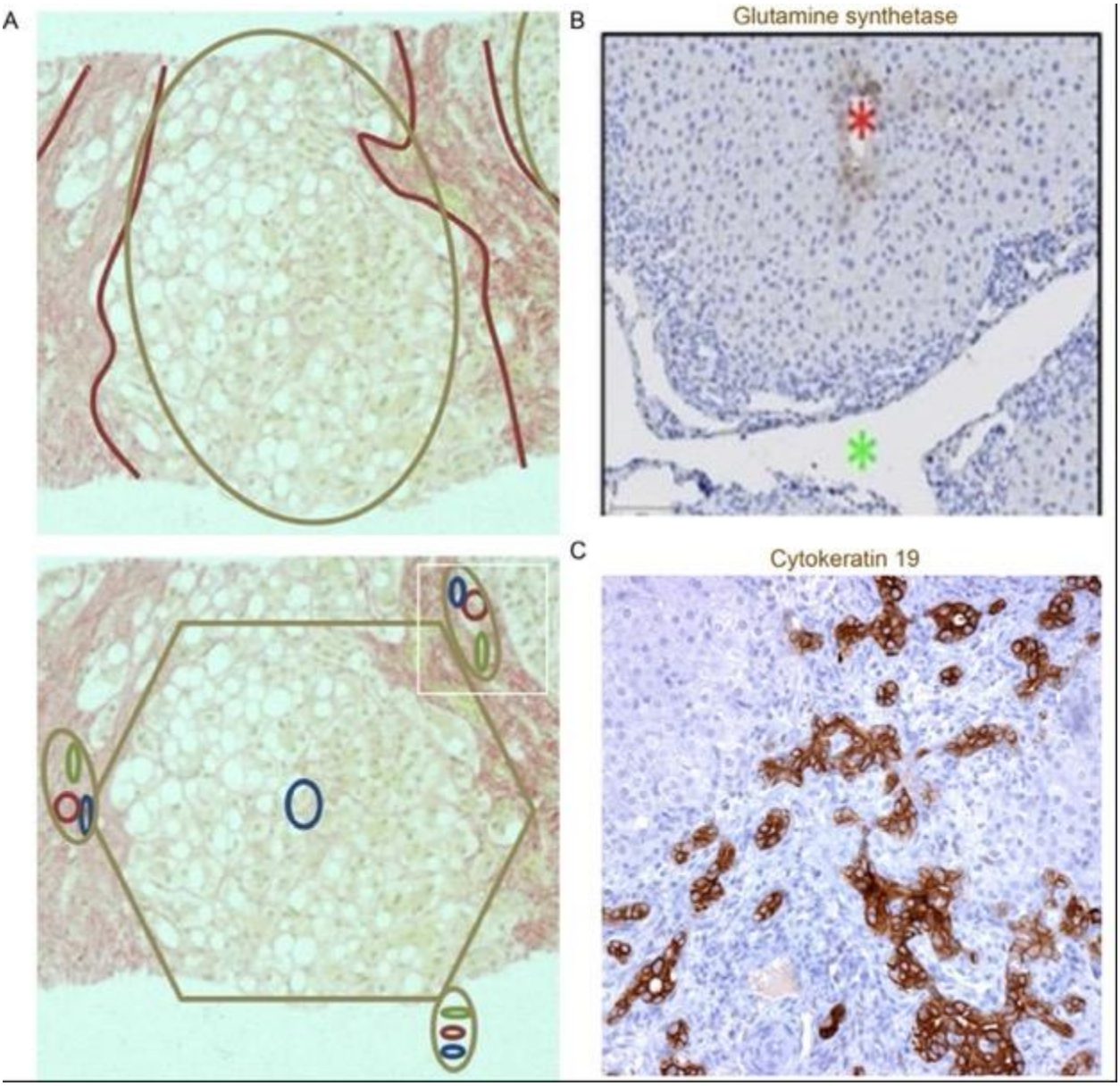

Figure 1.4. Dysregulation of cirrhotic structural and functional zonation. (A) Picrosirius red (collagen) staining of cirrhotic liver. Top: Red outline highlights fibrovascular septae, gold oval encircles hepatocyte nodule. Bottom: Classic lobule schematic overlayed on nodule, emphasizing absence of central venule and expansion of portal tracts in fibrous septae. Adapted from [54]. **(B)** Loss of pericentral markers, i.e. glutamine synthetase, is commonly reported in cirrhosis. Green asterisk: portal venule. Red asterisk: central venule. Adapted from [55]. **(C)** Classic cirrhotic ductular reaction presents with increased CK19+ cholangiocyte-like cells. These may or may not have patent lumens and may appear duct-like or as chains of single cells. Adapted from [50].

While we know much about the organization of these cell types and structures in two dimensions, studies are just beginning to explore how they are organized in three-dimensional space.

1.4 The Current State of the Art of Human Liver 3D Imaging

We know much about human tissue architecture and disease-induced remodeling from traditional 2D histology (for imaging small-scale structures) and contrast-based imaging for large-scale structures. Contrast-based imaging is now frequently visualized in 3D. It can be used to a resolution of about 0.5 mm per voxel, making it useful for structures on the scale of small veins or arteries but not for smaller vessels like venules, arterioles, or capillaries. Contrast imaging relies on the perfusion of contrast agents, so it can only be used to visualize the lumens of perfusable structures. 2D histology balances some of these limitations; microscopes have resolution limits in the nanometers, allowing visualization of some of biology's smallest structures, and tissue staining can be used to gather phenotypic and functional information, but only in two dimensions. These complementary imaging modalities have done much for the field of liver anatomy but leave a 3D resolution gap. Larger perfusable structures have been imaged in 3D but lack cell type information, while smaller structures and their cell types have been precisely visualized but mostly only in 2D. **Here, we begin to fill these gaps by using large-field 3D histology to empirically reconstruct human liver cell types and networks at the sublobular, lobular, and multilobular scales.**

While traditional histological methods have been valuable and provided centuries of anatomical data across many tissues and species, they are not without limitations (**Figure 1.5**). Cutting the tissue into thin sections can physically alter the structures to be examined. Cross-sections of tissue may miss sparse structures, and if structures are captured, their distribution throughout the actual 3D tissue may be misreported in 2D (**Figure 1.5 B-C**). Loops, branches, and

other complex structural events may be utterly unrepresented in 2D cross-sections; one continuous structure's loop or branch would appear to be multiple individual structures in cross-section (**Figure 1.5 A**). These limitations motivate 3D imaging of large samples to represent architecture and distribution more accurately, especially in intricately complex tissues like the liver. A technique that preceded tissue clearing to reconstruct 3D structures from 2D histology is the reconstruction of serial sections. These methods involve staining and imaging multiple consecutive individual tissue sections, then digitally aligning the sections and reconstructing the tissue as if it had not been cut. However, sectioning is still destructive and can cause tissue loss or structural damage at the interface of each slice, and reconstructing serial sections is very time- and labor-intensive, especially for samples over 100 um thick. [56]

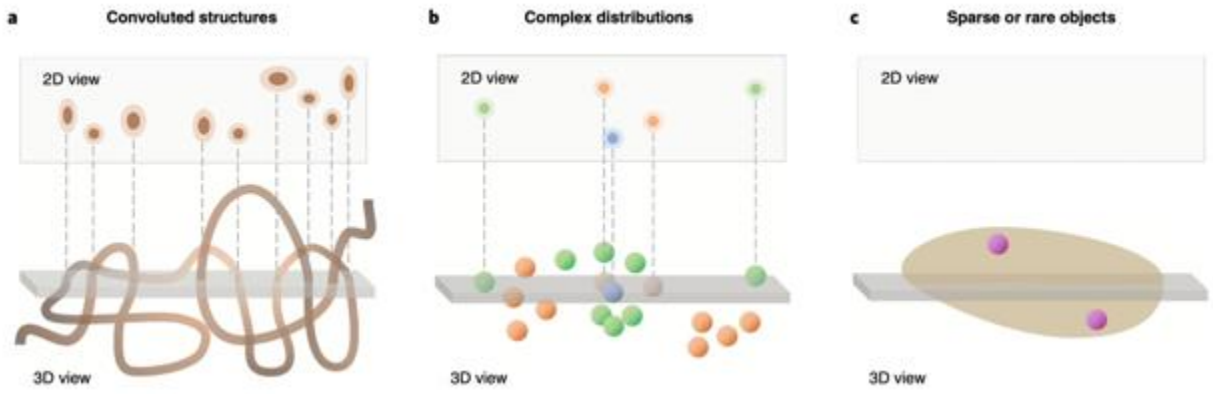

Figure 1.5. 2D histology misrepresents 3D structures. (A) One connected convoluted structure (3D view), like a vessel or duct, may appear as multiple disconnected objects in cross-section. **(B)** 2D sampling may inaccurately capture complex 3D spatial distributions, like zonated cells and structures. **(C)** Sparse or rare objects may simply not be included in 2D sections. Adapted from [57].

Some larger perfusable structures within the liver have been successfully imaged and reconstructed in 3D via modalities like MRI or CT (**Figure 1.6**). 3D scans like this can be used in surgical planning to estimate remaining liver volume after tumor excision. Vascular casting is a similar but *ex vivo* method where the perfusable vessels and ducts are filled with a resin. The tissue

is dissolved away, and the resin physical 3D model can be photographed, manipulated, and measured. However, these techniques have resolution limitations that leave the finer interlobular structures out of the picture. Further, while these methods can create beautiful 3D models, they only reconstruct the lumens of the perfusable structures and do not capture phenotypic or cell type information (**Figure 1.6**).

To overcome these limitations, groups have begun attempting to use 3D histology on diverse tissues including the liver. 3D histology typically involves two critical steps performed on thick tissues: staining and optical clearing. Tissue staining is traditionally done on sections about 5 um thick, which proteins (like antibodies) can penetrate within one hour. Small molecules (like the nuclear marker Hoechst used in this dissertation) can penetrate within five minutes. Efficient penetration of staining molecules matters greatly for tissue staining. For example, if a nucleus marker could not reach the tissue center, it may inaccurately appear as though there are no nuclei when the stain could simply not attach to the targets. 3D immunostaining of thick tissues requires chemical, time, and temperature changes to ensure satisfactory penetration of staining molecules. Whole-mount immunohistochemistry and similar techniques were popularized in fields requiring staining of intact brain and embryos. [58] The application of techniques that work in the brain, a very fatty tissue, may be ideal for tissue like the liver, which can contain lipid droplets. Specifically, lipids are hydrophobic and may preclude the penetration of antibodies and staining molecules diluted into the aqueous blocking buffers used in traditional staining techniques. The inclusion of dimethylsulfoxide (DMSO), an amphipathic molecule that can help to improve the solubility of polar and non-polar molecules, in all staining steps was found to improve penetration of blocking proteins, antibodies, and small molecules. [58, 59, 60] Chemical innovations like this, combined with increased incubation times to give molecules more time to penetrate tissue and

higher temperatures to increase diffusion speed, have enabled whole-mount immunostaining of numerous tissue types and informed the protocols developed in this dissertation.

If tissue can be stained deeply, then why can the traditional microscope not capture thick images? A primary reason for imaging depth limitations is light scatter, which in tissue is primarily caused by a mismatch of materials' refractive indices (RI). RI is a value that reflects how quickly light travels through a material. At the interface of two materials with different RIs, the light will appear to bend. For example, if a straight straw is placed at an angle within a glass of water, the observer may see the literal bending of light caused by the RI mismatch at the air-water interface – the straw will appear slightly bent at the point where it enters the water. Let us consider RI mismatch within a system more resembling cells and tissues. Cells are primarily water, with lots of proteins and lipids. Imagine shining a flashlight (the microscope's light) through a cube of gelatin, primarily made of proteins and water. The light may bend slightly or appear a bit weaker on the other side of the cube, but the light can shine through the gelatin. Now, imagine adding cream to the gelatin before it sets up. The flashlight's beam will be scattered entirely, and the cream gelatin appears opaque. Part of this phenomenon is due to refractive index mismatch. Cream is a colloidal suspension of fat particles in water. Many oils and fats have refractive indices of ~1.46, and water's RI is 1.333. The mixture of many densely packed fat droplets suspended within water leads to a light scattering effect. Light repeatedly bends as it passes through the suspension, bouncing off of fat droplets. The light can never get from the flashlight to the other side of the cube, as it is bounced around in all directions, leading the cream gelatin to have an opaque appearance. We emphasize that the mixture of lipid and water is responsible for the scatter, as we contrast this to observing light pass through pure fat, like a bottle of olive oil that appears transparent. Cells appear opaque to the eye and the microscope because of refractive index

mismatch between the water, lipids, proteins, organelles, and other materials that comprise the cells. Tissues, therefore, appear opaque as well. Optical tissue clearing techniques, which render the tissue transparent so that the microscope can "see" deeper in, are based on the principle of **matching refractive indices**. This matching is done by either removing high-scatter molecules like lipids or incubating the tissue in chemicals that cause the refractive indices of all materials to match. The tissue clearing method that we adapted and optimized for this dissertation work is the "clearing-enhanced 3D" (Ce3D) method. This method is aqueous (i.e., does not require tissue dehydration, which can warp structures), works by refractive-index matching, and was initially performed in lymph nodes and found to be compatible with many antibodies and fluorophores. [61] For those interested, there is a Nature Protocols publication describing the original method in more depth. [62]

At this point, multiple groups have established many protocols for immunostaining and clearing tissues. [63, 64, 65, 66] While diverse organs now have established clearing protocols, from soft tissue like intestine to hard tissue like bone and tooth, and even whole rodents and small non-human primates, the brain has been an organ of particular interest for groups establishing these protocols, specifically because of the complexity of the brain's structure-function relationships and the historical desire to follow neurons' processes across multiple anatomical regions. [67, 68, 69] 3D histology for the liver has not been as extensively optimized as the brain. Indeed, a study found that the brain stained and cleared greater than four times more efficiently than cell-dense tissues like the liver and the kidney. [70, 71] This illustrates the remaining need for published protocols that work robustly for thick liver samples (as in this dissertation), which are likely to work on similarly dense tissues like the kidney. It also provides a rationale for why most existing cleared liver studies were performed on relatively thin pieces of tissue from smaller model organisms.

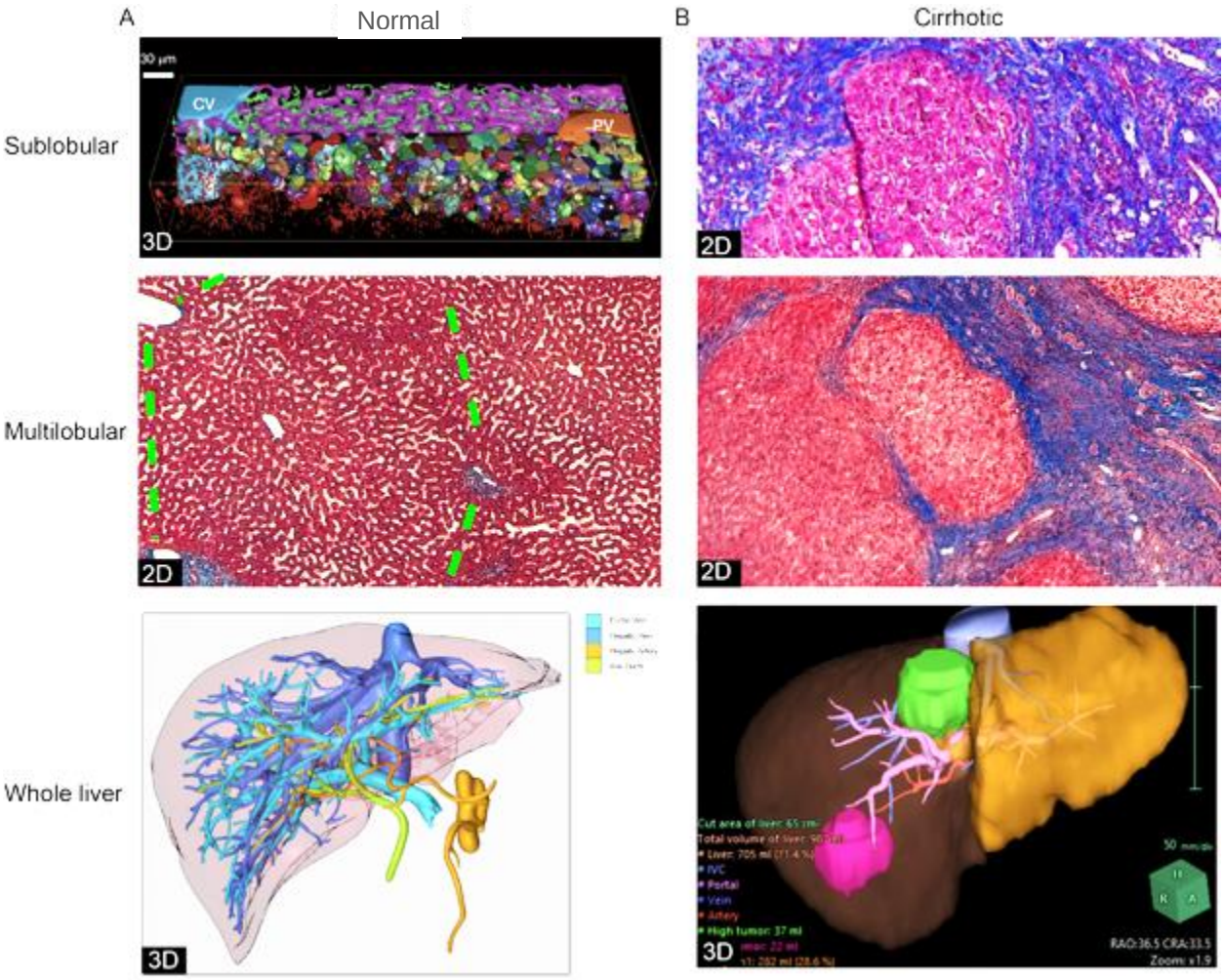

Figure 1.6. Graphical literature review: Multiscale 3D human imaging. (A) Representations of current imaging of the non-fibrotic human liver. Top: 3D model created from immunofluorescence showing a portal-central axis. Reconstructions include bile canaliculi (green) and sinusoids (magenta) in the rear, as well as lipid droplets (red) and nuclei (rainbow) in the front. CV: central venule. PV: portal venule. Adapted from [72]. Resolution limit of 3D method: ~200 – 500 nm. Center: Non-fibrotic human liver stained in 2D with Masson trichrome for cells (red) and collagen (blue). Dashed line highlights boundaries of one lobule. Bottom: 3D whole-liver imaging via CT and MRI is possible for perfusable bile ducts (green), and vasculature (cyan, blue, orange). Resolution limit of 3D method: ~0.5 mm voxel. Adapted from [73]. **(B)** Representations of current imaging of the cirrhotic human liver. Top: Cirrhotic human liver stained in 2D with Masson trichrome, zoomed to approximately same scale as A (top). Adapted from the Liver Fellow Network. Center: Cirrhotic human liver stained in 2D with

Masson trichrome, set to same dimensions as A (center). Note the lack of identifiable lobule architecture. Bottom: 3D whole-liver CT imaging of cirrhotic human liver with tumors (green, magenta). This imaging is used to predict final liver remnant volume post-hepatectomy (orange shading). Adapted from [74].

1.4.1 *Tissue clearing and the liver*

We performed a literature review to identify existing 3D human liver immunostaining publications. We first searched for studies with keywords like 'liver structure map' and '3D human liver imaging'. Most resulting publications were not directly relevant to this dissertation's methods, as they used techniques such as CT or MRI (as described above). We expect that this is due to the *in situ*, less invasive nature of those imaging modalities. 'Liver structure map' also returned studies related to MAP kinase signaling in the liver. To identify publications that performed 3D liver staining and, therefore, more accurately identify the body of literature to hold context for this dissertation, we needed to search for keywords like '3D human liver staining', 'liver 3d reconstruction antibody' or '3D human liver histology'. We also identified significant authors in the field and ensured we were familiar with their publications and citing works.

Early in the literature review, we noticed that the field of tissue clearing for 3D imaging of the liver is relatively new and that human-specific 3D imaging is exceptionally rare. The earliest publication identified here, where authors 3D-imaged 150 um-thick slices of mouse liver, was published in 2010. This work used 3D imaging of sublobular mouse structures, like sinusoids and nuclei, to infer a simulated lobule model during experimental (carbon tetrachloride-induced) regeneration. The model then predicted that daughter hepatocytes align to the closest sinusoid during regeneration. [75] This study was a big leap toward that group's goal of creating a 'virtual liver' to simulate and model things like physiologic processes and drug metabolism/pharmacokinetics. [76] It also provided methods and protocols that other groups used

and adapted to examine rodent liver in 3D. However, if we estimate the lobule to be a sphere, a human lobule contains about 25 times the volume of a mouse lobule. This difference may provide insight into why more groups have imaged the smaller organ, i.e., imaging, data, and time limitations, in addition to the ease of which rodent specimens are available compared to human.

All but two existing 3D liver staining studies were performed on non-human samples. Approximately ten imaged healthy mouse tissue, one on the acetaminophen-injured mouse, one on the CCl4-injured mouse liver, one on the mouse liver throughout bile duct ligation-mediated injury, and two studies compared rat tissue in health, fibrosis, advanced fibrosis, and cirrhosis. [75, 77, 78, 79, 80, 81, 82, 83, 84] Do we truly need to study the human liver to understand the human liver, or are these model organisms evolutionarily similar enough to make human imaging duplicative and unnecessary? It is known that functions like drug metabolism differ between humans and model organisms like rodents. [85] The physical size of the structures and lobule also differ significantly; the human lobule diameter is approximately three times larger than that of the mouse lobule. We may gain important insights about how nature patterns and engineers structures and networks by comparing the same organs of multiple species across such different size scales. Importantly, functional zonation is different in rodents than in humans. For example, the classically zonated marker for periportal mouse hepatocytes, E-cadherin, is not zonated in the human liver. [86] This pattern may imply a species-related difference in barrier function via E-cadherin-related adherens junctions, with mouse E-cadherin-mediated junctions concentrated at the portal region, the entrance to the liver, and human junctions more ubiquitously formed. [87] For these reasons, 3D imaging of the rodent liver cannot serve as a surrogate for a detailed reconstruction of the human liver.

3D histology techniques have just begun to be applied to the human liver. The most recent publication utilizing 3D immunostaining and tissue clearing in the human liver was published in 2020. [88]. The authors describe a method to immunostain and image human liver macrophages in 3D. Their motivation for working within 3D space was that 2D sections may not capture whole macrophage cells or show the vascular or biliary structures and how the macrophages are located in relation to them. Interestingly, this work also independently optimized the Ce3D clearing method for human liver pieces, the same clearing method utilized in this dissertation. They immunostained only one cell type, the macrophage, and reported that even with Ce3D clearing, their tissue had to be cut to 200 um thickness, the depth of approximately 40 traditional histology sections, to be successfully imaged. [88]

The one other publication staining the human liver in 3D was published in 2019 (**Figure 1.6 A, top left**). [72] This paper examined structural differences between normal control, healthy obese, steatotic, and early nonalcoholic steatohepatitis (NASH) liver samples. This sample set represents the clinical progression of fatty liver disease, a growing health problem. They identified morphological cellular and tissue changes that correlate with disease progression. They also found the 3D bile canaliculus network dysregulated in early NASH. Finally, they used fluid dynamic simulations to predict increased pericentral biliary pressure, consistent with elevated bile markers in the patients' blood. Their motivation for working in 3D space was that the complex architecture of the liver leaves it hard to infer the 3D organization of cells, canaliculi and sinusoid networks, and overall tissue structure from 2D histology. [72] This paper was impactful in that they identified a possible new aspect of liver pathobiology in NASH. However, the paper focused only on the microscale structures, the canaliculi and sinusoids, and largely ignored the larger microvessels and bile ductules (**Figure 1.6 A, top left**). Their tissue was sectioned to 100 um thick, approximately

the depth of 20 traditional histology sections. They utilized a portal-central axis as a surrogate for the liver lobule rather than extending their image field in the x and y dimensions to capture the whole lobule. These decisions worked in the context of the microscale canaliculi and sinusoids; a 100 um-thick subsection of the lobule may contain enough tiny structures to represent the overall network. However, they leave the 3D organization of the critical larger microvessel and ductule networks unexplored (**Figure 1.6**).

In summation, the human liver lobule has never been fully imaged in 3D, in neither the x-y plane nor the z dimension, as far as we are aware (**Figure 1.6**). Therefore, the existing body of work in the liver histo(patho)logy field leaves the empirical 3D human liver lobule un-reconstructed, including functional and structural zonation (**Figure 1.6**). The field has also not explored the 3D network organization of microvessels larger than capillaries or biliary structures larger than canaliculi and has not examined how these critical human liver structures and cell types change in cirrhosis (**Figure 1.6**).

1.5 SUMMARY

The healthy liver has a complex architecture integral to its homeostasis; many liver diseases are associated with structural changes that impair blood flow, bile clearance, and overall organ function. Scientists have historically studied liver structure using traditional two-dimensional histology and three-dimensional contrast-based computed tomography (CT). These methods leave a resolution gap where there is cell-type specific information in only two dimensions and three-dimensional information from only the perfusable, contrast-injectable structures. The cell-level 3D structure of the human liver has not been empirically defined. Further, traditional histology requires tissue sectioning, which can physically alter the structure. The 2D nature of the

visualization can make convoluted structures appear distinct, e.g., a cross-section of one winding vessel may look like two or more separate vessels.

To overcome these limitations, groups have recently begun imaging thick liver samples via 3D immunostaining and tissue clearing, which render the tissue optically clear and permit deeper imaging than traditional methods. Most of this work was done on rodent liver, and the few human liver studies have imaged less than one functional unit (lobule) to a depth of only a couple hundred microns. Here, we have surpassed existing 3D human liver mapping attempts by imaging approximately 200 times their captured tissue volume. We acquired non-fibrotic and cirrhotic human liver and applied 3D immunostaining to label sinusoidal endothelial cells, pericentral hepatocytes, biliary epithelial cells, endothelial cells, and smooth muscle cells. Liver-optimized optical clearing permitted acquisition of microscope images to a depth of approximately 500 um, a 2.5-fold depth improvement over previous 3D liver studies.

For the first time, the entire functional unit of the human liver has been visualized in three dimensions, allowing the reconstruction and characterization of its unevenly distributed and convoluted structures. Comparative analysis of healthy and diseased tissues has identified pathologic changes in 3D bile duct networks and 3D blood vessel networks, previously not histologically studied in three dimensions. We also find volumetric differences in central functional zonation, identifying a ‘decentralization’ phenotype of the cirrhotic human liver. These results provide a more holistic, empirical view of the three-dimensional architecture of the human liver and its disease-induced adaptive remodeling. These studies may enable more accurate modeling and engineering of 3D human liver tissue and provide new insights into the (patho)biology of the human liver.

Chapter 2. MULTIPLEXED 3D IMMUNOSTAINING, CLEARING, AND IMAGING OF THE HUMAN LIVER

2.1 INTRODUCTION

The intricate microstructure of the liver is critical for its health and function. While 2D histology has allowed interrogation of tissue structure for centuries, advances in histological techniques, microscopy, and computing now allow for the expansion of histology to the third dimension. 3D imaging of the liver is vital because of the tissue's unevenly distributed (zonated) features and many convoluted tube-like networks, which can be misrepresented in traditional 2D histology.

The rodent liver has been explored via 3D immunostaining for over a decade, but primarily on relatively thin tissue sections of approximately 100-200 um thickness. The rodent liver lobule is about an order of magnitude smaller than the human lobule. Existing human liver 3D imaging studies have imaged less than an entire lobule, partially due to this large size. The human liver has been imaged at 100 um thick or less, similar to the rodent studies. Imaging at this scale has allowed the study of 3D microscale networks like canaliculi and sinusoids, unveiling new cholestasis-like changes underlying fatty liver disease. [72] However, previous imaging limitations have precluded exploration of the 3D dynamics of larger networks like the ductules and blood vessels. [88, 72] Therefore, **we hypothesize that combining tissue-optimized staining and clearing with large-field, overnight 3D imaging enables mapping the human liver across multiple lobules.**

To expand hepatology's understanding of the 3D organization of liver microstructure, we sought to map critical multiscale vascular and biliary structures across multiple human liver lobules. To do this, we aimed to use immunostaining and small molecule labeling to empirically define diverse hepatic cell types and structures deep within the tissue and then optically clear the

tissue to permit deep microscopy. The liver can be more challenging to deeply stain and clear than other tissues, presumably because of high cell density. [70] Here, we overcame technical limitations of existing 3D liver staining and clearing methods to allow for deeper and broader labeling and imaging by optimizing the Ce3D method for liver samples. [61] We identified and optimized a panel of antibodies and small molecules robustly compatible with the human liver and the Ce3D clearing method. This panel successfully marks pericentral hepatocytes (i.e., functional hepatic zonation), nuclei, cell membranes, bile canaliculi, Type 2 sinusoidal endothelial cells (i.e., functional vascular zonation), bile ducts (i.e., structural zonation), vascular endothelial cells, and smooth muscle cells. We could image small fields at high resolution to visualize and model the microscale human structures and networks. We then explored the hypothesis that expanding our imaging field at lower resolution would capture whole-lobule and multilobular 3D images of the human liver. We utilized these 3D images to create 3D models of the human liver with which to further the field's understanding of the tissue's intricate microstructure. Here, we establish that deep immunolabeling, tissue clearing, and large-field confocal imaging can be used to map vasculobiliary networks and zonated features across multiple human liver lobules.

2.2 Materials and Methods

2.2.1 *Human liver samples*

Living donors undergoing oncologic surgery with no underlying fibrosis provided liver samples via partial hepatectomy. To preserve the donated tissue, samples were sliced with a vibratome to a thickness of two millimeters and fixed immediately in 4% paraformaldehyde for up to one week at 4°C and then moved to phosphate-buffered saline (PBS) at 4°C. All participants provided written informed consent. All de-identified human specimens were obtained from a Biorepository. The study protocol was approved by the institutional review board (A Repository

for the Study of the Pathogenesis and Treatment of Liver Tumors. University of Washington STUDY00001852) before study commencement.

2.2.2 *Whole-mount staining of human liver biopsies with antibodies & small molecules*

To identify proteins of interest within thick tissue via **immunostaining**, we used a customized version of the Ce3D protocol. [89] Samples were first punched into six-millimeter discs using biopsy punches, washed in fresh PBS for one hour, and then blocked in Ce3D alternative blocking buffer (1x B.D. Perm/Wash buffer + 1% [w/v] bovine serum albumin + 1% [v/v] normal donkey serum + 0.3% [v/v] Triton X-100 in PBS) overnight at 37°C with gentle shaking. 6 mm biopsy punches were chosen as a tissue size large enough to contain four-to-six human lobules each but small enough to be stained efficiently with ~5 uL primary antibody per sample and be imaged overnight at 10x resolution. Larger samples would have been cost- and time-prohibitive.

To mark proteins of interest, samples were incubated with primary antibodies diluted 1:100 (except anti-SMA at 1:500) in Ce3D alternative blocking buffer with 5% (v/v) dimethyl sulfoxide (DMSO, a penetration enhancer) for 24 hours at 37ºC with gentle shaking (Table 2.1). If primary antibodies were fluorophore-conjugated, we began light protection with aluminum foil to prevent bleaching. Samples were then washed with Ce3D wash buffer (0.2% [v/v] Triton X-100 + 0.5% [v/v] 1-thioglycerol in PBS) for six to eight hours at room temperature with gentle shaking, changing the buffer every two hours, to remove excess primary antibody molecules. To make the proteins of interest visible via fluorescence, washed samples were then incubated in fluorophore-conjugated secondary antibodies diluted 1:400 in Ce3D alternative blocking buffer with 5% (v/v) DMSO and 1:400 Hoechst 33342 overnight at 37ºC with gentle shaking and were protected from light. If utilized for cell membrane staining, the fluorescent **small molecule** phalloidin (Thermo Fisher A12379) was added at this step at a 1:100 dilution. To remove excess fluorescent molecules,

samples were washed in Ce3D wash buffer for six to eight hours at room temperature with gentle shaking, changing the buffer every two hours.

Table 2.1. Key Resources Table - Antibodies and Small Molecules

ANTIBODY/SMALL MOLECULE	SOURCE	IDENTIFIER
Alexa Fluor 488 Phalloidin	Thermo Fisher	Cat#A12379
Hoechst 33342	Thermo Fisher	Cat#H3570
Hoechst 33258	Thermo Fisher	Cat#H3569; RRID: ab_2651133
Rabbit monoclonal anti-CK19 (clone EP1580Y)	Abcam	Cat#ab52625; RRID: AB_2281020
Mouse monoclonal anti-CD31 (clone JC/70A)-DyLight 550	Novus	Cat#NB600-562R
Rabbit polyclonal anti-CYP2E1	Abcam	Cat#ab28146; RRID: AB_2089985
Goat polyclonal anti-CD32b	R&D Systems	Cat#AF1330; RRID: AB_354737
Mouse monoclonal anti-GLUL (clone GS-6)	Sigma	Cat#MAB302; RRID: AB_2110656
Rabbit monoclonal anti-MRP2 (clone EPR10997(2))	Abcam	Cat#ab187644
Mouse monoclonal anti-aSMA (clone 1A4)	Sigma	Cat#A2547; RRID: AB_476701
Donkey anti-Rabbit, Alexa Fluor 647	Invitrogen	Cat#A31573; RRID: AB_2536183
Donkey anti-Rabbit, Alexa Fluor 488	Invitrogen	Cat#A21206; RRID: AB_2535792
Donkey anti-Rabbit, Alexa Fluor 594	Invitrogen	Cat#A21207; RRID: AB_141637
Donkey anti-Goat, Alexa Fluor 647	Invitrogen	Cat#A21447; RRID: AB_141844
Donkey anti-Mouse, Alexa Fluor 555	Invitrogen	Cat#A31570; RRID: AB_2536180
Donkey anti-Mouse, Alexa Fluor 488	Invitrogen	Cat#A21202; RRID: AB_141607

2.2.3 *Optical clearing of cell-dense tissue*

To reduce water transfer, which would change the RI, samples were briefly dried after washing and quickly transferred to Ce3D clearing solution (22% [v/v] N-methylacetamide, 80% [w/v] Histodenz, 0.1% [v/v] Triton X-100 in PBS) with Hoechst 33342 (1:400 dilution) for overnight incubation at 37ºC with gentle shaking. The overnight incubation allows for

equilibration of the Ce3D clearing solution and water within the sample. The sample is then transferred to a larger volume of new Ce3D clearing solution in the morning for long-term, light-protected storage at room temperature to enhance clearing. We find that overnight incubation results in tissue clearing that allows visualization of a few hundred microns of thickness and is still cloudy to the eye. However, longer incubations till the tissue is as clear as stained glass allows microscopy of up to > 1 mm of thickness, depending on the sample.

2.2.4 *3D confocal imaging and image processing*

To view the fluorescent structures of interest, liver samples were placed on glass-bottom dishes with enough Ce3D clearing solution to cover the piece and covered with a coverslip to keep flat and reduce water evaporation and sample movement. Imaging was performed on a confocal laser scanning microscope (Leica TCS SP8). Available objectives included a 10x 0.4 numerical aperture (N.A.) dry objective, 20x 0.75 NA dry objective, and 63x 1.4 NA oil objective (Leica). Hoechst, Alexa Fluor 488, Alexa Fluor 555/594 or DyLight 550, and Alexa Fluor 647 were excited with 405, 488, 552, and 638 lasers, respectively, and detected with hybrid detectors (HyD).

Z-stacks were acquired through Leica Application Suite X (LAS X) software (Leica Microsystems). To ensure full-depth signal capture across the entire sample, the bottom of the stack was set ~5 um below the start of the visible signal. We added ~5 um to allow for any sample settling or overnight movement. The top of the stack was ended at the end of the visible signal, using Z-compensation within LAS X to increase laser power and gain throughout the stack as necessary to a maximum of 5% laser power and 100% gain. 5% laser power was chosen as a maximum to prevent bleaching. To cover the 6 mm biopsy punches, the 10x objective was used, and tiles of approximately 4 x 4 image stacks were stitched using the Mosaic Merge function within LAS X.

Images were converted to Imaris image format (.ims) using Imaris File Converter 9.3.1 (Oxford Instruments) and visualized within Imaris 9.3.1 (Oxfored Instruments) in 3D View or Slice Mode. Automatic Surface creation mode was used to reconstruct microscale structures (cell membranes, canaliculi, sinusoids, hepatocytes). Surface creation mode was used manually to reconstruct 3D models of mesoscale structures (venules, arterioles, ductules).

To plot pixel intensity across regions of interest as a 3D projection, we used FIJI with the Interactive 3D Surface Plot plugin (Barthel, Kai Uwe). [90]

2.3 RESULTS

2.3.1 *An optimized pipeline for reconstructing human liver tissue.*

To enable large-scale microscopic 3D visualization of human liver tissue, we developed a customized pipeline involving immunostaining, tissue clearing, and confocal imaging (**Figure 2.1**). First, the non-tumor liver is excised from patients undergoing partial hepatectomy. Samples are dissected at least two centimeters away from any present tumor, a distance at which tissue is expected to be free from field effect (**Figure 2.1 A**). [91, 92] These liver samples are then sliced to a thickness of 2 mm via a vibratome and fixed in paraformaldehyde (**Figure 2.1 B**). After rinsing, samples are punched into 6 mm discs with biopsy punches, a size expected to contain approximately four to six human lobules (**Figure 2.1 B**). Samples are then stained with antibodies or small molecules and cleared via Ce3D, resulting in thick, transparent samples of the human liver that can be imaged at high resolution with a confocal laser scanning microscope (**Figure 2.1 C**).

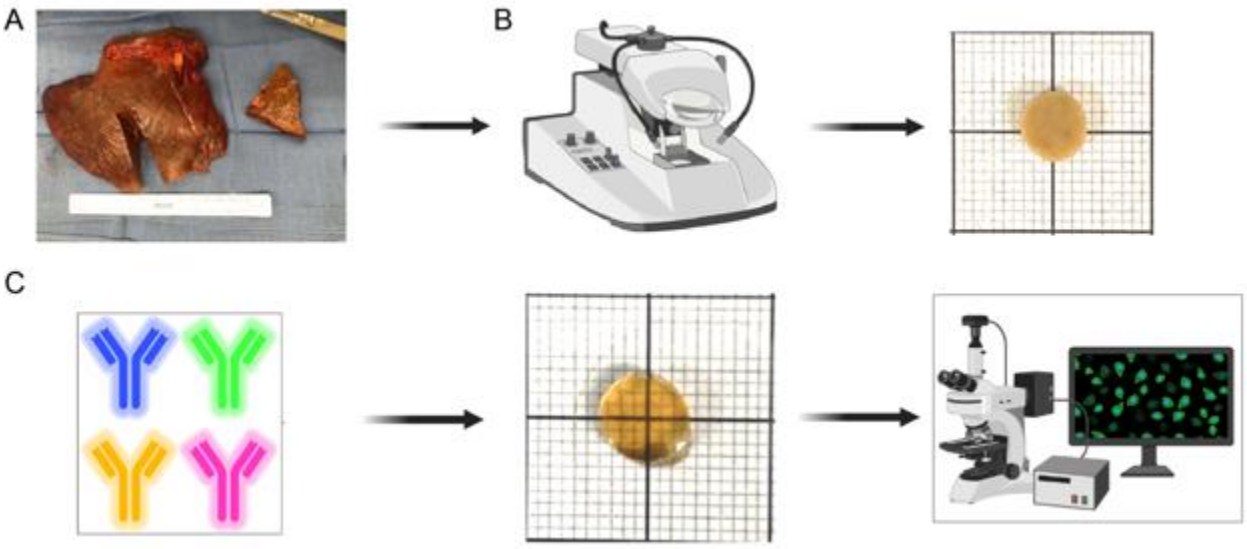

Figure 2.1. Schematic of the 3D liver mapping pipeline. (A) Partial hepatectomy of human liver, including tumor (rear) and representative non-tumor liver utilized for these studies (right, excised). **(B)** Tissue was sectioned with a vibratome (left) into 2 mm-thick slabs and punched into 6 mm-diameter rounds with biopsy punches (right). Note opacity of sample. **(C)** Liver was stained with up to four markers at a time (left), represented here by fluorescent IgG molecule schematics colored for their corresponding wavelengths (blue, green, orange/red, far-red [magenta]). Tissue was then optically cleared (center). Note the tissue transparency and the stained-glass appearance due to remaining brown pigmentation of the cells. Finally, tissue was imaged via confocal microscopy (schematic, right).

2.3.2 *Deep fluorescent labeling and 3D imaging of cell-resolution hepatic structures.*

Once we established our pipeline, we identified panels of antibodies and small molecules to stain diverse multiscale structures deeply (**Figure 2.2**). Our goal was to unveil the empirical 3D organization of the liver's intricate microanatomy. To do this, we first applied our liver mapping pipeline to visualize a range of established markers across sublobular liver structures and cell types. Our pipeline resulted in robust 3D visualization of microscale structures like pericentral hepatocytes (GLUL and CYP2E1), nuclei (Hoechst), cell membranes (phalloidin), bile

canaliculi/apical membranes (MRP2), and Type 2 sinusoids/basal membranes (CD32b) (**Figure 2.2**).

One of the first cell types of interest for liver mapping was the **hepatocyte**. Specifically, we aimed to mark pericentral hepatocytes to enable visualization of human zonation patterns in 3D. Immunostaining of GLUL, a pericentral enzyme involved in ammonia metabolism, revealed the layer of hepatocytes surrounding each central venule (**Figure 2.2 A**). By viewing one optical section captured by the microscope, we can approximate a traditional 2D tissue section (**Figure 2.2 A**, top left). This representative image revealed two distinct central venule lumens ringed by GLUL+ hepatocytes (**Figure 2.2 A, top left, asterisks**). We uncovered one utility of 3D imaging by viewing a top-down, horizontal (*en face*) maximum intensity projection (MIP) of the sample (**Figure 2.2 A, bottom**). Here, 3D visualization revealed that these two cross-sectional lumens were two ends of one connected central venule (**Figure 2.2 A, bottom**). We also found that CYP2E1, a pericentral drug metabolism enzyme, provides robust visualization of pericentral hepatocytes (**Figure 2.2 A, top right**). While GLUL marks the layer of hepatocytes adjacent to the central venule, CYP2E1 has a more gradient morphology. It brightly stains hepatocytes within the central region and fades toward the portal region. Here, we selected an *en face* MIP from a representative pericentral field to emphasize the hepatocytes' staining morphology (**Figure 2.2 A, top right**).

To visualize the 3D organization of hepatic **nuclei**, we used the well-established marker Hoechst 33342 (**Figure 2.2**). We found that three-dimensional visualization of nuclei reflects the high cellularity of the liver and provides some cell type information at higher resolutions (**Figure 2.2**).

To examine human liver cells' 3D organization, we stained **cell membranes** with fluorescent phalloidin, a peptide that binds to the abundant cytoskeletal protein F-actin. Though this is not a cell-type-specific marker, approximately 70% of the cells within the liver are hepatocytes. [21] We found that 3D phalloidin staining provides a detailed reconstruction of the liver's cell membrane organization (**Figure 2.2 B**). By examining 3D high-resolution membranes as an *en face* MIP, we observed that the highly complex arrangement of liver cell membranes appears mesh-like (**Figure 2.2 B, top**). By segmenting the cell membranes, reconstructing them into a 3D model, and viewing the perpendicular plane, we found that the mesh-like network is primarily composed of cells with polygonal membranes resembling hepatocytes (**Figure 2.2 B, bottom**). This 3D model of the membrane network allows visualization of distinct neighboring cell membranes (**Figure 2.2 B**, **bottom, arrowheads**). The model unveiled small intercellular spaces, which we hypothesized are bile canaliculi (**Figure 2.2 B, bottom, arrowheads**) (**Supplementary Video 1**).

We adapted our 3D imaging technique to examine this hypothesis and view the organization of the **bile canaliculus** network (**Figure 2.2 C**). Multidrug resistance-associated protein 2 (MRP2) is a protein expressed on the canalicular membrane of hepatocytes that facilitates the efflux of bile salts. [93] We found that this marker unveiled the 3D mesh-like network of bile canaliculi (**Figure 2.2 C, top**). Segmenting the canaliculi and reconstructing a 3D model allowed appreciation of the 3D network from a perpendicular view (**Figure 2.2 C, bottom**). This representative side view was rainbow-coded for the position in the Z dimension; canaliculi at the top of the stack were red, and the bottom of the stack was blue. We observed that the software coded the green network that spanned most of this representative image as one green structure because it was one connected network – the unbroken structure was color-coded as the median height. We established that MRP2

immunostaining allows visualization of the human canaliculus network and its connectivity in 3D (**Figure 2.2 C**) (**Supplementary Video 2**). We did confirm the hypothesis that the intercellular spaces found with phalloidin staining are canaliculi by co-staining MRP2 and phalloidin (**Supplementary Video 2**).

We next used our staining, clearing, and imaging process to reveal the zonated **sinusoid** network's 3D organization (**Figure 2.2 D**). CD32b is a protein found on Type 2 LSECs and is thought to be involved in antigen clearance. [94, 38] Type 2 LSECs are found mostly in the midlobular and pericentral zones. [38] We found that CD32b can be used to examine the 3D organization of the sinusoid network (**Figure 2.2 D**). Here, we observed the mesh-like intricacy of the sinusoid network (**Figure 2.2 D, top**). We found that the 3D nature of the network can be examined by segmenting the sinusoids, reconstructing them as a 3D model, and viewing perpendicularly (**Figure 2.2 D, bottom**). We observed that CD32b+ LSECs form lumens (asterisks), visible here in cross-section (**Figure 2.2 D**, **bottom**). The sinusoids appear to intertwine in 3D with the hepatic cords (black spaces) (**Figure 2.2 D, Supplementary Video 3**).

To examine the complex spatial relationship of the micro-transport structures, we combined these techniques to visualize the 3D canalicular and sinusoidal networks in the same sample (**Figure 2.2 E**) (**Supplementary Video 4**). The canaliculi and sinusoids exist on opposing poles of the hepatocyte membrane. We observed this relationship in 3D, shown here as a representative perpendicular MIP of fluorescence (**Figure 2.2 E, top**) and an angled 3D reconstruction (**Figure 2.2 E, bottom**). The sinusoid lumens were visible within a few optically sectioned vessels (**Figure 2.2 E, bottom, top of image**). We found that the canalicular and sinusoidal meshes keep a consistent distance from one another as they weave through 3D space. This representative image

also shows a left-handed helical twist in both networks, which could be an artifact of sample alignment during dissection or imaging (**Figure 2.2 E**).

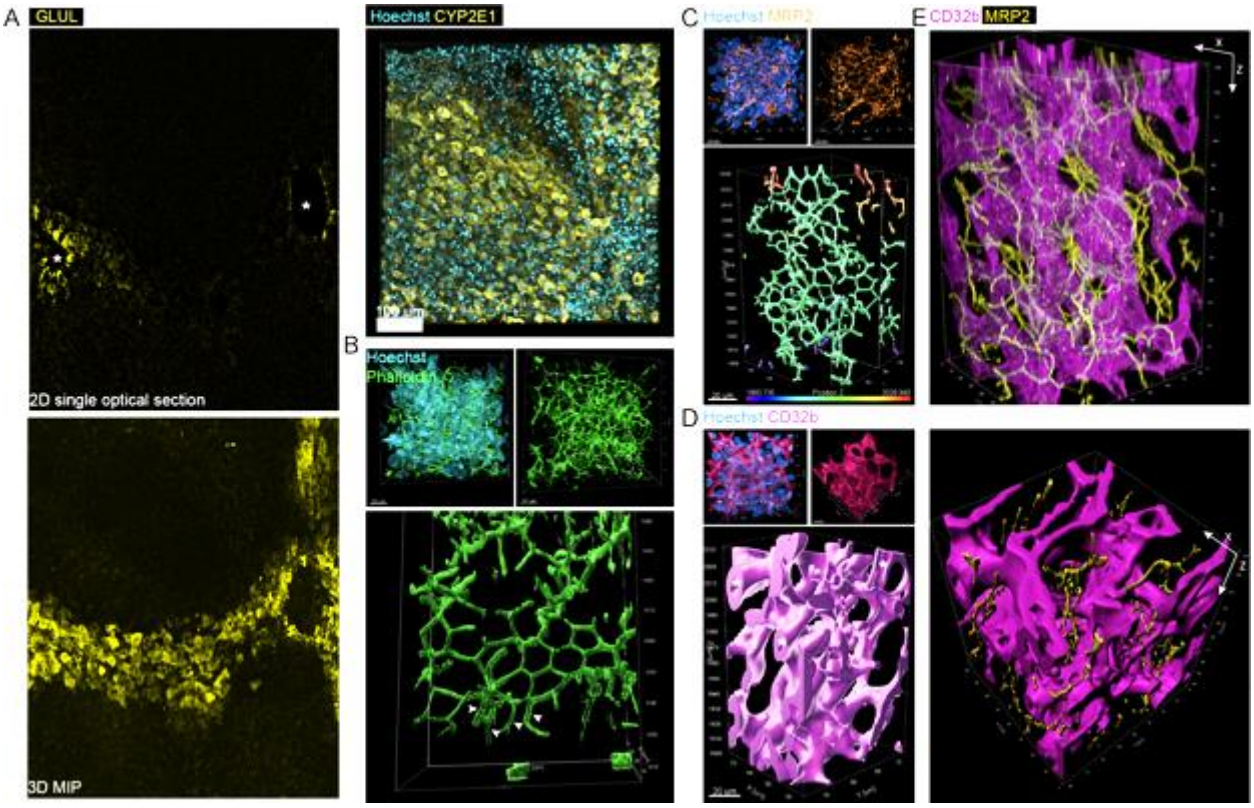

Figure 2.2. Deep labeling and 3D imaging unveils volumetric microscale human liver structures and networks. (A) Immunolabeling of pericentral hepatocytes. *Left:* A representative single 2D optical section of GLUL+ hepatocytes (yellow) shows two separate central venules (top, asterisks). An *en face* MIP of the same field (bottom). *Right:* CYP2E1 (yellow) *en face* MIP from a representative pericentral tile. Cyan: Hoechst. **(B)** Phalloidin (green) marks cell membranes. *Top:* 100 um-thick *en face* MIP from a representative tile. *Bottom:* Side view of 3D model of same tile. Dilated spaces between two adjacent hepatocyte membranes are likely to be canaliculi (arrowheads). **(C)** Immunolabeling of bile canaliculi. MRP2 (orange) marks the apical membranes of hepatocytes. *Top:* 130 um-thick *en face* MIP from a representative tile. *Bottom:* Side view of 3D model of same tile. Model shows the net-like 3D structure of bile canaliculus network. Statistical pseudo-coloring color-codes structure based on Z position; bottom structures are blue and top structures are red. Green structure is an unbroken canaliculus network. **(D)** Immunolabeling of Type 2 sinusoids. CD32b (magenta) marks the majority of LSECs. *Top:* 130

um-thick angled MIP of representative tile. *Bottom:* Angled side view of 3D model of the same tile. Model reveals the mesh-like 3D network structure of the sinusoids. Sinusoidal lumens are visible (asterisks). **(E)** Co-staining of microscale transport structures. CD32b (magenta) marks Type 2 LSECs and MRP2 (yellow) marks canaliculi. *Top:* 130 um-thick perpendicular MIP of representative tile. *Bottom:* Angled 3D model of same tile. Sinusoidal lumens are visible, as is the 3D spatial relationship between the two networks.

2.3.3 *Deep, large-field fluorescent labeling and imaging of zonated mesoscale hepatic structures.*

Having found evidence that we could unveil the 3D organization of critical human liver cell types and structures, we hypothesized that extending our imaging fields in all dimensions would allow the capture of at least one entire human lobule. Previous human liver 3D imaging studies used the portal-central axis as a surrogate for the lobule, but we aimed to map labeled cell types and structures more extensively. Our goal was to map mesoscale interlobular structures to examine how the portal triads and pericentral hepatocytes and sinusoids are arranged in 3D space (**Figure 2.3**).

To examine the 3D organization of human bile ducts, samples were stained with CK19, phalloidin, and Hoechst and cleared with Ce3D (**Figure 2.3 A**). CK19 is a keratin that is normally expressed by cholangiocytes. [95] Phalloidin was used to mark cell membranes, and Hoechst was used to label nuclei. We found that 3D immunostaining for CK19 revealed the intra- and interlobular organization of the bile ducts (**Figure 2.3 A**). An *en face* MIP showed the 3D organization of a representative portal triad (**Figure 2.3 A, top left**). Portal venules were identified as lumens with much larger diameter than the bile ductules, a morphologic hallmark of the venules from traditional histology (**Figure 2.3 A, top left**). To further extend our 3D understanding of bile duct organization, we captured multiple Z-stack tiles from the same image and stitched them together, analogous to creating a quilt from squares of fabric (**Figure 2.3 A, top right**). We

observed multiple distinct clusters of bile ducts (**Figure 2.3 A, top right**). Manual annotation of portal venules (red) and hepatic arterioles (white) was performed using Hoechst, phalloidin, and CK19 signals to confirm that these were two separate portal regions. The finding of two different portal triads revealed that we had successfully mapped bile ducts from at least two separate portal-central axes.

To further interrogate the 3D organization of the ductules, we reconstructed them as a segmented, opaque 3D Surface (**Figure 2.3 A, center and bottom**). Careful investigation of the 3D structures through manual rotation and angling revealed the complexity of the many branches (**Figure 2.3 A, center**). By isolating a representative region of interest of a reconstructed bile ductule and viewing it at a perpendicular angle, we observed a tortuous, nearly looping branch that illustrates the necessity for 3D imaging (**Figure 2.3 A, bottom, asterisk**). A convoluted 3D structure like this would be misrepresented in 2D cross-section (**Figure 2.3 A, bottom, dashed line**). The tortuous branch would appear as two separate bile ducts if sectioned at the height of the dashed line; if cut higher up, it may resemble one horizontal duct. 2D quantification of complex structures like this would either over- or undercount the number of ductules while completely missing the dynamic structural intricacies.

We next used our 3D immunostaining and imaging technique to understand the organization of the zonated vascular structures (**Figure 2.3 B**). SMA was used to distinguish blood vessel types by smooth muscle cell morphology. [96] We observed that SMA displays a strong ring of signal when it marks arterioles (**Figure 2.3 B, top**). It appears as a weaker, stellate signal on central venules and showed little to no signal on sinusoids (**Figure 2.3 B, top, asterisk**). The central venule identity of the SMA^{lo} microvessels was confirmed by the absence of bile ductules or hepatic arterioles, which are portal structures. Also, sinusoids function by coalescing into the central

venule to allow the efflux of blood. We were able to identify these anastomoses in the individual z plane images, further confirming the central venule phenotype. CD32b was used to mark Type 2 LSECs (**Figure 2.3 B**). We observed strong CD32b immunoreactivity by the LSECs in the pericentral and midlobular regions, which faded toward the periportal region (**Figure 2.3 B**). CD31 marks vascular endothelial cells, and we found that it appears most robust in hepatic arterioles (**Figure 2.3 B**). The hepatic arteriole identity of CD31+ SMA+ vessels was confirmed by their small diameters and presence within the portal triads.

We reconstructed these vascular structures as 3D models and carefully interrogated their organization (**Figure 2.3 B**). By rotating and angling this representative large-field image, we observed that we could capture the complete size range of vascular structures (capillaries, arterioles, and venules) across a portal-central axis in 3D (**Figure 2.3 B, top left**). An *en face* MIP revealed this axis from a more traditional viewpoint (**Figure 2.3 B, top right**). We then isolated the representative portal triad reconstruction to examine the 3D structures in greater detail (**Figure 2.3 B, bottom**). We observed some CD32b+ LSECs in the portal region and found that the mesh-like sinusoid network intricately weaves with the hepatic arterioles of the portal triad. In the portal regions, nutrient- and oxygen-rich blood enters the liver through the portal venules and hepatic arterioles. The blood empties from these microvessels into the sinusoidal lumens where it mixes. It then percolates through the extensive sinusoid network till the sinusoids coalesce into the central venule on the other side of the axis. 3D visualization of this vital spatial relationship provides insight into how the structure and function of the liver's microvasculature are inextricably linked.

We next sought to investigate the 3D spatial organization of zonation of both hepatocytes and LSECs (**Figure 2.3 C-D**). To do this, we stained human liver with CYP2E1, CD32b, and phalloidin. We found that these large-field images unveiled the multilobular organization of

pericentral hepatocytes, Type 2 LSECs, and cell membranes, respectively (**Figure 2.3 C-D**). We observed the utility of 3D imaging by comparing a single optical section to an *en face* MIP (**Figure 2.3 C**, **left and center**). We found that the representative large field 2D planes captured only small regions of immunoreactivity (**Figure 2.3 C, left**). This is due to the uneven distribution of the zonated structures, which 2D imaging is known to misrepresent. We observed that 3D reconstruction of 3D large-field images revealed the tissue-wide distribution of the pericentral structures across multiple human lobules (**Figure 2.3 C, center**). By carefully rotating this representative reconstruction in 3D space, we found an interesting phalloidin+ CD32b- CYP2E1- set of lumens likely belonging to a large, interlobular portal triad (**Figure 2.3 C, right**). Angled visualization of the 3D model reveals the interior of the lumens (foreground and background, cyan) as well as the surfaces of the surrounding central patches (yellow and magenta) (**Figure 2.3 C, right**). The larger non-immunoreactive lumen in the foreground is likely a non-terminal portal venule and the smaller lumen in the background is likely a non-terminal hepatic arteriole (**Figure 2.3 C, right**).

Now that we had qualitatively observed liver zonation organization in 3D, we desired to quantify the distribution of the pericentral hepatocytes and Type 2 LSECs (**Figure 2.3 D**). To do this, we performed signal intensity analysis within FIJI. Specifically, we used the Interactive 3D Surface Plot plugin on the MIP of the 3D fluorescent images (**Figure 2.3 D**). This plugin plots the signal intensities of pixels within a region of interest as a 3D projection. The height of the plot (the y-axis) represents the intensity of each pixel, and the base plane of the plot corresponds to the pixel's location in the xy plane of the MIP (**Figure 2.3 D, center**). We found that the CYP2E1 (yellow, left) and CD32b (magenta, center) signal intensities follow similar spatial patterns and nearly colocalized (merge, right) across multiple pericentral regions, named for regional mountain

ranges (**Figure 2.3 D, center**). We visualized the zonated spatial dynamics of pericentral hepatocytes and Type 2 LSECs by choosing inclusive regions of interest containing non-immunoreactive (periportal) edges and central venule lumens (**Figure 2.3 D, center**). We observed that signal dropped off completely within the central venule lumens, appearing like the chimney within a surrounding volcano of signal (**Figure 2.3 D, center**). An *en face* MIP of 'Mt. Rainier' allows more detailed view of the changes in signal intensity across the region of interest (**Figure 2.3 D, right**). While CYP2E1 and CD32b both mark pericentral structures and gradually fade toward the portal regions, the signals do not overlap because they mark two distinct cell types (**Figure 2.3 D**).

By extending our imaging in all dimensions, we observed hepatic structures at the lobular and multilobular levels that have not yet been reported in 3D from human samples (**Figure 2.3 E**). Thus, our liver mapping pipeline enables characterization of vital structurally and functionally zonated mesoscale structures across multiple human lobules.

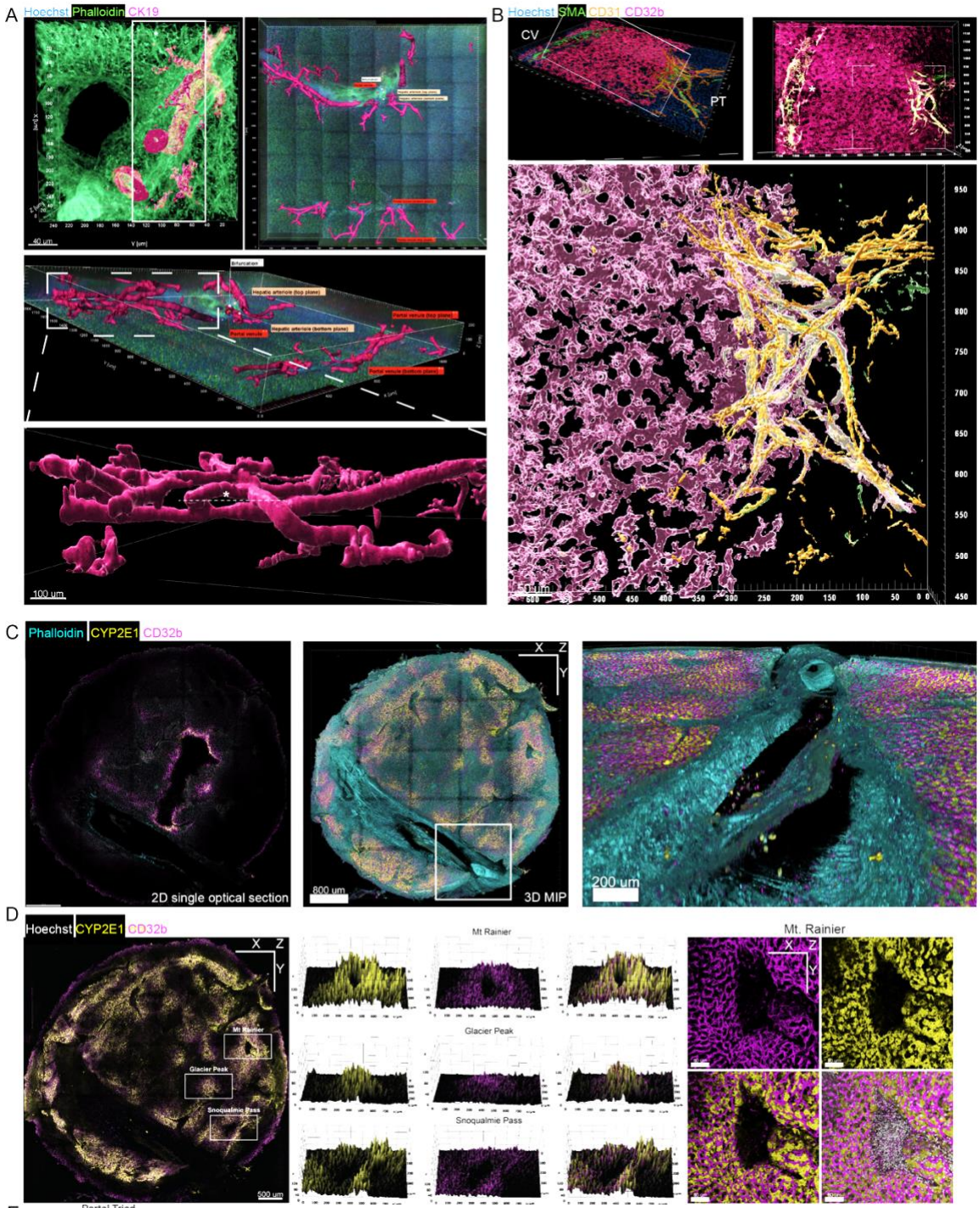
A
Hoechst Phalloidin CK19
100 um
B
Hoechst SMA CD31 CD32b
CV
PT
50 um
C
Phalloidin CYP2E1 CD32b
2D single optical section
800 um
3D MIP
200 um
D
Hoechst CYP2E1 CD32b
Mt Rainier
Glacier Peak
Snoqualmie Pass
500 um
Mt. Rainier
E
Portal Triad
BD
HA
PV
CV
Hepatocytes
Canaliculi
Sinusoids
Human: ~1.5 mm
Mouse: ~ 0.5 mm
Hepatocytes:
Phalloidin+/MRP2+ (membranes)
CYP2E1+ /GLUL+
(pericentral only, cytoplasm)
CK19/CD32b/SMA/CD31-
Canaliculi:
Phalloidin+ (neighboring membranes)
MRP2+
CYP2E1/CK19/CD32b/SMA/CD31-
Sinusoids:
CD32b+ (pericentral and transitional only)
Phalloidin/MRP2/CYP2E1/CK19/SMA/CD31-
Bile ducts:
CK19+/MRP2+ (cholangiocytes)
Phalloidin+ (lumen and cell membranes)
CYP2E1/CD32b/SMA/CD31-
Hepatic arteries:
CD31+++ (endothelial cells)
SMA+/CD32b+ (smooth muscle cells)
Phalloidin/CK19/CYP2E1/MRP2-
Portal veins:
SMA+ (smooth muscle cells)
CYP2E1/Phalloidin/M-
RP2/CD32b/CK19/CD31-
Large and within portal triad
Central veins:
SMA+
CYP2E1/Phalloidin/M-
RP2/CD32b/CK19/CD31-
Large and not within portal triad

Figure 2.3. Deep labeling and 3D imaging of multilobular structures. (A) Immunolabeling of bile ducts. CK19 (magenta) marks the biliary epithelial cells. Phalloidin (green) labels cell membranes. *Top left:* 60 um-thick *en face* MIP of a representative portal triad tile with a 3D reconstruction of the bile ducts (magenta, white box). Unmarked black space is the lumen of a portal venule. *Top right:* Multilobular 100 um-thick *en face* MIP of multiple portal triads with 3D models of the bile ducts (magenta). Manual annotations mark portal venules (red) and hepatic arterioles (white). Phalloidin (green) at this large scale shows the dense cellularity of the tissue. *Center:* Angled view of top right, revealing transverse dynamics of bile ducts throughout tissue volume. *Bottom*: Perpendicular view of inset from the center panel. This view shows the extensive branching of the bile ducts, including tortuous structures (asterisk), exemplifying the importance of 3D volumetric imaging. If this tissue were imaged with traditional 2D histology, the cross-section (dashed line) might make this structure appear to be two distinct bile ducts. **(B)** Immunolabeling of zonated vasculature. CV = central vein, PT = portal triad. SMA (green) was used to distinguish blood vessel types by smooth muscle cell morphology. CD31 (orange) marks vascular endothelial cells, appearing strongest in hepatic arterioles. CD32b labels Type II LSECs. *Top left*: Angled 3D model of representative central-portal axis. *Top right*: *En face* MIP of the box from the top left, showing complex vasculature across the entire central-portal axis with vascular zonation (magenta signal decreases toward portal triad). *Bottom: En face* 3D model of the box from top right, further detailing portal triad architecture. Sinusoids are now transparent to highlight the hepatic arterioles (orange). To detail the sheath-like morphology of arterioles' smooth muscle cells, SMA (green) is transparent. Endothelial cells line the vessel lumens as the tunica intima, while smooth muscle cells surround that layer in a ring called the tunica media. **(C)** Immunolabeling of zonated hepatocytes and vasculature. CYP2E1 (yellow) marks pericentral hepatocytes. *Left:* Single 2D optical section. *Center: En face* 3D MIP of whole biopsy punch. *Right:* Angled fluorescent reconstruction of box in center panel, viewing inside of a vessel lumen. **(D)** Distribution of zonated hepatocytes and vasculature surrounding central venules. *Left: En face* MIP of same image from (C) with isolated central venules labeled "Mt. Rainier", "Glacier Peak", and "Snoqualmie Pass" for their resemblance of regional mountain peaks. *Center:* 3D plots of signal intensity distribution surrounding central venules of interest. Y axis: signal intensity, X and Z axes: positions in 2D space, all measurements derived from MIP. *Right: En face* MIPs of one central venule of

interest. Note the complex interweaving relationship between the pericentral hepatocytes (yellow) and Type II LSECs (magenta). **(E)** Summary of the signal distribution in the human liver.

2.3.4 *Multilobular 3D imaging permits visualization of the first human z-dimensional portal-central axis.*

After developing our liver mapping pipeline to identify structures from the sublobular to the multilobular scales, we hypothesized that we could further expand our imaging capability and explore lobule architecture across an entire biopsy punch. Microscopy of this scale using a 10x objective results in an average rectangular prismatic image greater than 4 mm x 4 mm x 500 um. Our confocal imaging system can capture an image of this size in approximately 15 hours during an overnight imaging session. We notably did not observe significant fluorophore bleaching after imaging of this time length.

We applied an immunostaining panel to mark the structures that create the lobule framework, specifically the central venules and portal triads (**Figure 2.3**). Bile ducts were stained with CK19. Vascular endothelial cells were marked with CD31, which we observed most robustly in the hepatic arterioles, presenting with a strong ring-like signal. SMA was used to mark the smooth muscle cells associated with venules and arterioles. We found a morphological difference between the central venule SMA, which appears quite stellate-like (**Figure 2.3 A, right**), and the strong sheath-like signal of the SMA surrounding the hepatic arterioles (**Figure 2.3, especially panel A, right**). We confirmed central venule identity as these were the only lone structures in this staining panel, whereas portal triad structures appear together. Portal venules were not robustly marked by CD31 or SMA but were identified as the $CD31^{lo}/SMA^{lo}$ lumens present within the portal triads, which we manually traced in Imaris (**Figure 2.3 B-C**).

Our pipeline captured approximately 200x the volume of previous human liver 3D images (**Figure 2.3 A**). Here, we present an angled MIP of a representative fluorescent image encompassing multiple human liver lobules in the x-y plane (**Figure 2.3 A, left**). We found three separate central venules, observing that the one in the center of the image bifurcated into two (double-CV label) (**Figure 2.3 A, left**). We observed representative portal triads semi-regularly interspersed between the central venules, supporting that the human lobule generally repeats throughout the parenchyma. Previously published human liver studies used the portal-central axis (P-C axis) as a surrogate for the liver lobule and presented 3D images of dimensions 500 um x 500 um x 100 um. To compare this to the data volume collected in this study, we placed a representative 500 um x 500 um x 100 um P-C axis from this MIP (**Figure 2.3 A, right**) on the same scale as the entire reconstruction (inset, left).

Our 3D imaging pipeline allowed us to explore human liver architecture at depths previously unattainable by fluorescent imaging. Careful inspection of the images revealed that we had captured the first reported Z-dimensional P-C axis (**Figure 2.3 B-C**). As we panned through the hundreds of Z-plane images that, when stacked, create the 3D image, we observed a central venule in a low z plane, followed by space, and then a portal triad appeared on the top of the z-stack. A perpendicular view of the fluorescent MIP shows the structures (**Figure 2.3 B, left**). By utilizing Imaris's 3D Surface creation module, we segmented the structures of interest to filter out unnecessary signal (**Figure 2.3 B, right**).

By zooming into the 3D image, we visualized the relationship between the branching central venule and portal triad (**Figure 2.3 C).** A perpendicular view of the MIP shows that the central venule on the bottom of the image stack is a lone structure (i.e., not part of a triad) with CD31+ endothelium and stellate-like SMA+ smooth muscle cells (**Figure 2.3 C, left, red box**). The portal

triad found higher in the Z-stack shows strong CK19+ bile ducts with small-diameter CD31+ hepatic arterioles (**Figure 2.3 C, left**). We found approximately 500 um of distance (the average human lobule radius) between the central venule and portal triad. This distance supports the conclusion that we observed a portal-central axis in the Z dimension.

We examined the spatial relationship between the central venule branches and the portal triad by segmenting and reconstructing this region of interest (**Figure 2.3 C, right**). Here, we revealed the consistent distance between the central venule's branches and the branches of the portal triad. As the central venule extends through the parenchyma at an approximately 45º angle, so do the portal triad branches (**Figure 2.3 C, right**). This image is the first published image of a Z-dimensional portal-central axis within the human liver that we are aware of. This finding has possible implications for modeling the liver lobule in 3D space, including schematics and textbook illustrations, where it is frequently imagined as a sphere or a cylinder.

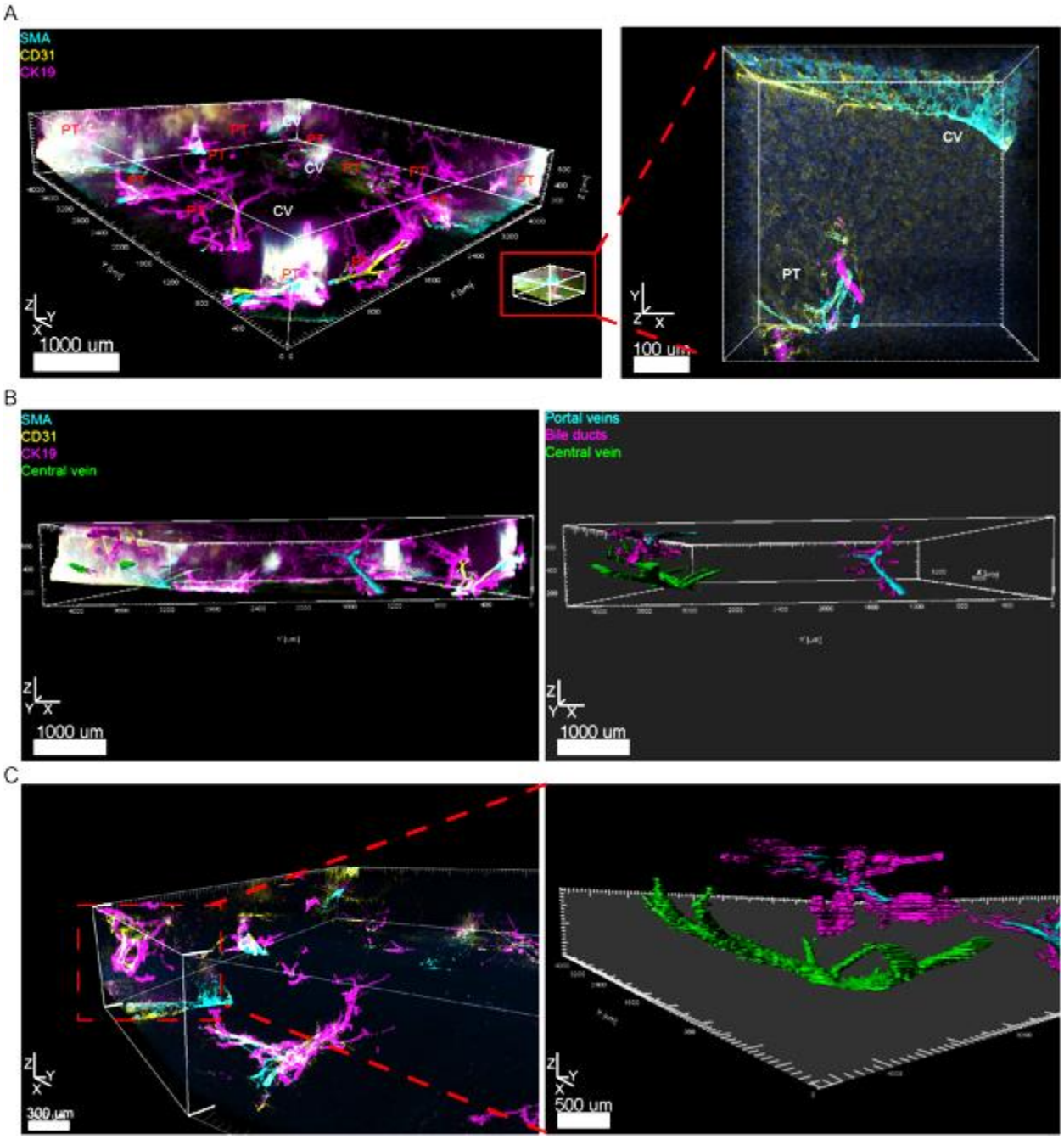

Figure 2.4. Combining thick staining with large-field imaging enables 3D visualization of human liver architecture across multiple lobules. (A) Visualization of 200x the volume of existing 3D human liver studies. *Left:* Angled view of a representative 3D MIP with manual annotation of central veins (CV, white) and portal triads (PT, red). Image dimensions: greater than 4000 um x 4000 um x 800 um, total volume greater than 1.28×10^{10} um^3. Note the strong yellow signal of CD31+ hepatic arterioles (front right edge, bifurcated). Note the dynamic paths of branching bile ductules (magenta) and hepatic arterioles (yellow). *Right:* A representative 100

um-thick *en face* MIP of a P-C axis from left, cropped to 500 um x 500 um x 100 um. These are the reported dimensions within [72], which imaged micro-scale structures across the P-C axis. Right panel is duplicated into the left panel, angled and put onto same scale as left. This illustrates the dramatic volume increase in this work over previous 3D human liver microscopy. Note the stellate-like morphology of venous SMA expression (right). **(B)** Coronal view of same large field from A. *Left:* Manually reconstructed 3D models of bile ductules (magenta), a central venule (green, left), and a portal venule (cyan, right) within merged MIP. *Right:* Isolated 3D models. Note the close association of magenta bile ductules with the cyan portal venule (right). Note the central vein (green, left) captured on the bottom of the Z-stack and portal triad (magenta and cyan, left) captured higher in the Z dimension. **(C)** Exploration of the Z-dimensional P-C axis. *Left:* Angled view of the merged MIP, zoomed in to region of interest. SMA and CD31 mark a central vein branching through the image volume (bottom edge of box). Above, CK19 and CD31 mark a portal triad. Note empty space between the structures. *Right:* Manually reconstructed 3D models of the first-ever published Z-dimensional P-C axis. Note the branching of the central vein (green) through the tissue volume and the consistent distance between the CV and PT.

2.4 DISCUSSION

Here, we have developed a deep immunolabeling, tissue clearing, and confocal imaging pipeline that enables large-field 3D imaging of the human liver. We have surpassed previous 3D liver imaging volumes by approximately 200 times and, in doing so, captured the first images across even one lobule as well as multiple lobules within the same image. We have captured the first Z-dimensional portal-central axis and 3D-modeled the spatial relationship between the central venule and portal triad in the Z dimension. We have demonstrated the necessity and utility of 3D imaging by comparing MIPs and reconstructions against representative 2D cross sections.

Importantly, we have identified a panel of multiple antibodies and small molecules that can be used alone and in combination to mark diverse cell types and structures in the liver. We have used these panels to unveil the 3D interlobular distributions of nuclei, cell membranes, pericentral

hepatocytes, Type II LSECs, bile ductules, hepatic arterioles, and central venules. These markers will likely be useful for deep imaging of other organs. Our optimized Ce3D-based deep immunolabeling and tissue clearing method should also be amenable to other tissue types.

We have extended our imaging field by balancing resolution and capture time and by imaging on our confocal system overnight, without any noticeable signal bleaching. The ability to view the intricate architecture of the liver at a never-before-seen scale unlocks the capacity to begin characterizing the 3D networks of the larger structures like ductules and vasculature that have not yet been explored due to imaging limitations. Further, we expect these protocols to be compatible with diseased liver tissue and enable interrogation of 3D structural changes within advanced liver disease.

Chapter 3. MORPHOMETRIC MULTILOBULAR 3D IMAGING OF THE HUMAN LIVER REVEALS PERIPORTAL EXPANSION AND PERICENTRAL REGRESSION WITHIN THE CIRRHOTIC LIVER

3.1 INTRODUCTION

The liver is the largest internal organ and performs hundreds of distinct functions, from protein synthesis to drug metabolism. The liver is composed of a complex microarchitecture that is integral to both its function and homeostasis. Dramatic microstructural changes are the hallmark of cirrhosis, a progressed form of liver disease where scar tissue deposition segments the parenchyma into sections and causes vascular changes. Cirrhosis has been studied in 2D and is known to involve an expansion of fibrous tissue bands (fibrovascular septa), formation of hepatocyte nodules contained within these septa, dysregulation of zonated hepatocyte functions, and remodeling of bile ductules and blood vessels. The gold standard technique for studying the liver's complex structure and its changes in liver disease is two-dimensional histo(patho)logy.

Traditional histology requires tissue sectioning, which can physically alter the structure. The 2D nature of the visualization can make convoluted structures appear distinct, e.g., a cross-section of one winding vessel may look like two or more separate vessels. To overcome these limitations, we and others have recently begun digitally reconstructing thick tissue samples via 3D immunostaining and tissue clearing. Tissue clearing renders the tissue optically clear to permit deeper imaging and, subsequently, thicker reconstruction than traditional methods. While we know much about how healthy and diseased hepatic cell types and structures are organized in two dimensions, studies are just beginning to explore how they are arranged in three-dimensional space. Most of this work has been performed on rodent liver. The few human liver 3D

immunostaining studies have imaged less than one lobule to a depth of only a couple hundred micrometers. While existing 3D liver imaging studies have begun to unveil the empirical 3D microarchitecture of the human liver in health and in liver disease, they have so far been limited by both the image volume and the number of cell types and structures visualized. We hypothesize that multilobular 3D mapping and morphometric analysis of non-fibrotic and cirrhotic liver unveils volumetric dysregulation of network organization and functional zonation in cirrhosis.

Here, we have surpassed existing 3D human liver mapping attempts by imaging approximately 200 times the previously captured tissue volume. We acquired normal and cirrhotic human liver specimens and applied 3D-optimized immunostaining to label Type 2 sinusoidal endothelial cells, bile canaliculi, biliary epithelial cells, endothelial cells, smooth muscle cells, and pericentral hepatocytes. Liver-optimized optical clearing permitted acquisition of microscope images to a depth of approximately 500 um, a 2.5-to-5-fold depth increase over previous 3D liver studies. Comparative analysis of non-fibrotic and cirrhotic tissues has identified morphological differences in bile ducts, blood vessels, and zonation, features that have not previously been histologically studied in three dimensions. We find a volumetric expansion of periportal structures with regression of pericentral structures and cell types, unveiling a pathological decentralization phenotype within cirrhotic human liver of multiple etiologies. These results provide a more holistic, empirical view of the three-dimensional architecture of the human liver and its cirrhosis-induced adaptive remodeling. These studies may enable more accurate modeling and engineering of 3D human liver tissue and provide new insights into human liver cirrhosis (patho)biology.

3.2 MATERIALS AND METHODS

3.2.1 *Non-fibrotic and cirrhotic human liver samples*

Non-fibrotic samples: Liver samples were obtained after partial hepatectomy from patients undergoing oncologic surgery with no underlying liver fibrosis (**Table 3.1**). The non-tumor liver (n = 6) was dissected from at least two centimeters away from any present tumor, a distance at which the tissue was free from field effect. One sample was obtained from an organ donor who died from causes unrelated to the liver, wherein a biopsy was collected as soon as possible post-mortem.

Cirrhotic samples: Liver samples were obtained either post-partial hepatectomy from patients undergoing oncologic surgery with evidence of underlying fibrosis (n = 2) or after complete liver resection from patients who received liver transplants (n = 3) (**Table 3.1**).

To preserve tissue, samples were sliced with a vibratome to a thickness of two millimeters and fixed immediately in 4% paraformaldehyde for up to one week at 4C and then moved to phosphate-buffered saline at 4C. All participants provided written informed consent. All de-identified human specimens were obtained from a Biorepository. The study protocol was approved by the institutional review board (A Repository for the Study of the Pathogenesis and Treatment of Liver Tumors. University of Washington STUDY00001852) before study commencement.

Table 3.1. Details for analyzed samples.

Group	Sex	Age (yrs)	Reason for Hepatectomy	Chemo?	Notes
Non-fibrotic	F	75	Adenocarcinoma	No	
	F	64	Hepatocellular carcinoma (HCC)		History of Li Freumani syndrome
	F	59	Metastatic colorectal cancer (mCRC)	Yes	Some chemo-associated steatosis
	M	46	mCRC	Yes	
	F	69	mCRC	Yes	Minimum chemo
	M	38	mCRC	Yes, FOLFOX	
	M	49	Brain death (donated organ)	No	

Cirrhotic	F	66	Hepatitis C virus (HCV)-HCC		"Mild fibrosis"
		51	mCRC	Yes, FOLFOX	
	F	68	Cirrhosis (transplant)	No	Decompensated alcoholic cirrhosis
	F	62	Cirrhosis (transplant)	No	Acute hepatitis B virus
	M	51	Cirrhosis (transplant)	No	Primary sclerosing cholangitis
Median	F	60.5	mCRC	Yes	

3.2.2 *Deep immunolabeling of structural (Architecture Panel) and functional (Zonation Panel) zonation and tissue clearing*

For immunostaining and tissue clearing, we used a modified, liver-optimized version of the Ce3D protocol. [61] To begin immunostaining, samples were first punched into six-millimeter discs using biopsy punches, washed in fresh phosphate-buffered saline (PBS) for one hour, and then blocked in Ce3D alternative blocking buffer (1x BD Perm/Wash buffer + 1% bovine serum albumin + 1% normal donkey serum + 0.3% Triton X-100 in PBS) overnight at 37C with gentle shaking. To identify proteins of interest, samples were incubated in primary antibodies diluted 1:100 (except for anti-SMA at 1:500) in Ce3D alternative blocking buffer with 5% dimethyl sulfoxide (DMSO) for 24 hours at 37ºC with gentle shaking (**Table 3.2**). If primary antibodies were conjugated to a fluorophore, samples were protected from light from this step on to prevent bleaching. To remove excess antibody, samples were then washed with Ce3D wash buffer (0.2% Triton X-100 + 0.5% 1-thioglycerol in PBS) for six to eight hours at room temperature with gentle shaking, changing the buffer every two hours. To allow fluorescent visualization of the primary-bound proteins of interest, washed samples were then incubated in fluorophore-conjugated secondary antibodies diluted 1:400 in Ce3D alternative blocking buffer with 5% DMSO overnight at 37ºC with gentle shaking, and protected from light from this step on to prevent bleaching (**Table 3.2**). To remove the unbound excess antibody, samples were next washed in Ce3D wash buffer for six to eight hours at room temperature with gentle shaking, changing the buffer every two hours.

Finally, samples were transferred to Ce3D clearing solution with Hoechst 33342 (1:400 dilution) for overnight incubation at 37ºC with gentle shaking. This overnight incubation allows for water-Ce3D exchange within the tissue, beginning RI matching. To enhance RI matching, tissue is then moved to a larger volume of new Ce3D clearing solution in the morning and held at room temperature for long-term storage.

Table 3.2. Key Resources Table – Multiplexed Antibody Panels

ANTIBODY/SMALL MOLECULE	TARGET	IDENTIFIER
Architecture Panel		
Hoechst 33342	Nuclei	Cat#H3570
Rabbit monoclonal anti-CK19 (clone EP1580Y)	Bile ducts	Cat#ab52625; RRID: AB_2281020
Mouse monoclonal anti-CD31 (clone JC/70A)-DyLight 550	Vascular endothelial cells	Cat#NB600-562R
Mouse monoclonal anti-aSMA (clone 1A4)	Smooth muscle cells	Cat#A2547; RRID: AB_476701
Donkey anti-Rabbit, Alexa Fluor 647	CK19	Cat#A31573; RRID: AB_2536183
Donkey anti-Mouse, Alexa Fluor 488	aSMA	Cat#A21202; RRID: AB_141607
Zonation Panel		
Hoechst 33342	Nuclei	Cat#H3570
Goat polyclonal anti-CD32b	Type II LSECs	Cat#AF1330; RRID: AB_354737
Mouse monoclonal anti-GLUL (clone GS-6)	Pericentral hepatocytes	Cat#MAB302; RRID: AB_2110656
Rabbit monoclonal anti-CK19 (clone EP1580Y)	Bile ducts	Cat#ab52625; RRID: AB_2281020
Donkey anti-Rabbit, Alexa Fluor 488	CK19	Cat#A21206; RRID: AB_2535792
Donkey anti-Goat, Alexa Fluor 647	CD32b	Cat#A21447; RRID: AB_141844
Donkey anti-Mouse, Alexa Fluor 555	GLUL	Cat#A31570; RRID: AB_2536180

3.2.3 *3D imaging and image processing*

To image the biopsy punches, a stained and cleared human liver sample was placed on a glass-bottom dish in enough Ce3D to cover the tissue, covered with a coverslip to keep flat, and imaged on a confocal laser scanning microscope (Leica TCS SP8) with a 10x 0.4 numerical aperture dry objective (Leica). Hoechst, Alexa Fluor 488, Alexa Fluor 555 or DyLight 550, and Alexa Fluor 647 were excited with 405, 488, 552, and 638 laser lines, respectively, and detected with hybrid detectors (HyD).

To image the whole biopsy punches in 3D, arrays of 4 x 4 Z-stacks were acquired and stitched together through Leica Application Suite X (LAS X) software. Imaging of this magnitude requires overnight microscopy sessions of approximately 16 hours. We do not notice significant signal bleaching after imaging for this long. The bottom of the Z stack was set ~5 um below the start of the visible signal to allow for sample settling or movement. The top of the stack was set at the end of the visible signal, with Z-compensation used to increase laser power and gain throughout the stack as necessary. A maximum laser power of 5% was not exceeded to avoid significant fluorescence bleaching. Tile scans were stitched using the Mosaic Merge function within LAS X. One 6 mm biopsy punch was imaged per antibody panel per subject, in general.

Images were visualized and processed in Imaris 3D visualization and analysis software. The Normalize Layers function was used to correct signal attenuation across the image depth in the Z dimension. The Background Subtraction function was used to reduce the background signal. Signal attenuation across the X and Y dimensions was corrected by rotating the image by 90º and applying the Normalize Layers function separately.

3.2.4 *Quantitative morphometric analysis*

To perform morphometric analyses of multilobular structures, we used Imaris software (Oxford Instruments) and Vesselucida software (MBF Biosciences).

For quantification of structure volumes and tissue densities, Surfaces of each immunofluorescent stain were generated in Imaris. Surfaces were made using the Surface Creation Wizard with the Smoothing and Background Subtraction parameters set to 4 µm and 15 µm, respectively. The "split touching objects" option was utilized to enable visualization of individual structure characteristics, e.g., signal intensity within a single reconstructed sinusoid branch rather than the overall connected network. Surfaces parameters including Background Threshold and Quality for seed point filtering were then manually adjusted to optimize accuracy of image reconstruction for each sample. Lastly, we identified and removed any background signal or tissue autofluorescence that was captured in the reconstruction. From these Surfaces, Imaris generated data describing the stained features' volumes and signal intensities.

To trace and quantify the branching structures (bile ductules, microvessels, and central venules), we used Vesselucida. The images had to be resized to 25% of the original image size to load within the tracing software. A semi-manual process was used to trace branching structures. First, the automatic tracing module was used to identify the microstructures of approximately 15 um diameter (bile ductules and microvessels). Then, larger vessels or ductules were manually traced, and these were manually connected to smaller automatically traced vessels. We manually traced the central venules, which were all too large for the automatic tracing to identify reliably. From these tracings, Vesselucida generated morphometric data describing the architecture of the networks at the whole-image level, the individual vessel/ductules level, the segment level, and branch points and loops.

3.2.5 *Statistical analysis*

Data are presented as violin plots with all data points. GraphPad Prism was used to perform all statistical analyses. For comparisons between two groups, a Mann-Whitney U test was performed.

3.3 RESULTS

3.3.1 *Traditional 2D histopathology to phenotype analyzed samples.*

To first phenotype the human samples being explored in 3D, we performed traditional 2D histology. All samples underwent traditional paraffin processing and microtome sectioning. Tissue sections from each human sample were stained with Masson trichrome, which stains connective tissue blue, cytoplasm red or pink, and nuclei brown or black (**Figure 3.1, left**). Each sample's tissue sections were also stained with hematoxylin and eosin (H&E), which stains cytoplasm pink and nuclei purple or blue (**Figure 3.1, right**).

We found an increase in connective tissue within cirrhotic samples by examining the Masson trichrome compared to non-fibrotic (**Figure 3.1, left**). Our non-fibrotic samples contained small amounts of connective tissue in the portal regions, consistent with normal tissue morphology (**Figure 3.1 A**). The cirrhotic samples contained more connective tissue overall, expanding from the portal regions to bridge the tissue as fibrous bands (**Figure 3.1 B**). Cirrhotic tissue contained distinct nodules of hepatocytes isolated from the rest of the tissue by these fibrous bands, consistent with known cirrhotic morphology (**Figure 3.1 B, asterisk**). These nodules and the absence of central venules made it impossible to identify normal portal-central axes or lobule architecture within the cirrhotic Masson trichrome stains.

H&E staining allows pathologists to analyze the cellularity and general architecture of the tissue (**Figure 3.1, right**). H&E staining of the non-fibrotic samples revealed approximately normal morphology with visible portal triads and central venules (**Figure 3.1 A**). Sinusoids are visible as the white space between the cords of the pink hepatocyte cytoplasm. Bile ductules are discernible as distinct rings of epithelium with large nuclei near the larger white portal venule lumens (**Figure 3.1 A, right, asterisk**). We found small numbers of immune cells with tiny, bright nuclei near the portal regions of the non-fibrotic liver (**Figure 3.1 A**). Cirrhotic human samples contained an increased immune cell presence, as expected (**Figure 3.1 B, right, angle bracket**). We found an increase in bile ductules within our cirrhotic samples' H&Es, typically located in the expanded fibrous septa which originate from portal regions (**Figure 3.1 B, right, caret**). Non-nucleated, pink, protein-rich regions are swaths of connective tissue present in cirrhotic tissue but not non-fibrotic (**Figure 3.1 B, right, asterisk**). Our traditional histological staining revealed dramatic structural changes in cirrhotic tissue compared to non-fibrotic and allowed phenotyping of the tissues used in this study. However, 2D staining does not allow us to view or analyze these pathologic changes in their native 3D context. This limitation led us to apply our established 3D imaging procedures to interrogate volumetric structural and functional changes in human cirrhosis.

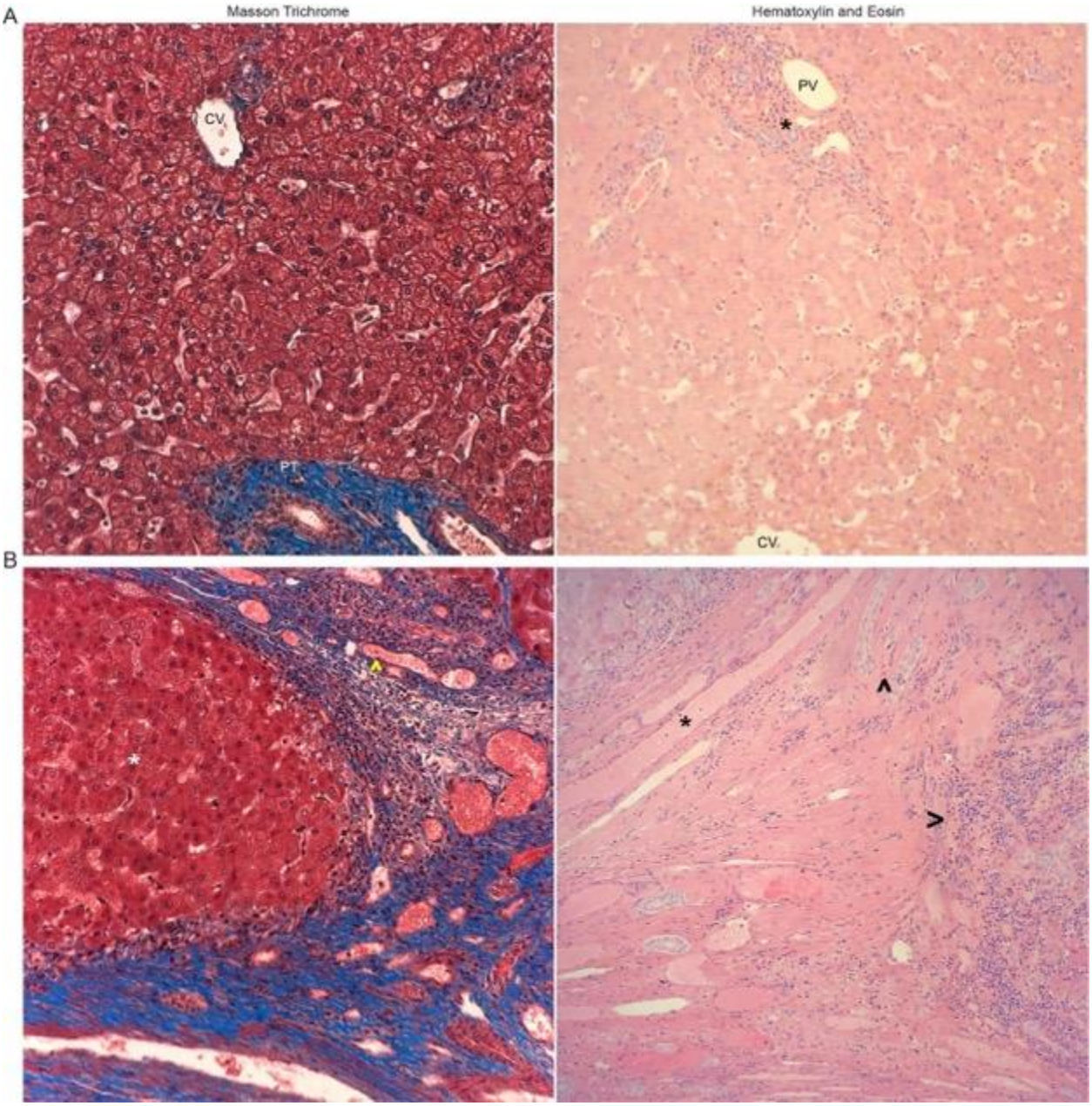

Figure 3.1. Traditional histological staining for phenotyping our analyzed samples. Masson trichrome staining (left) reveals connective tissue in blue and cell cytoplasm in red. Nuclei are brown/black. Hematoxylin and eosin staining (right) colors cytoplasm pink and nuclei purple/blue. (A) Representative field of a representative non-fibrotic human liver tissue sample. CV: central venule. PT: portal triad. PV: portal vein. Asterisk: bile ductule cross-section. (B) Representative field of a representative cirrhotic human sample. White asterisk: hepatocyte nodule. Yellow caret: full blood vessel. Black asterisk: non-nucleated connective tissue. Black caret: expanded bile ductules. Angle bracket: immune cells.

3.3.2 *Development of 3D models of branching structures.*

To enable morphometric analysis, we developed a pipeline within the commercially available software Vesselucida (MBF Biosciences) to trace branching structures and measure those traces at the whole-network, individual vessel/duct, and individual segment levels (**Figure 3.2**). The software uses the term 'vessel' to identify any continuous branching structure; in this section, 'vessel' is synonymous with 'ductule'. We found that resizing our large images to 25% using the Resize function of LAS X software (Leica Microsystems) allowed them to not exceed the software and hardware's computing capacities. We observed that the software's automatic tracing module, which was developed for tracing microvasculature rather than vessels of larger diameters, did not trace large vessels reliably. Instead, it detected the signal on the walls of the lumens as individual microvessels. Therefore, we observed optimal tracing of larger vessels with visible lumens by utilizing the manual tracing module.

The pipeline presented here details the working steps of the vessel tracing process. First, the fluorescent image is visualized as a MIP, which can be viewed as a partial projection which the user can pan through (**Figure 3.2 A**). We found this function helpful for identifying vessel segments through the complex networks, which can be visually overwhelming and confusing to trace as full projections. The fluorescent image is then traced, either manually or automatically (**Figure 3.2 B**). Automatic tracing involves seed point placement along the vessels; seeds are generated by an algorithm and then can be manually edited. Seeds are then connected by an algorithm to form 3D tracings of the vessels, shown here as a center line (yellow) to permit visualization of the trace with the fluorescent signal (**Figure 3.2 B**). 3D vessel traces will generate volume from the center line out the edge of fluorescent signal and can be pseudo-colored for custom visualization (**Figure 3.2 C**). We found that rainbow coloration provided efficient

visualization of individual traced vessels (**Figure 3.2 C**). 3D traces can be used as binary segmentations by isolating the traces from any remaining background signal (**Figure 3.2 D**). We found that we could view the 3D reconstructions on a white background to enhance shadows (**Figure 3.2 E**). Vesselucida software allows the export of these 3D tracings as file formats (.stl, .obj, etc.) compatible with many common 3D printers.

After tracing vessels, structural features like branch points and loops can also be visualized. We observed that Vesselucida could reliably identify branch points within traced vessels (**Figure 3.2 F, red**). We also found reliably traced loops within reconstructed vessels (**Figure 3.2 G, white**). This optimized Vesselucida tracing protocol allowed us to model branching structures in 3D and perform morphometric analyses to compare cirrhotic human liver to non-fibrotic.

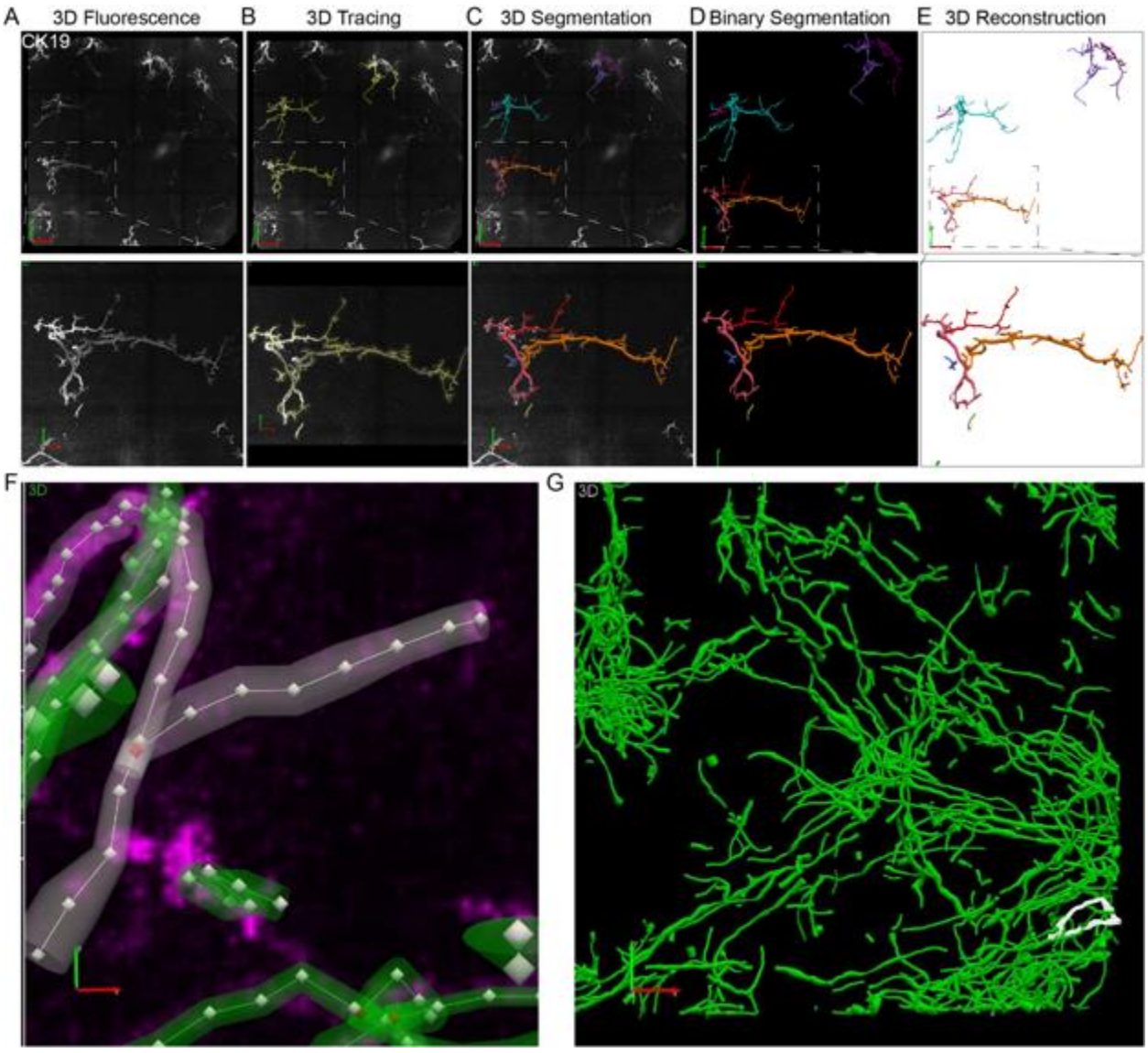

Figure 3.2. Branching structures are reconstructed as 3D models using Vesselucida.

Results of each step of Vesselucida tracing on one representative large human sample. Here, three bile duct clusters from individual portal triads are reconstructed to show context compared to unconstructed signal. **(A)** Fluorescent image (en face MIP) of interest. **(B)** Tracing (yellow center line) is done manually or semi-automatically. Manual tracing involves placing points along the structure, which the software will then reconstruct. Semi-automatic tracing involves placing 'seeds' on structures and optimizing algorithm parameters that the software then uses to connect the seeds. **(C)** 3D tracing with color coding to cycle through rainbow colors for each individual structure. Note remaining background signal (gray). **(D)** 3D tracing may be isolated from background signal to leave a binary reconstruction. **(E)** White background allows visual

appreciation of structure connectivity. **(F)** Vesselucida reconstructs branch points (red) within tracings. **(G)** Vesselucida reconstructs loops (white) within tracings.

3.3.3 *3D surface models of structures and networks.*

To quantify volumetric properties of non-branching structures, we utilized Imaris 3D visualization and analysis software (Oxford Instruments). We found that Imaris generates reliable 3D models (Surfaces) of fluorescently stained structures. First, we visualize the raw fluorescent image within Imaris's 3D View module (**Figure 3.3 A**). We processed our images by applying the Normalize Layers function to correct for signal attenuation in x, y, and z planes (**Figure 3.3 B**). Next, we used the Imaris Surface Creation Wizard to generate opaque 3D models of the fluorescent signal (**Figure 3.3 C**). We found optimal reconstruction using the Wizard in Local Contrast mode rather than Absolute Intensity mode. We optimized parameters for our images (**Figure 3.3 C**). After reconstruction, we trimmed the samples to eliminate areas with unsatisfactory antibody signal to increase quantification accuracy (**Figure 3.3 D**). We found that trimming 3D images resulted in reduced empty, black image space, which would have artificially diluted structure densities. This also allowed us to correct for observed individual sample differences in antibody penetration or tissue clarity, which resulted in some tissue samples containing deeper tissue signal than others. We generated uniform 4000 x 4000 x 300 um rectangular prismatic images for quantification (**Figure 3.3 D**). Finally, volumetric measurements were calculated using Imaris's built-in Statistics operation (**Figure 3.3 E**).

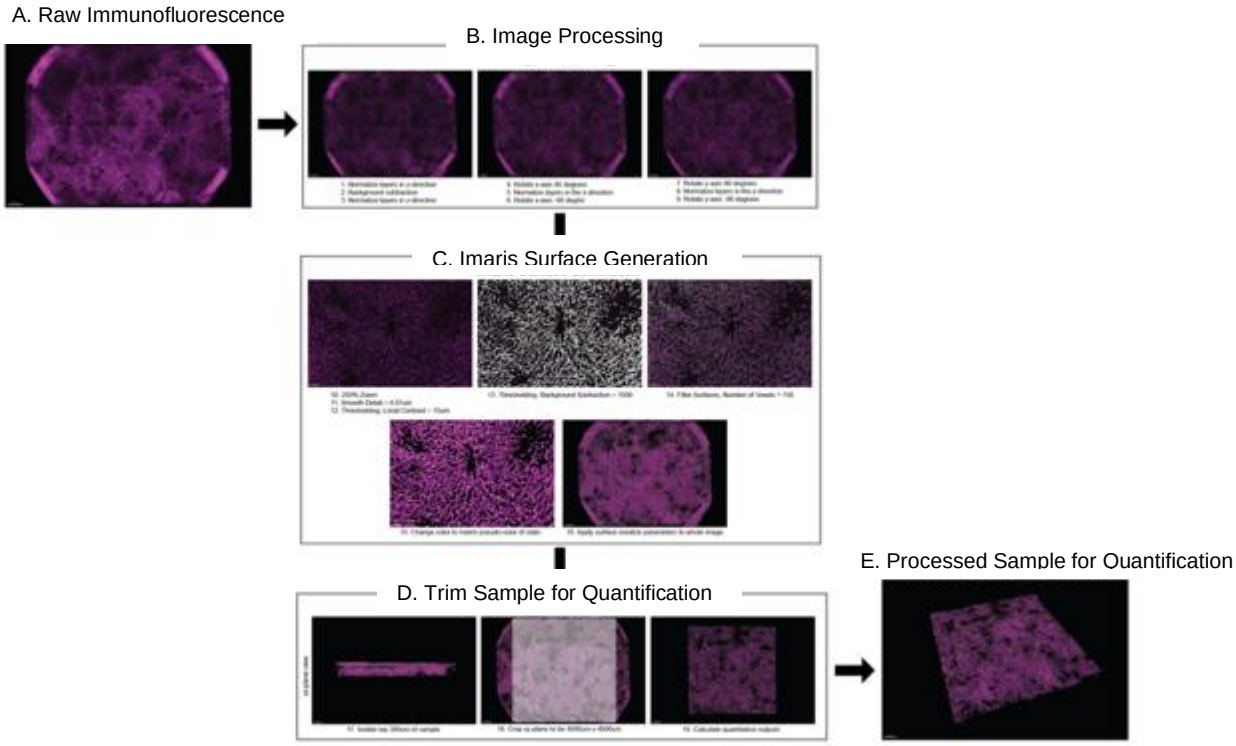

Figure 3.3. Volumetric structures are reconstructed as 3D models using Imaris. Results of each step of Imaris processing and Surface creation on one representative image. **(A)** Fluorescent image (en face MIP) of interest. **(B)** Image processing is performed. 1. Normalize layers in Z-dimension. 2. Background subtraction. 3. Normalized layers in Z-dimension. 4. Rotate X-axis 90º. 5. Normalize layers in X-dimension. 6. Rotate X-axis -90º. 7. Rotate y-axis 90º. 8. Normalize layers in the y-dimension. 9. Rotate y-axis -90º. **(C)** Surface Creation Wizard is used. 10. 250% zoom used to visualize details. 11. Smooth detail = 4 um. 12. Thresholding based on Local Contrast = 15 um. 13. Thresholding based on Background Subtraction = 1500. 14. Filter based on volume, Number of Voxels = 150. 15. Pseudo-color Surface as desired. 16. Apply Surface Creation parameters to entire image. **(D)** Samples are trimmed for quantification. 17. Isolate top 300 um of sample. 18. Crop XY plane to be 4000 um x 4000 um square. 19. Calculate quantitative outputs. **(E)** Output processed Surface image, angled.

3.3.4 *The cirrhotic liver contains a denser and more complex 3D network of CD31+ microvessels than non-fibrotic.*

After developing morphometric analysis workflows and showing that our non-fibrotic and cirrhotic tissues exhibited characteristic differences using traditional 2D histology, we hypothesized that our liver mapping techniques would enable comparative analysis of the cirrhotic microvasculature. To test this hypothesis, we performed thick immunostaining using our optimized architectural staining protocol. This antibody panel marks the bile duct network with CK19, the microvessel network with CD31, and smooth muscle cells with SMA. This allows identifying the portal triads (CK19+ CD31+) and central venules (SMA+CK19-).

We found that in both non-fibrotic and cirrhotic tissues, the CD31 signal provides robust segmentation of hepatic arterioles, which are otherwise identifiable based on their presence within the portal triad and their relatively small diameter compared to the larger portal venules (**Figure 3.4 A**). We found that CD31 may also mark injured sinusoids in some cirrhotic tissues that have undergone defenestration and capillarization (**Figure 3.4 A, right**). [97] Therefore, our CD31+ network analysis reflects changes in the non-fenestrated microvessel populations.

To quantify the observed differences in microvessel networks between non-fibrotic and cirrhotic human liver tissue, we traced CD31+ microvessels across each entire sample using Vesselucida software (**Figure 3.4 B**). Analysis of these tracings within Vesselucida Explorer software showed that the microvessel network of the cirrhotic human liver is significantly denser and more complex than the non-fibrotic network (**Figure 3.4 C**). Specifically, we found a significant increase in the total: number of vessels, vessel network path length, vessel surface area, vessel network volume, percentage of tissue area, number of branching nodes, and number of vessel endings per entire sample in the cirrhotic liver compared to non-fibrotic (**Figure 3.4 C**).

To interrogate the architecture of the individual microvessels that make up the overall network, we quantified properties of the average individual microvessels per sample rather than the whole network (**Figure 3.4 D**). We found no statistically significant differences in the individual microvessel architecture within non-fibrotic and cirrhotic human liver samples (**Figure 3.4 D**). Specifically, we cannot dismiss the hypothesis that any observed differences are due to chance. The measured properties include average length, surface area, volume, number of branching nodes, loop count, and number of endings per vessel (**Figure 3.4 D**).

We further dissected the individual microvessels' architecture by quantifying the characteristics of the individual segments and loops that comprise the individual vessels (**Figure 3.4 E-F**). Loops are segments that branch off and then rejoin the 'trunk' of the vessel. We observed no significant differences between the non-fibrotic and cirrhotic groups; any differences may be due to chance. The measured segment properties were average length, average diameter, and average tortuosity. The measure loop properties included average length, surface area, volume, and diameter.

Taken together, these data indicate that though the architecture of the individual CD31+ microvessels is not significantly different from the non-fibrotic liver, the cirrhotic liver contains significantly more individual microvessels resulting in a denser and more complex network. This significant increase in the number of microvessels leads to a network-wide increase in density (percent of tissue volume comprised by vessels), total path length, surface area, volume, branching nodes, and endings. Importantly, without 3D imaging and analysis, we would not be able to measure volumetric vessel parameters like density and volume. We would not be able to reliably identify microvessel branches and loops, which would each appear as one or two distinct structures in cross-section. By imaging 3D across multiple lobules, we have captured and analyzed the

microvessels as a network. Our evidence that the 3D architecture of the average individual microvessels does not significantly differ emphasizes the importance of our technique's ability to analyze architecture across large data volumes, enabling network-wide quantification.

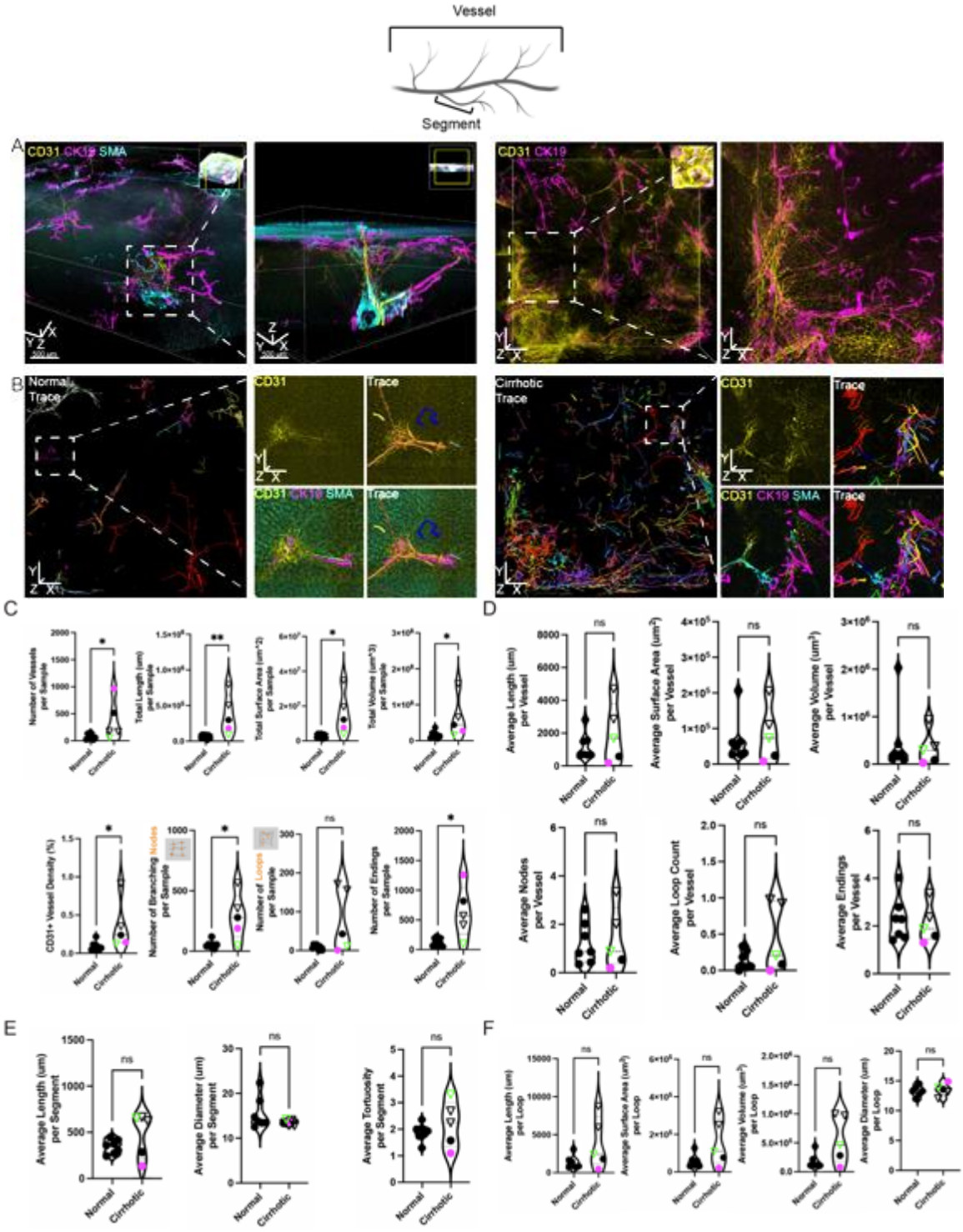

Figure 3.4. 3D imaging unveils an increase in CD31+ microvessel network density and complexity in cirrhosis. (A) 3D fluorescent images showing CD31+ microvessel (yellow) morphology in non-fibrotic (left) and cirrhotic (right) tissue. **(B)** Left: Representative en face 3D tracing of CD31 across an entire non-fibrotic human liver biopsy punch. Individual vessels are

color-coded rainbow. Inset shows fluorescent MIPs overlaid with tracing. Right: Representative en face 3D tracing and MIPs of a representative cirrhotic biopsy punch. **(C)** Morphometric measurements of each sample's entire CD31+ microvessel network. **(D)** Morphometric measurements describing the average individual CD31+ microvessel within each sample. **(E)** Morphometric measurements describing the average segment per CD31+ microvessel for each sample. **(F)** Morphometric measurements describing the average CD31+ loop per sample. Data points: Open triangles are samples of decompensated cirrhosis. Lime green sample was green to the eye, indicating bile congestion. Magenta sample was denoted fibrotic rather than cirrhotic.

3.3.5 *The cirrhotic 3D biliary network fills more tissue volume than the non-fibrotic biliary network.*

Having used morphometric analysis to detect differences in the cirrhotic and non-fibrotic CD31+ microvessel networks, we next sought to compare the critical bile ductule networks.

We found that in both non-fibrotic and cirrhotic tissues, CK19 signal robustly marks the cholangiocytes that comprise the bile ductules (**Figure 3.5 A**). We closely examined the cirrhotic samples for any morphologies that may resemble classic ductular reaction (DR), and we did find hallmark DR in one sample. However, most samples did not display classic DR, instead presenting with some intermediate expanded morphology (**Figure 3.5 A, right**). Therefore, our CK19+ network analysis reflects changes in the bile ductule networks including, but not limited to, classic ductular reaction.

To quantify the observed differences in ductule networks between non-fibrotic and cirrhotic human liver tissue, we traced CK19+ ductules across each entire sample using Vesselucida software (**Figure 3.5 B**). Analysis of these tracings within Vesselucida Explorer software showed that the ductule network of the cirrhotic human liver has a longer total path length and takes up a significantly larger percentage of tissue volume (**Figure 3.5 C**). Specifically, we found a

significant increase in the total: volume density (%), length, surface area, and number of vessel endings per entire sample in the cirrhotic liver compared to non-fibrotic (**Figure 3.5 C**).

To interrogate the architecture of the individual ductules that make up the overall network, we quantified properties of the average individual ductules per sample in addition to the whole network (**Figure 3.5 D**). We found no statistically significant differences in the individual ductule architecture within non-fibrotic and cirrhotic human liver samples; any observed differences could be due to chance (**Figure 3.5 D**). The measured properties include average length, surface area, volume, number of branching nodes, loop count, and number of endings per ductule (**Figure 3.5 D**).

We further dissected the individual ductules' architecture by quantifying the characteristics of the individual segments and loops that comprise the individual ductules (**Figure 3.5 E-F**). We observed no significant differences between the non-fibrotic and cirrhotic groups; any differences may be due to chance. The measured segment properties were average length, average diameter, and average tortuosity. The measure loop properties included average length, surface area, volume, and diameter.

Taken together, these data indicate that though the architecture of the individual CK19+ ductules is not significantly different from the non-fibrotic liver, the cirrhotic liver contains significantly more bile ductule density and the ductule network has a longer overall path length. Importantly, without 3D imaging and analysis, we would not be able to measure volumetric vessel parameters like density and volume. We would not be able to reliably measure the total path length because 2D cross sections would only show measurable length for perfectly horizontal structures. By imaging 3D across multiple lobules, we have captured and analyzed the ductules as a network. Our evidence that the 3D architecture of the average individual ductules does not significantly

differ, in combination with our similar microvessel data, further emphasizes the importance of capturing large tissue volumes for quantification.

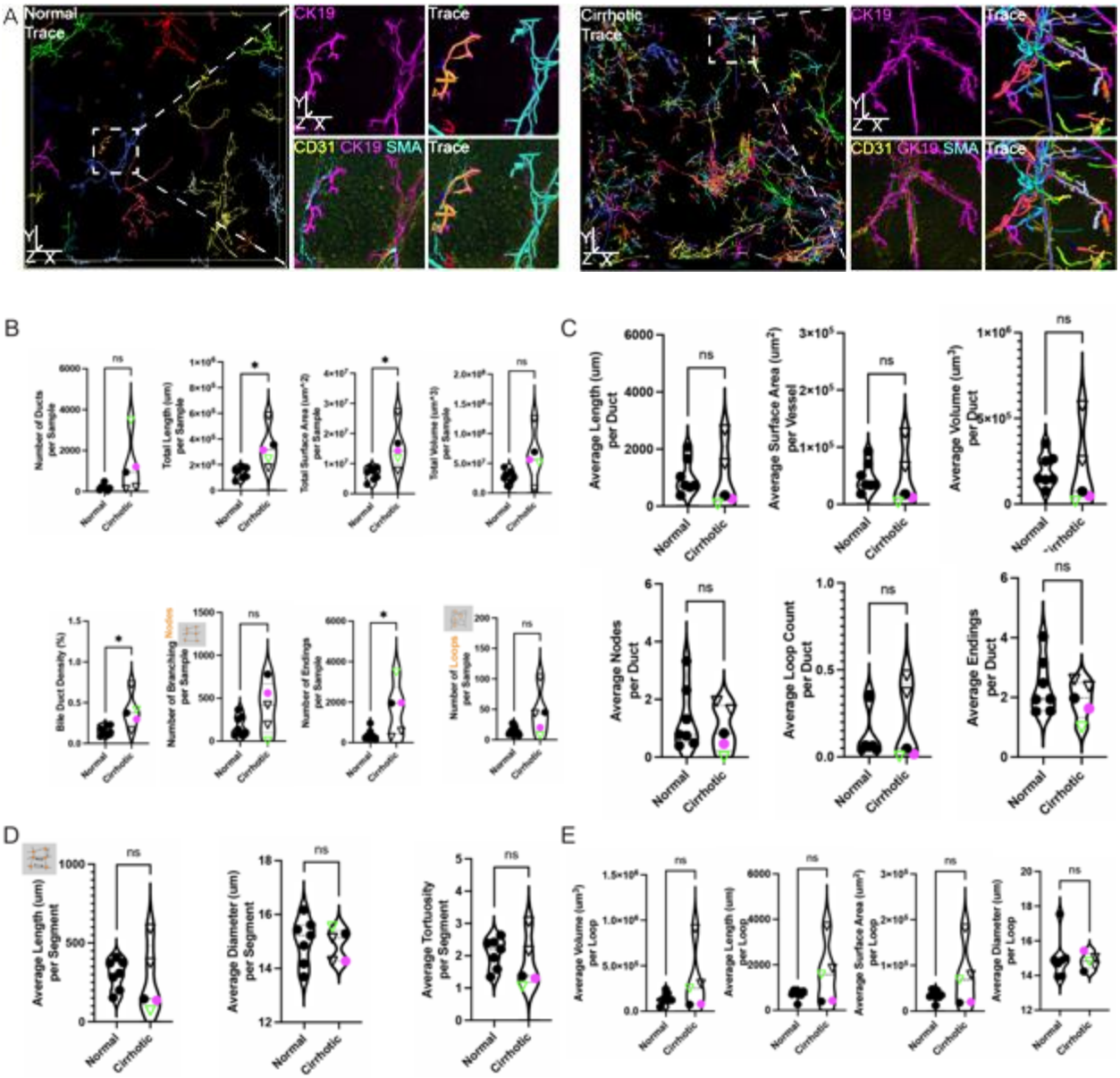

Figure 3.5. 3D imaging unveils an expansion of CK19+ ductule network volume in cirrhosis. (A) Left: Representative en face 3D tracing of CK19 across an entire non-fibrotic human liver biopsy punch. Individual ductules are color-coded rainbow. Inset shows fluorescent MIPs overlaid with tracing. Right: Representative en face 3D tracing and MIPs of a representative cirrhotic biopsy punch. **(B)** Morphometric measurements of each sample's entire CK19+ ductule network. **(C)** Morphometric measurements describing the average individual CK19+ ductule within each sample. **(D)** Morphometric measurements describing the average

segment per CK19+ ductule for each sample. **(E)** Morphometric measurements describing the average CK19+ loop per sample. Data points: Open triangles are samples of decompensated cirrhosis. Lime green sample was green to the eye, indicating bile congestion. Magenta sample was denoted fibrotic rather than cirrhotic.

3.3.6 *The cirrhotic liver contains fewer individual central venules compared to non-fibrotic.*

After performing morphometric analysis to compare cirrhotic and non-fibrotic portal vasculobiliary structures, we next aimed to volumetrically analyze the central venules (CVs). We found that in both non-fibrotic and cirrhotic tissues, SMA marks central venules with its stellate-like morphology (**Figure 3.6 A**). We confirmed central venule identity of these SMA+ vessels by their distance from any surrounding CK19+ bile ducts, which are portal landmarks.

To quantify observed differences in central venules between non-fibrotic and cirrhotic human liver tissue, we manually traced SMA+ CVs across each entire sample using Vesselucida software (**Figure 3.6 A**). Analysis of these tracings within Vesselucida Explorer software showed that the cirrhotic human liver contains significantly fewer central venules than non-fibrotic (**Figure 3.6 B**). Specifically, we found a significant decrease in both the total number of individual CVs and the total number of CV endings in cirrhotic liver compared to non-fibrotic (**Figure 3.6 B**).

To investigate the architecture of the individual CVs within the samples, we quantified properties of the average individual venules per sample (**Figure 3.6 C**). We found no statistically significant differences in the individual venule architecture within non-fibrotic and cirrhotic human liver samples; any observed differences could be due to chance (**Figure 3.6 C**). The measured properties include average length, surface area, volume, number of branching nodes, loop count, and number of endings per ductule (**Figure 3.6 C**). One cirrhotic sample had zero

detectable CVs, which likely made our sample size have less power to detect significance in these comparisons (**Figure 3.6 B-C**).

Taken together, these data indicate that though the architecture of the individual CVs is not significantly different from the non-fibrotic liver, the cirrhotic liver contains significantly fewer individual CVs. Central vein count itself is a measurement that could be done in 2D, but our data volume offers a drastically larger sample from which to draw conclusions than traditional staining; these images are the equivalent of at least 100 individual 2D image planes of greater than 4 mm x 4 mm. Additionally, our evidence that the 3D architecture of the average individual CVs does not significantly differ, in combination with our similar microvessel and ductule data, further demonstrates the importance of capturing large tissue volumes for quantification.

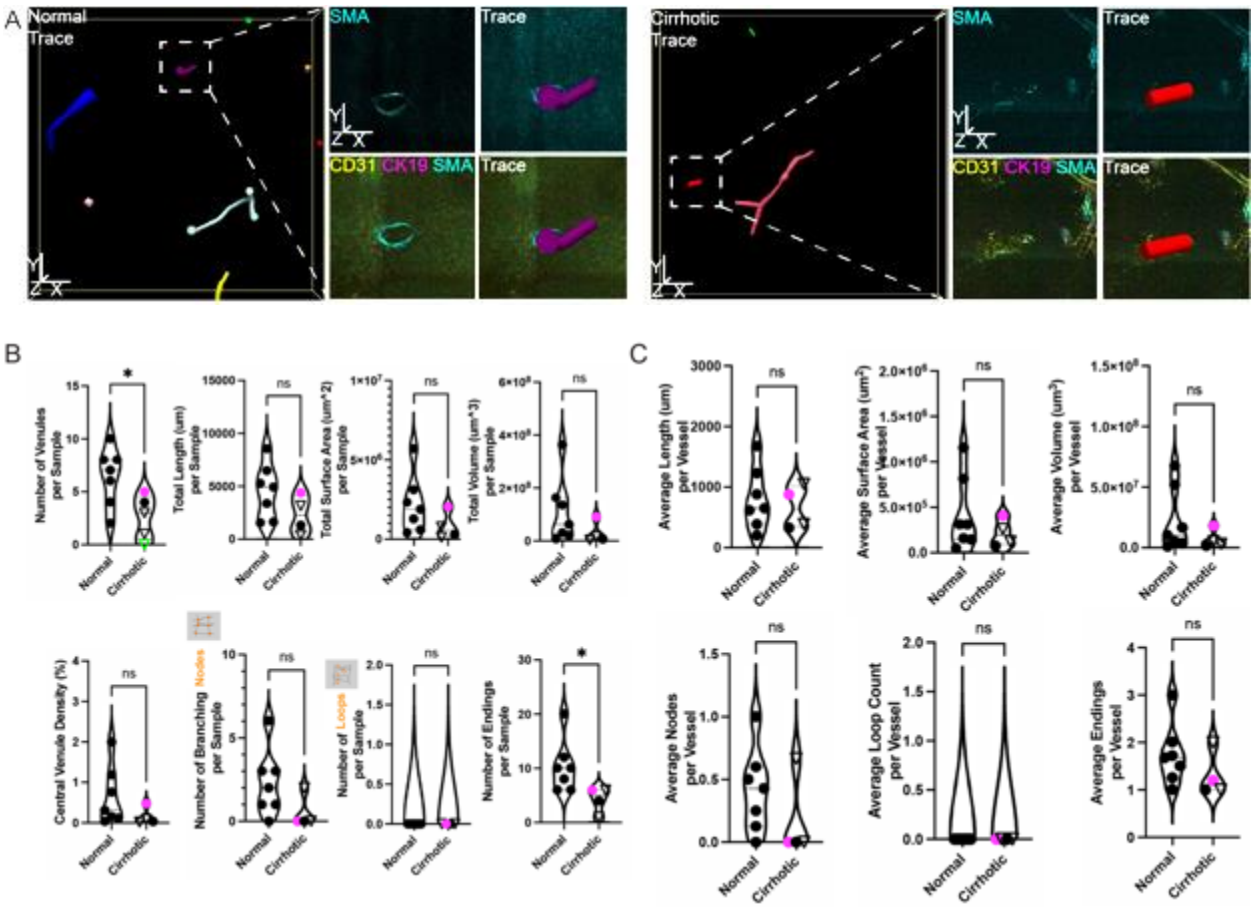

Figure 3.6. 3D imaging shows fewer central venules present in cirrhotic liver. (A) Left: Representative en face 3D tracing of central venules across an entire non-fibrotic human liver biopsy punch. Individual vessels are color-coded rainbow. Inset shows fluorescent MIPs overlaid with tracing. Right: Representative en face 3D tracing and MIPs of a representative cirrhotic biopsy punch. **(B)** Morphometric measurements of each sample's entire central venule network. **(C)** Morphometric measurements describing the average individual central venules within each sample. Data points: Open triangles are samples of decompensated cirrhosis. Lime green sample was green to the eye, indicating bile congestion. Magenta sample was denoted fibrotic rather than cirrhotic.

3.3.7 *Dysregulation of hepatocyte zonation of the cirrhotic liver.*

After revealing dysregulation in structural zonation of the cirrhotic liver lobule through Vesselucida tracing, we sought to investigate the functional zonation of hepatocytes and LSECs in 3D. To do this, we stained, imaged, and reconstructed GLUL+ pericentral hepatocytes and

CD32b+ Type 2 LSECs as 3D models and quantified their volume densities as percentage of overall tissue volume (**Figure 3.7**). We included CK19 staining here as a landmark for the portal region (bile ductules) (**Figure 3.7**).

We did not detect significant differences in the volume densities of sinusoids or nuclei in cirrhotic liver compared to non-fibrotic; observed differences could be due to chance (**Figure 3.7**). We did, however, find a significant increase in the percentage of cirrhotic tissue that was made of CK19+ bile ductules, confirming the previous data measured in Vesselucida (**Figure 3.7**).

Interestingly, we did not find a significant difference in GLUL+ hepatocyte volume density in cirrhotic compared to non-fibrotic liver (**Figure 3.7 C**). However, examining the qualitative and quantitative data further revealed that one sample in the cirrhotic group was a statistical outlier for GLUL+ density. This sample indeed showed robust GLUL+ hepatocytes. We consulted the surgeon who collected the sample and learned that this sample was graded as fibrotic rather than cirrhotic and was therefore less far along the spectrum of fibrosis progression than other cirrhotic samples. We found that every other cirrhotic sample showed nearly no robust GLUL+ hepatocytes. Removal of the statistical outlier does reveal a statistically significant reduction in GLUL+ hepatocyte volume in cirrhotic tissue compared to non-fibrotic. This qualitative and quantitative data further supports our discovery of a net decentralization phenotype within human liver cirrhosis (**Figure 3.7**).

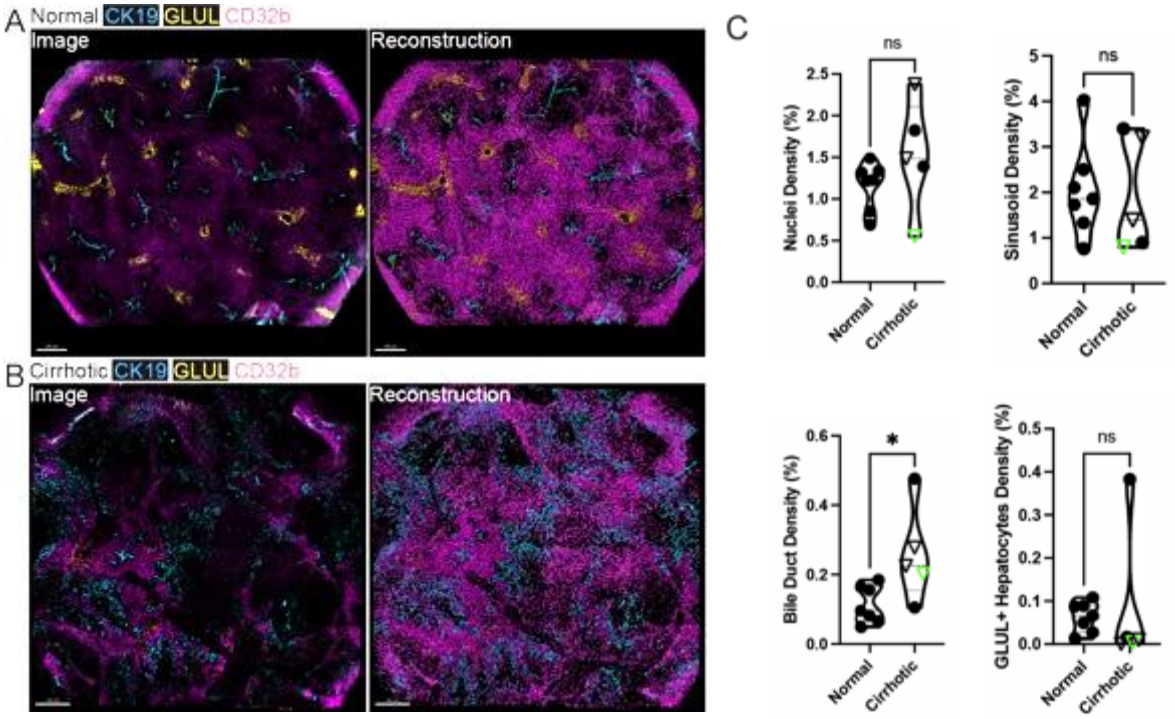

Figure 3.7. 3D imaging of human liver zonation reveals a decentralization phenotype in cirrhotic liver. (A) En face MIP (left) and 3D Surface reconstruction (right) of an entire representative non-fibrotic human liver biopsy punch. **(B)** En face MIP (left) and 3D Surface reconstruction (right) of an entire representative cirrhotic biopsy punch. **(C)** Density measurements of nuclei, CD32b+ sinusoids, CK19+ ductules, and GLUL+ pericentral hepatocytes as a percentage of image volume for each sample. Data points: Lime green sample was green to the eye, indicating bile congestion.

3.4 DISCUSSION

In this chapter, we demonstrate that 3D histology and morphometry can unveil volumetric changes in cirrhotic liver tissue that have potential functional consequences. A key advantage of this method is that it multiplexes commercially available antibodies to mark structural and functional cell types of interest. We developed one panel to mark the landmark portal and central vasculobiliary structures to reveal the architecture of the lobules. We developed another panel to stain the pericentral hepatocytes, Type II LSECs, and bile ducts to interrogate the 3D spatial organization of functional zonation. Our deep immunostaining, clearing, and large-field imaging

pipeline enables investigation of structurally and functionally zonated human liver features at scales and depths not previously possible. This allowed us to investigate how critical 3D networks and pericentral hepatocyte phenotype change in human liver cirrhosis over multiple lobules.

Here, we used 3D imaging and analysis to reveal the volumetric histopathology of the cirrhotic human liver. We tested the hypothesis that the 3D architecture of the vascular and biliary networks is dysregulated in human cirrhosis. We found that the cirrhotic CD31+ microvessel network displays significantly increased density and complexity than the non-fibrotic network. We found sparse regions of a cirrhotic sample displaying CD31+ sinusoids within this dataset, a severely dysfunctional endothelial phenotype correlated with loss of sinusoid fenestrations. Less than one-quarter of the sample displayed this phenotype, indicating the importance of large 3D imaging to capture these minority structural events. We similarly found that the cirrhotic bile ductule network comprises a significantly larger percentage of tissue volume than the non-fibrotic network. This dataset includes one cirrhotic sample containing hallmark ductular reaction. We speculate that there is a non-DR ductular expansion mechanism in cirrhosis. This is concluded from our observation that most samples did not include classic DR but did have significantly increased ductule network density. **These observed expansions in vasculobiliary volume represent an increase in tissue percentage comprised of porto-lobular structures**, potentially reflecting a broader "pro-portalization" phenotype.

We next qualitatively and quantitatively explored the centrilobular structures, namely the central venules, Type 2 sinusoids, and glutamine synthetase-positive hepatocytes. Central venules were defined as having a lumen and stellate-like SMA positivity and importantly did not have nearby CK19+ bile ductules. **We identified significantly fewer central venules within the**

cirrhotic samples than the non-fibrotic, indicating a possible decentralization phenotype. To explore this further, we examined pericentral hepatocytes.

Glutamine synthetase (GLUL), an enzyme involved in nitrogen metabolism, is a classic marker for pericentral hepatocytes. Here, we examined the density of GLUL+ hepatocytes in the non-fibrotic and cirrhotic human liver. All but one cirrhotic sample contained nearly zero GLUL+ hepatocytes, and the one sample that did was clinically "more fibrotic than cirrhotic". If we excluded this statistical outlier, we found a **significant decrease in the density of GLUL+ hepatocytes in the cirrhotic liver compared to non-fibrotic, which is evidence supportive of a decentralization phenotype**. Loss of central hepatic function could have severe functional implications for blood flow; the disappearance of central venules would be associated with dysfunctional blood drainage and possibly contributes to the portal vein hypertension known to be a clinical complication of cirrhosis. Loss of central hepatocyte functions would lead to defects in drug metabolism, nutrient metabolism, and bile acid synthesis. Implications of loss of glutamine synthetase include defects in ammonia metabolism, which can lead to hyperammonemia (buildup of ammonia in the blood). [98] Indeed, hyperammonemia is a side effect of liver failure and cirrhosis and can cause systemic problems including neurological defects. [98, 99]

Here, we have demonstrated the utility of 3D histopathology for the study of liver diseases. We have shown evidence of network-level expansion of portal vasculobiliary structures. Importantly, we have shown that the architecture of the individual ductules and vessels does not significantly change, but the architecture of the overall networks do. In tandem with an expansion of portal structures, we have detected significant regression of central features in cirrhotic liver. Specifically, not only is the number of central venules decreased but so are the GLUL+ pericentral hepatocytes. Taken together, these structural and functional changes reflect a net 'decentralization'

phenotype, where cirrhotic tissue is overall more periportal and less pericentral than non-fibrotic. This dysregulation is reflect in the complete loss of identifiable lobule architecture in traditional Masson trichrome and H&E stains of cirrhotic liver. Importantly, we have explored volumetric features within cirrhotic samples of multiple etiologies, so our results are not specific to only one underlying liver disease but instead represent the cirrhotic tissue state.

Chapter 4. CONCLUSIONS AND FUTURE DIRECTIONS

Three-dimensional imaging could further our understanding of liver (patho)biology by improving the accuracy of models and unveiling the organization of structures within networks critical for function. While imaging modalities currently exist to examine large, perfusable structures in 3D, they do not provide information about the cell types that make up the structures. Immunostaining is traditionally used to examine tissue at the cell level and provides cell phenotype information but is usually done in two dimensions across very small scales. These small scales can isolate the examined structures from the context of the rest of the tissue. Additionally, the 2D nature of traditional histology may misrepresent unevenly distributed, sparse, and convoluted structures. Thus, robust methods to perform 3D histology are necessary.

Recent chemical, microscopy, and technological breakthroughs have enabled a combination of whole-mount immunostaining with deeper imaging of the Z dimension. These innovations have provided 3D images of the liver at cell resolution, unveiling volumetric structural changes underlying experimental rodent pathologies and human fatty liver disease. [72, 78] However, human liver microarchitecture has barely begun to be investigated in 3D, and the existing studies have imaged relatively small tissue sections of 500 um x 500 um x 100 um. While this allowed interrogation of the microscale structures, the complete human lobule and the vital mesoscale structure networks have not yet been imaged in 3D. Further, liver cirrhosis, the severe scar-tissue buildup responsible for most liver disease-related deaths characterized by significant histological defects, has not yet been examined in 3D. This dissertation seeks to address these gaps in methods and knowledge by exploring how structurally and functionally zonated 3D features are organized in the non-fibrotic liver and are dysregulated in the cirrhotic human liver.

To address the challenge of imaging complex, highly cellular tissue in 3D, we must first understand the functional structures of the human liver in health and disease. In Chapter 1, we review the microanatomy of the normal liver with a focus on the main structural unit, the lobule. We discuss the critical lobular structure-function relationship of 'liver zonation,' the phenomenon where individuals of the same cell type perform different functions depending on their proximity to the central venules or portal triad. We next examine what causes liver cirrhosis and how the organization of the lobule and zonation are dysregulated in cirrhosis. Following this introduction to liver (patho)biology, we present the rationale of tissue clearing and the existing 3D immunostaining studies of the rodent and human livers. We correlate the number of rodent and human studies with the smaller relative size of the rodent lobule and highlight the need for technical innovations to analyze larger human samples. Later, in Chapters 2 and 3, we adapt one of these antibody-compatible clearing methods to robustly immunostain and clear human liver tissue. We developed a 3D staining, clearing, and imaging pipeline to visualize the human liver. We then optimized a panel of antibodies and small molecules to label multiple liver cell types and structures and expanded our imaging field to capture various human liver lobules in 3D. In the rest of this dissertation, we used these methods to study structurally and functionally zonated human liver features and quantify how they are dysregulated in cirrhosis.

Chapter 2 reports our staining, clearing, and imaging pipeline to visualize critical multiscale features in the human liver. While previous studies have focused on two or three human liver structures, we identified a panel of antibodies and small molecules with which to stain nuclei, cell membranes, pericentral hepatocytes, bile canaliculi, Type 2 LSECs, vascular endothelium, smooth muscle cells, and bile ducts deeply and in 3D. We found that we could capture architectural structures and functional zonation across multiple portal-central axes. We then expanded our

imaging field to capture architectural structures across the entire biopsy punch of human tissue. Careful examination of this unveiled the first published portal-central axis in the Z dimension, with implications for modeling the third dimension of the liver lobule. The revelation of the intricate 3D organization of these critical liver structures led us to explore volumetric architectural dysregulation in human liver cirrhosis.

The studies in Chapter 3 compare the architecture of branching and non-branching volumetric structures and networks in non-fibrotic and cirrhotic human liver tissue. First, we examined the vasculobiliary systems that comprise the lobule framework. We performed morphometric analyses and compared the structures at the individual vessel/ductule and whole-network levels. We did not find significant differences in the architecture of individual CD31+ microvessels in cirrhotic tissue compared to non-fibrotic. However, we did find statistically significant differences in most measurements at the whole-network level that indicated that the cirrhotic CD31+ microvessel network is significantly denser and more complex than the non-fibrotic. If the networks were forests, the individual trees (vessels) of each forest are not significantly different shapes on average, but the cirrhotic 'forest' contains significantly more trees, so there are many more branches, more total volume, etc. This increase in microvessel network density and complexity has potential implications for blood flow and oxygen and nutrient needs within the cirrhotic liver.

We next compared the individual CK19+ bile ductules and the whole network of ductules between cirrhotic and non-fibrotic liver. We did not find significant differences in the architecture of the individual ductules. We did, however, find a statistically significant increase in the percent of cirrhotic tissue volume made of bile ductules compared to non-fibrotic. We found evidence of Ductular Reaction within few cirrhotic liver samples, suggesting that DR is not the only mechanism of ductule change in cirrhosis. We next performed morphometric analyses on the

central venules, having found significant expansion of these critical portal triad structures. We did not find significant differences in the architecture of the individual central venules. Still, we found a significant decrease in central venules within the cirrhotic liver compared to non-fibrotic. Taken together, these data point to a net 'decentralization' phenotype within the cirrhotic human liver, where the portal structures expand through the fibrous bands and take up more tissue volume while central venules are reduced. This phenotype may have implications for bile and blood flow defects within the cirrhotic liver and functional consequences due to the loss of the lobule architecture altogether. Importantly, our samples were collected from liver cirrhosis of multiple etiologies, implying that the observed changes are not due to specific underlying liver disease but instead represent the cirrhotic tissue state.

After revealing this dysregulation in structural zonation of the cirrhotic liver lobule, we sought to investigate the functional zonation of hepatocytes and LSECs. To do this, we reconstructed GLUL+ hepatocytes and CD32b+ Type 2 LSECs as 3D models and quantified their volume densities as a percentage of overall tissue volume. We included CK19 staining here as a marker for the portal region (bile ductules). We did not find significant differences in the volume densities of sinusoids or nuclei in the cirrhotic liver compared to non-fibrotic. We saw a significant increase in the percentage of cirrhotic tissue made of CK19+ bile ductules, confirming the previous data measured in separate software. We detected a significant decrease in GLUL+ hepatocyte volume between cirrhotic and non-fibrotic liver tissue. This data provides functional protein evidence of a loss of pericentral phenotype within human liver cirrhosis. To summarize these morphometric findings, the microvessel and bile ductule networks are significantly expanded in human liver cirrhosis while central venule count is reduced, and hepatocytes lose their pericentral phenotype. These results led us to conclude that human liver cirrhosis of multiple etiologies displays a net

'decentralization' phenotype, with possible implications for the blood pressure buildup (portal vein hypertension) and hyperammonemia (ammonia buildup) frequently associated with liver failure and cirrhosis.

The methods and findings contained in this dissertation are unique contributions to the growing understanding of 3D liver (patho)biology. Biological organization is critical for function across the molecular, cellular, tissue, and organ spatial scales. Here, we have used traditional techniques in modern and innovative ways to bridge the gap between the cellular and tissue spatial scales in 3D. We have developed antibody panels that will also be useful for examining other epithelial organs. Our liver-optimized deep immunostaining, Ce3D clearing, and large-field microscopy pipeline has overcome existing technical limitations precluding large-volume imaging of tissues with high cell density like the liver. Another cell-dense organ is the kidney, and we expected these methods to inform efforts for imaging large kidney samples. Studying human liver diseases in this 3D has uncovered volumetric aspects of fatty liver disease and, now, liver cirrhosis. We have unveiled that the microvessels and bile ductules change in cirrhosis at the network level, but the individual structures' architectures are not significantly different. This discovery reinforces the need for large-field 3D imaging to interrogate mesoscale biological systems.

Further work in this field should deepen and broaden the scope of the methods and evidence presented here. For example, 3D histology could be used to improve the diagnosis and staging of liver cancer. Groups have found that 3D histology provides pathologists with a more accurate, holistic view for staging prostate cancer, for example, than grading via the individual 2D images. This kind of comparison has not yet been done on human liver tumors that we are aware of, and 3D pathology may improve the accuracy of diagnosis and staging and unveil the 3D organization of malignancies and their associated microvessels and other networks. Another possible

application of 3D histology would be the characterization of morphological changes across the host-tumor interface. The tumor interface is a dynamic region where cancer cells encounter and adapt to new microenvironments and other cell types. Future work should seek to expand the staining molecule library to enable visualization of extracellular matrix components, critical effectors and mediators of both homeostasis and pathologies. For example, hyaluronan can mediate angiogenesis and tumor vascularization and may be involved in the cirrhotic microvessel changes we found here. Collagen is undoubtedly involved in liver fibrosis and cirrhosis, and the ability to visualize and quantify fibrous septa in 3D would improve volumetric understanding of cirrhogenesis.

Technical limitations could also literally increase the depth and breadth of the work presented here. Increases in staining molecule penetration depth, like through the development of nanobodies and other small molecular weight staining molecules, would reach cells further into the tissue. Perhaps this would be a way to make the imaging of the entire lobule feasible in the Z dimension, past the portal-central axis presented here. Improvements in imaging technologies also allow capturing larger images than confocal systems and in shorter time frames. Light-sheet imaging systems are an example of a fluorescent imaging modality that can provide much faster scan times than confocal microscopes. Specific microscope objectives are being developed with long working distances and high numerical apertures specifically for imaging thick samples at high resolutions. Currently, they are cost-prohibitive, but we expect that they will become more accessible soon. The data generated by these imaging modalities can be on the order of terabytes, so the existing limitations in data handling and storage will need to be overcome both on the hardware and software sides of processing and analysis.

These possibilities raise theoretical questions about how large would be large enough to map the human liver completely. The liver comprises repetitive lobules, but they are not perfectly homogenous as the textbooks would have us assume. Imaging large enough to capture a representative sample of many lobules would likely be helpful. Perhaps robust imaging of 3D lobules like those presented here will provide preliminary data to perform power analyses to determine how many lobules would be statistically representative for measuring certain aspects. However, even if we could image an entire mouse liver or entire human lobe or organ, we would lose much of the high-resolution visual information of the smaller structures. The field would have to create a Google Maps-like interactive visualization module that would allow panning and zooming to synchronize structures across multiple scales. At a specific size scale, we would be imaging the same structures as less invasive modalities like CT, MRI, and ultrasound, so it would be worth considering that this may answer "how large is large enough." The advantage of 3D immunostaining would be to gather cell type information from these structures. Still, the antibody costs, data volumes, and imaging times would likely be prohibitive for structures that could already be visualized in 3D non-invasively.

This dissertation has bridged the gap between the cellular and tissue scales in the 3D organization of the human liver in homeostasis and cirrhosis. We hope that the work presented here provides inspiration for other researchers to image tissues in 3D at scales not yet explored and to ask questions regarding the structure-function relationships so critical to (patho)biology.

BIBLIOGRAPHY

[1] S. K. Asrani, H. Devarbhavi, J. Eaton and P. S. Kamath, "Burden of liver diseases in the world," *Journal of Hepatology,* pp. 151-171, 2019.

[2] U.S. Department of Health and Human Services, "Summary Health Statistics: National Health Interview Survey," 2018.

[3] L. Cordero-Espinoza and M. Huch, "The balancing act of the liver: tissue regeneration versus fibrosis," *The Journal of Clinical Investigation,* 2018.

[4] A. M. Kilbourne, G. Switzer, K. Hyman, M. Crowley-Matoka and M. J. Fine, "Advancing health care disparities research within the health care system: a conceptual framework," *American Journal of Public Health,* vol. 96, no. 12, pp. 2113-2121, 2006.

[5] U.S. Department of Health and Human Services Office of Minority Health, "National Partnership for Action to End Health Disparities Toolkit for Community Action".

[6] N. Lopez and V. Gadsden, "Health Inequities, Social Determinants, and Intersectionality," *National Academy of Medicine Perspectives,* 2016.

[7] G. C. Nguyen and P. J. Thuluvath, "Racial disparity in liver disease: Biological, cultural, or socioeconomic factors," *Hepatology,* vol. 47, no. 3, pp. 1058-1066, 2008.

[8] H. B. El-Serag and A. C. Mason, "Rising incidence of hepatocellular carcinoma in the United States," *New England Journal of Medicine,* 1999.

[9] V. K. Rustgi, G. L. Davis, S. K. Herrine, A. J. McCullough, S. L. Friedman and G. J. Gores, "Future trends in hepatology: challenges and opportunities," *Hepatology,* 2008.

[10] G. C. Gee and L. C. Ford, "Structural Racism and Health Inequities: Old Issues, New Directions," *Du Bois Review,* 2011.

[11] Z. D. Bailey, N. Krieger, M. Agenor, J. Graves, N. Linos and M. T. Bassett, "Structural racism and health inequities in the USA: evidence and interventions," *The Lancet,* vol. 389, no. 10077, 2017.

[12] R. Rosenblatt, N. Wahid, K. J. Halazun, A. Kaplan, A. Jesudian, C. Lucero, J. Lee, L. Dove, A. Fox, E. Verna, B. Samstein, B. E. Fortune and R. S. Brown, "Black Patients Have Unequal Access to Listing for Liver Transplantation in the United States," *Hepatology,* 2021.

[13] N. A. Wahid, R. Rosenblatt and R. S. Brown, Jr., "A Review of the Current State of Liver Transplantation Disparities," *Hepatology,* 2020.

[14] K. Wegermann, J. M. Wilder, A. Parish, D. Niedzwiecki, Z. F. Gellad, A. J. Muir and Y. A. Patel, "Racial and Socioeconomic Disparities in Utilization of Telehealth in Patients with Liver Disease During COVID-19," *Digestive Diseases and Sciences,* 2021.

[15] G. L. Armstrong, "Injection drug users in the United States, 1979-2002: an aging population," *Archives of Internal Medicine,* 2007.

[16] A. H. Mokdad, B. A. Bowman, E. S. Ford, F. Vinicor, J. S. Marks and J. P. Koplan, "The continuing epidemics of obesity and diabetes in the United States," *The Journal of the American Medical Association,* 2001.

[17] J. Guy and H. F. Yee, Jr., "Health Disparities in Liver Disease: Time to Take Notice and Take Action," *Hepatology,* 2010.

[18] J. M. Crawford, "Development of the Intrahepatic Biliary Tree," *Seminars in Liver Disease,* vol. 22, no. 3, 2002.

[19] M. Krishna, "Microscopic Anatomy of the Liver," *Clinical Liver Disease,* 2013.

[20] K. Kachi and S. W. French, "The connection between the nuclei of binucleated hepatocytes: an ultrastructural study," *Journal of Submicroscopic Cytology and Pathology,* vol. 26, no. 2, 1994.

[21] B. Gao, W.-I. Jeong and Z. Tian, "Liver: An Organ with Predominant Innate Immunity," *Hepatology,* 2008.

[22] A. Treyer and A. Musch, "Hepatocyte Polarity," *Comprehensive Physiology,* vol. 3, pp. 243-287, 2013.

[23] L. A. van Grunsven, "3D in vitro models of liver fibrosis," *Advanced Drug Delivery Reviews,* vol. 121, pp. 133-146, 2017.

[24] N. Katz, H. F. Teutsch, K. Jungermann and D. Sasse, "HETEROGENEOUS RECIPROCAL LOCALIZATION OF FRUCTOSE-l ,6-BIS- PHOSPHATASE AND OF GLUCOKINASE IN MICRODISSECTED PERIPORTAL AND PERIVENOUS RAT LIVER TISSUE," *FEBS Letters,* vol. 83, no. 2, 1977.

[25] E. L. LeCluyse, R. P. Witek, M. E. Andersen and M. J. Powers, "Organotypic liver culture models: Meeting current challenges in toxicity testing," *Critical Reviews in Toxicology,* vol. 42, no. 6, 2012.

[26] S. Colnot and C. Perret, "Liver Zonation," in *Molecular Pathology of Liver Diseases,* Spring Science and Business, 2011.

[27] J. Ahn, J.-H. Ahn, S. Yoon, Y. S. Nam, M.-Y. Son and J.-H. Oh, "Human three-dimensional in vitro model of hepatic zonation to predict zonal hepatotoxicity," *Journal of Biological Engineering,* vol. 13, 2019.

[28] R. Gebhart, A. Baldysiak-Figiel, V. Krugel, E. Ueberham and F. Gaunitz, "Hepatocellular expression of glutamine synthetase: An indicator of morphogen actions as master regulators of zonation in adult liver," *Progress in Histochemistry and Cytochemistry,* vol. 41, no. 4, 2007.

[29] K. O. Lindros, "Zonation of Cytochrome P450 Expression, Drug Metabolism and Toxicity in Liver," *General Pharmacology,* vol. 28, no. 2, 1997.

[30] S. Benhamouche, T. Decaens, C. Godard, R. Chambrey, D. S. Rickman, C. Moinard, M. Vasseur-Cognet, C. J. Kuo, A. Kahn, C. Perret and S. Colnot, "Apc Tumor Suppressor Gene Is the “Zonation-Keeper” of Mouse Liver," *Developmental Cell,* vol. 10, no. 6, 2006.

[31] A. Braeuning, M. Menzel, E.-M. Kleinschnitz, N. Harada, Y. Tamai, C. Kohle, A. Buchmann and M. Schwarz, "Serum components and activated Ha-ras antagonize expression of perivenous marker genes stimulated by β-catenin signaling in mouse hepatocytes," *The FEBS Journal,* 2007.

[32] R. Gebhart, "Metabolic zonation of the liver: Regulation and implications for liver function," *Pharmacology and Therapeutics,* vol. 53, no. 3, 1992.

[33] S. Edwards, P. F. Lalor, G. B. Nash, G. E. Rainger and D. H. Adams, "Lymphocyte traffic through sinusoidal endothelial cells is regulated by hepatocytes," *Hepatology,* vol. 41, no. 3, 2005.

[34] L. Modis and A. Martinez-Hernandez, "Hepatocytes modulate the hepatic microvascular phenotype.," *Laboratory Investigation,* vol. 65, 1991.

[35] E. Barbera-Guillem, M. Rocha, A. Alvarez and F. Vidal-Vanaclocha, "Differences in the Lectin-Binding Patterns of the Periportal and Perivenous Endothelial Domains in the Liver Sinusoids," *Hepatology,* vol. 14, no. 1, 1991.

[36] T. Horn, J. Henriksen and P. Christoffersen, "The sinusoidal lining cells in “normal” human liver. A scanning electron microscopic investigation," *Liver International,* vol. 6, no. 2, 1986.

[37] F. Braet and E. Wisse, "Structural and functional aspects of liver sinusoidal endothelial cell fenestrae: a review," *Comparative Hepatology,* vol. 1, 2002.

[38] O. Strauss, A. Phillips, K. Ruggiero, A. Bartlett and R. Dunbar, "Immunofluorescence identifies distinct subsets of endothelial cells in the human liver," *Scientific Reports,* vol. 7, 2017.

[39] P. F. Lalor, P. Shields, A. J. Grant and D. H. Adams, "Recruitment of lymphocytes to the human liver," *Immunology & Cell Biology,* 2002.

[40] B. Christ, S. Bruckner and S. Winkler, "The Therapeutic Promise of Mesenchymal Stem Cells for Liver Restoration," *Trends in Molecular Medicine,* vol. 21, no. 11, 2015.

[41] P. Friedl and D. Gilmour, "Collective cell migration in morphogenesis, regeneration and cancer," *Nature Reviews Molecular Cell Biology,* vol. 10, 2009.

[42] G. C. Gurtner, S. Werner, Y. Barrandon and M. T. Longaker, "Wound repair and regeneration," *Nature,* vol. 453, 2008.

[43] P. Ramachandran and J. P. Iredale, "Liver fibrosis: a bidirectional model of fibrogenesis and resolution," *QJM: An International Journal of Medicine,* vol. 105, no. 9, 2012.

[44] A. Martinez-Noguera, E. Montserrat, S. Torrubia and J. Villalba, "Doppler in Hepatic Cirrhosis and Chronic Hepatitis," *Seminars in Ultrasound, CT, and MRI,* vol. 23, no. 1, 2002.

[45] D. Schuppan and N. Afdhal, "Liver cirrhosis," *The Lancet,* vol. 371, no. 9615, 2008.

[46] B. E. Van Beers, R. Materne, L. Annet, L. Hermoye, C. Sempoux, F. Peeters, A. M. Smith, J. Jamart and Y. Horsmans, "Capillarization of the Sinusoids in Liver Fibrosis: Noninvasive Assessment With Contrast-Enhanced MRI in the Rabbit," *Magnetic Resonance in Medicine,* vol. 49, 2003.

[47] M. Sasaki, H. Ikeda, H. Haga, T. Manabe and Y. Nakanuma, "Frequent cellular senescence in small bile ducts in primary biliary cirrhosis: a possible role in bile duct loss," *The Journal of Pathology,* 2005.

[48] K. Sato, M. Marzioni, F. Meng, H. Francis, S. Glaser and G. Alpini, "Ductular Reaction in Liver Diseases: Pathological Mechanisms and Translational Significances," *Hepatology,* 2019.

[49] V. L. Gadd, R. Skoien, E. E. Powell, K. J. Fagan, C. Winterford, L. Horsfall, K. Irvine and A. D. Clouston, "The portal inflammatory infiltrate and ductular reaction in human nonalcoholic fatty liver disease," *Hepatology,* 2013.

[50] A. S. Gouw, M. C. van den Heuvel, M. Boot, M. J. Slooff, S. Poppema and K. P. de Jong, "Dynamics of the vascular profile of the finer branches of the biliary tree in normal and diseased human livers," *Journal of Hepatology,* 2006.

[51] L. Racine-Samson, J.-Y. Scoazec, A. D'Errico, M. Fiorentino, L. Christa, A. Moreau, C. Roda, W. F. Grigioni and G. Feldmann, "The Metabolic Organization of the Adult Human Liver: A Comparative Study of Normal, Fibrotic, and Cirrhotic Liver Tissue," *Hepatology,* 1996.

[52] R. D'Ambrosio, A. Aghemo, M. G. Rumi, G. Ronchi, M. F. Donato, V. Paradis, M. Colombo and P. Bedossa, "A morphometric and immunohistochemical study to assess the benefit of a sustained virological response in hepatitis C virus patients with cirrhosis," *Hepatology,* 2012.

[53] E. M. Sokal, P. Trivedi, B. Portmann and A. P. Mowat, "Adaptative Changes of Metabolic Zonation During the Development of Cirrhosis in Growing Rats," *Gastroenterology,* 1990.

[54] University of Cape Town Pathology Learning Centre, "Cirrhosis of the Liver," University of Cape Town, [Online]. Available: http://www.pathologylearningcentre.uct.ac.za/cirrhosis-of-the-liver. [Accessed 11 May 2021].

[55] A. Ghallab, M. Myllys, C. H. Holland, A. Zaza, W. Murad, R. Hassan, Y. A. Ahmed, T. Abbas, E. A. Abdelrahim, K. M. Schneider, M. Matz-Soja, J. Reinders, R. Gebhardt, M.-L. Berres and M. Hatting, "Influence of Liver Fibrosis on Lobular Zonation," *Cells,* vol. 8, 2019.

[56] S. Fujisawa, D. Yarilin, N. Fan, M. Turkekul, K. Xu, A. Barlas and K. Manova-Todorova, "Understanding the three-dimensional world from two-dimensional immunofluorescent adjacent sections," *Journal of Pathology Informatics,* 2015.

[57] J. T. C. Liu, A. K. Glaser, K. Bera, L. D. True, N. P. Reder, K. W. Eliceiri and A. Madabhushi, "Harnessing non-destructive 3D pathology," *Nature Biomedical Engineering,* 2021.

[58] R. V. Sillitoe and R. Hawkes, "Whole-mount Immunohistochemistry: A High-throughput Screen for Patterning Defects in the Mouse Cerebellum," *Journal of Histochemistry & Cytochemistry,* 2002.

[59] K. Marren, "Dimethyl Sulfoxide: An Effective Penetration Enhancer for Topical Administration of NSAIDs," *The Physician and Sportsmedicine,* 2011.

[60] M. Verheijen, M. Lienhard, Y. Schrooders, O. Clayton, R. Nudischer, S. Boerno, B. Timmerman, N. Selevsek, R. Schlapbach, H. Gmuender, S. Gotta, J. Geraedts, R. Herwig, J. Kleinjans and F. Caiment, "DMSO induces drastic changes in human cellular processes and epigenetic landscape in vitro," *Scientific Reports,* 2019.

[61] W. Li, R. N. Germain and M. Y. Gerner, "Multiplex, quantitative cellular analysis in large tissue volumes with clearing-enhanced 3D microscopy (Ce3D)," *PNAS,* 2017.

[62] W. Li, R. N. Germain and M. Y. Gerner, "High-dimensional cell-level analysis of tissues with Ce3D multiplex volume imaging," *Nature Protocols,* 2019.

[63] E. A. Susaki, K. Tainaka, D. Perrin, F. Kishino, T. Tawara, T. Watanabe, C. Yokoyama, H. Onoe, M. Eguchi, S. Yamaguchi, T. Abe, H. Kiyonari, Y. Shimizu, A. Miyawaki and

H. Yokota, "Whole-Brain Imaging with Single-Cell Resolution Using Chemical Cocktails and Computational Analysis," *Cell,* 2014.

[64] B. Yang, J. Treweek, R. Kulkarni, B. Deverman, C.-K. Chen, E. Lubeck, S. Shah, L. Cai and V. Gradinaru, "Single-Cell Phenotyping within Transparent Intact Tissue through Whole-Body Clearing," *Cell,* 2014.

[65] K. Chung, J. Wallace, S.-Y. Kim, S. Kalyanasundaram, A. Andalman, T. Davidson, J. Mirzabekov, K. Zalocusky, J. Mattis, A. Denisin, S. Pak, H. Bernstein, C. Ramakrishnan and L. Grosenick, "Structural and molecular interrogation of intact biological systems," *Nature,* 2013.

[66] M.-T. Ke, S. Fujimoto and T. Imai, "SeeDB: a simple and morphology-preserving optical clearing agent for neuronal circuit reconstruction," *Nature Neuroscience,* 2013.

[67] G. Bossolani, I. Pintelon, J. Detrez, R. Buckinx, S. Thys, J. Nelisis Zanoni, W. De Vos and J.-P. Timmermans, "Comparative analysis reveals Ce3D as optimal clearing method for in toto imaging of the mouse intestine," *Neurogastroenterology & Motility,* 2019.

[68] D. Jing, S. Zhang, W. Luo, X. Gao, Y. Men, C. Ma, X. Liu, Y. Ya, A. Bugde, B. O. Zhou, Z. Zhao, Q. Yuan, J. Feng, L. Gao, W.-P. Ge and H. Zhao, "Tissue clearing of both hard and soft tissue organs with the PEGASOS method," *Cell Research,* 2018.

[69] E. A. Susaki, C. Shimizu, A. Kuno, K. Tainaka, X. Li, K. Nishi, K. Morishima, H. Ono, K. L. Ode, Y. Saeki, K. Miyamichi, K. Isa, C. Yokoyama, H. Kitaura, M. Ikemura, T. Ushiku and Shimizu, "Versatile whole-organ/body staining and imaging based on electrolyte-gel properties of biological tissues," *Nature Communications,* 2020.

[70] E. Lee, J. Choi, Y. Jo, J. Y. Kim, Y. J. Jang, H. M. Lee, S. Y. Kim, H.-J. Lee, K. Cho, N. Jung, E. M. Hur, S. J. Jeong, C. Moon, Y. Choe, I. J. Rhyu, H. Kim and W. Sun, "ACT-PRESTO: Rapid and consistent tissue clearing and labeling method for 3-dimensional (3D) imaging," *Scientific Reports,* 2016.

[71] E. Lee and W. Sun, "ACT-PRESTO: Biological Tissue Clearing and Immunolabeling Methods for Volume Imaging," *Journal of Visualized Experiments,* 2016.

[72] F. Segovia-Miranda, H. Morales-Navarrete, M. Kucken, V. Moser, S. Seifert, U. Repnik, F. Rost, M. Brosch, A. Hendricks, S. Hinz, C. Rocken, D. Lutjohann, Y. Kalaidzidis and Schafmayer, "Three-dimensional spatially resolved geometrical and functional models of human liver tissue reveal new aspects of NAFLD progression," *Nature Medicine,* vol. 25, pp. 1885-1893, 2019.

[73] A. Newe, L. Becker and A. Schenk, "Application and Evaluation of Interactive 3D PDF for Presenting and Sharing Planning Results for Liver Surgery in Clinical Routine," *PLOS ONE,* 2014.

[74] F. Pegoraro, R. Montalti, G. Rompianesi, M. C. Giglio and R. I. Troisi, "Laparoscopic ICG-guided RALPPS procedure for HCC on cirrhosis with 3D reconstruction implementation: a case report," *Hepatoma Research,* vol. 7, no. 24, 2021.

[75] S. Hoehme, M. Brulport, A. Bauer, E. Bedawy, W. Schormann, M. Hermes, V. Puppe, R. Gebhardt, S. Zellmer, M. Schwarz, E. Bockamp, T. Timmel, J. G. Hengstler and D. Drasdo, "Prediction and validation of cell alignment along microvessels as order principle to restore tissue architecture in liver regeneration," *PNAS,* 2010.

[76] D. Drasdo, J. Bode, U. Dahmen, O. Dirsch, S. Dooley, R. Gebhardt, A. Ghallab, P. Godoy, D. Haussinger, S. Hammad, S. Hoehme, H.-G. Holzhutter, U. Klingmuller, L. Kuepfer, J. Timmer and Zeri, "The virtual liver: state of the art and future perspectives," *Archives of Toxicology,* 2014.

[77] G. Peeters, C. Debbaut, W. Laleman, D. Monbaliu, I. Vander Elst, J. R. Detrez, T. Vandecasteele, T. De Schryver, L. Van Hoorebeke, K. Favere, J. Verbeke, P. Segers, P. Cornillie and W. H. De Vos, "A multilevel framework to reconstruct anatomical 3D models of the hepatic vasculature in rat livers," *Journal of Anatomy,* 2017.

[78] N. Vartak, A. Damle-Vartak, B. Richter, O. Dirsch, U. Dahmen, S. Hammad and J. G. Hengstler, "Cholestasis-Induced Adaptive Remodeling of Interlobular Bile Ducts," *Hepatology,* 2016.

[79] S. Hammad, S. Hoehme, A. Friebel, I. von Recklinghausen, A. Othman, B. Begher-Tribbe, R. Reif, P. Godoy, T. Johann, A. Vartak, K. Golka, P. O. Bucur, E. Vibert, R. Marchan and B. Christ, "Protocols for staining of bile canalicular and sinusoidal networks of human, mouse and pig livers, three-dimensional reconstruction and quantification of tissue microarchitecture by image processing and analysis," *Archives of Toxicology,* 2014.

[80] K. Meyer, O. Ostrenko, G. Bourantas, H. Morales-Navarrete, N. Porat-Shliom, F. Segovia-Miranda, H. Nonaka, A. Ghaemi, J.-M. Verbavatz, L. Brusch, I. Sbalzarini, Y. Kalaidzidis and R. Weigert, "A Predictive 3D Multi-Scale Model of Biliary Fluid Dynamics in the Liver Lobule," *Cell Systems,* 2017.

[81] H. Morales-Navarrete, F. Segovia-Miranda, P. Klukowski, K. Meyer, H. Nonaka, G. Marsico, M. Chernykh, A. Kalaidzidis and M. Zerial, "A versatile pipeline for the multi-scale digital reconstruction and quantitative analysis of 3D tissue architecture," *eLife,* 2015.

[82] G. Peeters, C. Debbaut, A. Friebel, P. Cornillie, W. H. De Vos, K. Favere, I. Vander Elst, T. Vandecasteele, T. Johann, L. Van Hoorebeke, D. Monbaliu, D. Drasdo, S. Hoehme, W. Laleman and P. Segers, "Quantitative analysis of hepatic macro- and microvascular alterations during cirrhogenesis in the rat," *Journal of Anatomy,* 2018.

[83] H. Morales-Navarrete, H. Nonaka, F. Segovia-Miranda, M. Zerial and Y. Kalaidzidis, "AUTOMATIC RECOGNITION AND CHARACTERIZATION OF DIFFERENT NON-PARENCHYMAL CELLS IN LIVER TISSUE," in *2016 IEEE 13th International Symposium on Biomedical Imaging*, Prague, Czech Republic, 2016.

[84] H. Morales-Navarrete, H. Nonaka, A. Scholich, F. Segovia-Miranda, W. de Back, K. Meyer, R. L. Bogorad, V. Koteliansky, L. Brusch, Y. Kalaidzidis, F. Julicher, B. M. Friedrich and M. Zerial, "Liquid-crystal organization of liver tissue," *eLife,* 2019.

[85] M. Martignoni, G. M. M. Groothuis and R. de Kanter, "Species differences between mouse, rat, dog, monkey and human CYP-mediated drug metabolism, inhibition and induction," *Expert Opinion on Drug Metabolism & Toxicology,* 2006.

[86] The Human Protein Atlas, "Tissue Atlas - Liver - CDH1," [Online]. Available: https://www.proteinatlas.org/ENSG00000039068-CDH1/tissue/liver. [Accessed 14 May 2021].

[87] M. Hempel, A. Schmitz, S. Winkler, O. Kucukoglu, S. Bruckner, C. Niessen and B. Christ, "Pathological implications of cadherin zonation in mouse liver," *Cellular and Molecular Life Sciences,* 2015.

[88] O. Strauss and N. K. Bjorkstrom, "Sample Preparation of Optically Cleared Liver Tissue to Identify Liver Macrophages Using 3D Microscopy," in *Methods in Molecular Biology series - Kupffer Cells: Methods and Protocols*, New York, New York, USA, Springer Science+Business Media, LLC, 2020.

[89] W. Li, R. N. Germain and M. Y. Gerner, "High-dimensional cell-level analysis of tissues with Ce3D multiplex volume imaging," *Nature Protocols,* vol. 14, 2019.

[90] J. Schindelin, I. Arganda-Carreras, E. Frise, V. Kaynig, M. Longair, T. Pietzch, S. Preibisch, C. Rueden, S. Saalfeld, B. Schmid, J.-Y. Tinevez, D. J. White, V. Hartenstein and Eliceiri, "Fiji: an open-source platform for biological-image analysis," *Nature Methods,* 2012.

[91] H. Chai and R. E. Brown, "Field Effect in Cancer–An Update," *Annals of Clinical & Laboratory Science,* vol. 39, no. 4, 2009.

[92] Y. Hoshida, A. Villanueva and J. M. Llovet, "Molecular profiling to predict hepatocellular carcinoma outcome," *Expert Review of Gastroenterology & Hepatology,* vol. 3, no. 2, 2009.

[93] S. Marie, I. Hernandez Lozano, L. Breuil, W. Saba, M. Goislard, A. Novell, J.-L. Gennisson, O. Langer, C. Truillet and N. Tournier, "Determination of the MRP2-mediated transport capacity at the liver-bile interface using an improved 99mTc-mebrofenin imaging protocol," *The Journal of Nuclear Medicine,* 2020.

[94] J.-Y. Scoazec and G. Feldmann, "In Situ Immunophenotyping Study of Endothelial Cells of the Human Hepatic Sinusoid: Results and Functional Implications," *Hepatology,* 1991.

[95] R. Jain, S. Fischer, S. Serra and R. Chetty, "The use of Cytokeratin 19 (CK19) immunohistochemistry in lesions of the pancreas, gastrointestinal tract, and liver," *Applied Immunohistochemistry & Molecular Morphology,* 2010.

[96] K. Kisler, M. T. Huuskonen and B. V. Zlokivic, "Building vascular roadmaps: A novel toolset for visualizing and annotating whole mouse brain vasculature," *Lab Animal,* 2020.

[97] P. Lalor, W. Lai, S. Curbishley, S. Shetty and D. Adams, "Human hepatic sinusoidal endothelial cells can be distinguished by expression of phenotypic markers related to their specialised functions in vivo," *World Journal of Gastroenterology,* 2006.

[98] Y. Zhou, T. Eid, B. Hassel and N. C. Danbolt, "Novel aspects of glutamine synthetase in ammonia homeostasis," *Neurochemistry International,* 2020.

[99] N. Qvartskhava, P. A. Lang, B. Gorg, V. I. Pozdeev, M. Pascual Ortiz, K. S. Lang, H. J. Bidmon, E. Lang, C. B. Leibrock, D. Herebian, J. G. Bode, F. Lang and D. Haussinger, "Hyperammonemia in gene-targeted mice lacking functional hepatic glutamine synthetase," *PNAS,* 2015.

[100] J. Bucevicius, G. Lukinavicius and R. Gerasimaite, "The Use of Hoechst Dyes for DNA Staining and Beyond," *Chemosensors,* vol. 6, 2018.

[101] I. Nehrhoff, D. Bocancea, J. Vaquero, J. J. Vaquero, J. Ripoll, M. Desco and M. V. Gomez-Gaviro, "3D imaging in CUBIC-cleared mouse heart tissue: going deeper," *Biomedical Optics Express,* vol. 7, no. 9, 2016.

VITA

Chelsea Louise Fortin was born in South Portland, Maine, in 1992 and raised in Rumford, Maine. She earned her Bachelor of Arts in Biology: Specialization in Cell Biology, Molecular Biology, and Genetics from Boston University in 2014, performing research in the lab of Dr. Xaralabos "Bob" Varelas from 2012 to 2014. Chelsea worked in the lab of Dr. Sangeeta Bhatia at the Massachusetts Institute of Technology from 2014 to 2015. She then moved across the country to be the founding staff member of the Stevens Lab at the University of Washington in 2016, beginning the doctoral program that autumn. Chelsea earned her Doctor of Philosophy in Molecular Medicine and Mechanisms of Disease from the University of Washington in 2021.